ISBN 978-82-326-5760-5 (printed ver.)
ISBN 978-82-326-6084-1
(electronic ver.)
ISSN 1503-8181 (printed ver.)

NTNU
Norwegian University of
Science and Technology

Silje Kreken Almeland

Doctoral thesis

Doctoral theses at NTNU, 2021:62

NTNU
Norwegian University of
Science and Technology
Thesis for the degree of
Philosophiae Doctor
Faculty of Engineering
Department of Civil and Environmental
Engineering

NTNU

Doctoral theses at NTNU, 2021:62

Silje Kreken Almeland

Numerical modelling of air entrainment

In hydraulic engineering

NTNU
Norwegian University of
Science and Technology

Silje Kreken Almeland

Numerical modelling of air entrainment

In hydraulic engineering

Thesis for the degree of Philosophiae Doctor

Trondheim, March 2021

Norwegian University of Science and Technology
Faculty of Engineering
Department of Civil and Environmental Engineering

NTNU
Norwegian University of
Science and Technology

NTNU
Norwegian University of Science and Technology

Thesis for the degree of Philosophiae Doctor

Faculty of Engineering
Department of Civil and Environmental Engineering

ISBN 978-82-326-5760-5 (printed ver.)
ISBN 978-82-326-6084-1 (electronic ver.)
ISSN 1503-8181 (printed ver.)
ISSN 2703-8084 (electronic ver.)

Doctoral theses at NTNU, 2021:62

PRINTED IN
NORWAY
NO - 1598

NORDIC SWAN ECOLABEL
Printed matter
2041 0731

Printed by Skipnes Kommunikasjon AS

Abstract

Air entrainment in water flows is a natural phenomenon prone to take place when energy is dissipated in flowing water. In nature, air entrainment appears as white water in waterfalls or in waves breaking on the beach. Within this process, air is forced into the water bulk. This results in a very complex flow pattern involving a broad range of time and length scales, which makes it challenging to measure experimentally and to reproduce numerically. In several hydraulic applications, air entrainment plays an important role and needs prediction to ensure safe and efficient operation of the particular structure. Within this work, numerical modelling of air entrainment in water flows has been considered. More specifically, modelling of a stepped spillway and a hydraulic jump is encountered using different approaches for air entrainment modelling and turbulence treatment.

A highly efficient approach, accounting for air entrainment in a subgrid model, was developed and proven to work well for a broad range of stepped spilway flows. The solver was built upon OpenFOAM®'s VoF solver `interFoam` in a RANS framework.

Furthermore, a LES approach coupled with interface capturing within the VoF framework, was employed to predict turbulence and air entrainment for the complex flow of a hydraulic jump. In a detailed simulation, the used methodology was shown to reproduce the flow pattern within the hydraulic jump in impressive agreement to corresponding DNS simulations. It thereby proved the predictive capability of OpenFOAM®'s VoF solvers for this flow.

In light of previously reported lack of proper verification and validation of numerical models within hydraulic engineering, an integral part of the work has also been to consider the more or less crucial influence of changing modelling parameters.

Preface

This thesis is submitted to the Norwegian University of Science and Technology (NTNU) in Trondheim for partial fulfilment of the requirements for the degree of Philosophiae Doctor (PhD).

This work is the result of a four-year PhD program, which was conducted at the Department of Civil and Environmental Engineering. The PhD position was allocated to 75% research and 25% teaching. The teaching part included contributions to lecturing, assignment creation and guidance of student assignments, as well as censoring exams, in TVM4155–Hydroinformatics and TVM4116–Hydromechanics.

In line with the polices at NTNU, the work was conducted in cooperation with international research communities. 13 months of the PhD period was spent at the Department of Mechanics and Maritime Sciences at Chalmers University of Technology in Gothenburg.

Professor Nils Olsen and professor Nils Rüther have contributed as main- and co-supervisors from NTNU, while professor Rickard Bensow and postdoc Timofey Mukha contributed to the supervisor task during the research stay at Chalmers.

The project has been funded by the Faculty of Engineering, and computing resources have been provided by UNINETT Sigma2 – the National Infrastructure for High Performance Computing and Data Storage in Norway, NTNU IDUN/EPIC computing cluster, and Chalmers Centre for Computational Science and Engineering (C3SE).

In accordance with the guidelines of the Faculty of Engineering, this thesis comprises a summary of the research that resulted in three scientific journal papers.

Acknowledgement

There will be mountains that I will have to climb,
and there will be battles that I will have to fight,
but victory or defeat, it's up to me to decide,
but how can I expect to win if I never try –
I just can't give up now,
I've come too far from where I started from,
nobody told me the road would be easy ...

-Mary Mary-

As a teenager, I heard this song that somehow got stuck in my head, and later also in my heart, and ended up motivating me through several challenges within sports and in life in general. I must admit that from time to time during the work terminating in this thesis, the voice of Mary Mary has been repeated in my head, and also from my most powerful speakers. It has been a journey, an educational journey along a bumpy road, made smoother with the help from various people I've been delighted to meet along the way. To these peoples, I owe a great thank you.

First of all, I would like to say that I feel privileged to have had the opportunity to spend some years of my working career to do research and complete the highest academic education. I express my deep gratitude to my main supervisor Nils R. B. Olsen. Thank you for setting the course of this project, having faith in me, and for giving me the opportunity to follow my wishes. I also direct gratefulness to Nils Rüther for fruitful discussions and for following up as a co-supervisor.

Furthermore, this thesis would not have been possible without my cooperators at Chalmers and Gothenburg. Regarding this, I want to thank Rickard Bensow for his guidance and for giving me the opportunity to develop my skills in a unique learning environment at the Marine department at Chalmers. And Timofey, I can't

thank you enough for the time you have invested in this work with me.

But that chapter of my PhD would never have been realized without the online slides from Chalmers' OpenFOAM® course, which piqued my interest in this place. So thanks to Håkan Nilsson for this course, and for finally accepting me as a student during the fall semester in 2018.

Perhaps my year in Gothenburg would not have been as fruitful without the people who showed me around in the forest areas around the city on two wheels. So biking friends - thanks for making my life in Gothenburg even more joyful, and for helping me out in several situations.

Besides the people directly involved in my PhD-work, many people have inspired me along the academic road, which has led to the choices I've ended up making. From my master studies, I want to thank Tore Haug-Warberg for opening my eyes to the world of numerical modelling and programming, and for making me a true wannabe-nerd during my master studies. And then, thanks to Anders, Eirik and Torstein for inspiring me to continue down this path during my five years at Petrell. I would also like to convey appreciations to my friend Kari who encouraged me to apply for the PhD position late 2015.

Furthermore, I want to thank my colleagues at NTNU – a few mentioned, but none forgotten. Slaven, thanks for the endless numbers of long evenings at the office, I appreciated your company and working endurance. Thanks to Ragnhild for keeping my mood up with her always funny snaps, Tobias for help and inspiration in my OpenFOAM® learning process, and Ganesh for proofreading assistance. A special thank you goes to Fjola for finally bringing her special cake, and for weekly Sunday coffees and muffins at the office during the autumn of 2018. And some well-deserved attention to the guy with the duck tattoo, Andreas, thank you for being my guardian angel when I've got myself into trouble with my Linux computer.

Finally, thanks to my friends and family. To all my good friends, thank you for hundreds of laughing hours, joyful company and good conversations, and for keeping my mind busy during my spare time. And last but not least, I have to express my heartfelt gratitude to my family; to my parents for their never-ending care and constant support in life, and to my siblings, Stian and Grunde, for inspiration, motivation and encouragement.

Contents

List of publications

Paper I: Silje K. Almeland, Nils R. B. Olsen, Kari Bråveit, and Pravin R. Aryal. Multiple solutions of the Navier-Stokes equations computing water flow in sand traps. *Engineering Applications of Computational Fluid Mechanics*, 13(1):199-219, January 2019. doi: 10.1080/19942060.2019.1566094

Paper II: Silje Kreken Almeland, Timofey Mukha, and Rickard E. Bensow. An improved air entrainment model for stepped spillways. *Applied Mathematical Modelling*, October 2020 (under review).

Paper III: Timofey Mukha, Silje Kreken Almeland, and Rickard E. Bensow. LES of a classical hydraulic jump: Influence of modelling parameters on the predictive accuracy. *Computers & Fluids*, October 2020 (under review).

Chapter 1

Introduction

1.1 Background

In certain instances, air will be drawn into the water flow and flow along with the water in a fluid mixture of air and water. Examples of this are when water flows down waterfalls, a jet hits a pool, or when high-velocity water flows down a sloped channel or a river. The process is referred to as air entrainment or aeration, and is a natural phenomenon in flowing water, prone to happen when energy is dissipated in free-surface flow. Air entrainment leads to a change in the physical properties of the flow, and may have crucial impacts on its behaviour [15]. At hydraulic structures, this aeration can lead to capacity overestimation, which constitutes safety issues, and can under unfortunate circumstances lead to severe damages of the structure. To clarify and illustrate these mentioned issues, some specific examples of aerated flow at hydraulic structures will be provided in the following.

Depending on the flow conditions, the water from a river intake will entrain air on its way down the dropshaft and towards the closed tunnel. This air might be transported all the way to the turbines, or trapped at the tunnel roof. In both cases, the air will occupy volume, and thereby reduce the discharge capacity. Air trapped at the tunnel roof creates potential for pressure loss, again influencing the discharge capacity negatively, but even worse it creates a potential for explosive blowouts which has been a challenge in several installations [37, 3, 18, 68, 61, 48, 23].

As the intakes lead water into the waterways and towards the turbines for electricity production, a spillway is used to control the water level at the dam. The spillway is active in flood events, when the amount of water in the reservoir increases beyond accepted values and should be dimensioned to withstand a certain flood load.

Along the spillway, aeration occurs and leads to increased surface heights of the flow. This has to be accounted for in the design of the spillway walls [6].

However, an advantage of the air entrainment process is encountered when designing the downstream energy dissipator required to protect the downstream river from erosion. The entrained air leads to energy dissipation along the spillway and thus reduces the needed scale of the energy dissipator [5]. Additionally, the presence of air in the flow can act to reduce damages caused by cavitation [5, 13, 25], a known threat to hydraulic structures. Cavitation is the process where water undergoes a phase transition to water vapour and happens when pressures below the vapour pressure appear in the flow. When the pressure later raises, or the vapour cavities are transported to higher pressure regions, the vapour bubbles might impel at the structure and cause damages [32]. Thus, air within the water flow might provide a protecting layer to the structure. Furthermore, flow aeration is known to reduce friction forces at the walls. This might impact the flow velocity, but is generally more important in naval engineering [46], where friction is of crucial importance to the transport efficiency.

In most applications where air entrainment plays an important role in hydraulic engineering, its existence is uncontrolled and not intended, but exists as a result of the flow conditions at the structure [15]. Due to its impact on the fluid flow, a necessity of having a measure of the amount of entrained air and its effect on the exposed flow, is acknowledged in the hydraulic engineering community. A general way to obtain such information is through investigation by the use of scaled physical laboratory models. However, in the case of air entrainment, physical model testing might not give accurate results due to the multiple set of physical factors that influence the process and makes the choice of scaling similitude challenging [15]. Froude number scaling is normally used for open channel flows, but in the case of flow aeration, air bubbles are entrained into the flow, which size will not scale correctly when subject to the geometric Froude similitude. Resultingly, uncorrect scaling will affect the air entrainment properties [17, 16].

Besides the evident challenges for physical model tests related to scaling effects, a major challenge in describing air entrainment emerges from the fact that it constitutes a very complicated process, spanning a broad range of time and length scales, involving both the motion of the interface and its interaction with the turbulence structures. This makes the use of standard measuring techniques in general use for single-phase flows, such as laser Doppler velocimetry (LDV), acoustic Doppler velocimetry (ADV), and particle image velocimetry (PIV), challenging [15].

Numerical modelling constitutes another way to predict the behaviour and characteristics of the flow. Even if numerical reproduction of the aeration process is a very demanding task, the increased availability of high performance computing (HPC) resources, improves its possibility. The use of numerical techniques might have the potential to improve the understanding of the mechanisms within the air entrainment processes, and thereby contribute to safer and more efficient design and operation of hydraulic structures.

The work done within the scope of this thesis is devoted to this topic, as reflected by the contents of the papers. The following section gives a review of the state of the art in numerical modelling of air entrainment.

1.2 State of the art

The multiphase structures emerging from the air entrainment process and its interaction with the flow's turbulent structures constitute a challenge for numerical reproduction. A reliable numerical solver for this purpose has to capture the topological changes at and below the free-surface, taking place in a broad range of spatial scales and is a real test on its predictive capabilities. Since air entrainment is driven by turbulence, one has to consider the approaches for turbulence and the multiphase together. For this purpose, one generally distinguishes between high- and low-fidelity approaches, both of which have been applied to hydraulic engineering applications.

In the high-fidelity approaches, such as Direct Numerical Simulations (DNS) and Large Eddy Simulations (LES) coupled with a method to explicit capture the interface, the aim is to resolve all the important scales of the problem within the computational mesh, resulting in a dense mesh and resource demanding computations. When applied to air entrainment, these approaches have generally been considered too computational demanding for industrial use. Thus, providing insight into the physics of the processes taking place when air entrainment occurs, is considered their primary application. Thereby, such computations can also contribute in validation matters of lower fidelity modelling approaches.

The other approach is to apply some kind of modelling framework to account for the important small scale mechanisms of the air entrainment process, while the computational mesh is kept at moderate resolution levels. This results in more efficient solvers, but at the expense of accuracy. Most often these solvers are based on the Reynolds Averaged Navier-Stokes (RANS) equations, combined with a subgrid model to account for bubbles. However, a challenge when it comes to modelling of the air entrainment process arises from its two-ways interaction with the turbulence.

In spite of the obvious challenges noted above, efforts using both paths has been reported in the literature. Starting in the scale-resolving regime, Mortazavi et al.

[43] reported a DNS simulation on a hydraulic jump with inlet Froude number 2, showing reasonable agreement with experimental results, thereby constituting a mean for further physical insight into the flow phenomena. Also on the hydraulic jump, but on a higher inflow Froude number, Jesudhas et al. [31] performed Detached-Eddy Simulations (DES), where most of the domain were applied to the LES regime. Results in excellent agreement with experiments were reported, providing new insight into the turbulent structure of the hydraulic jump.

LES analyses on plunging jets where done by Deshpande et al. [19] and Khezzar et al. [33]. Deshpande et al. [19] reported good agreement with experimental results for a jet plunging into shallow water with an impact angle of 12.5°. Excellent accuracy was obtained for the immediate effect of the impingement jet on the receiving water, but the long time behaviour was not reported. In this work, the filtered part of the turbulent spectrum was not modelled, but rather simply ignored, following an implicit approach for turbulence treatment. A reasoning behind this choice was that single-phase turbulence models are expected to fail in regions where strong coupling between unresolved turbulence motion and unresolved interfacial structures appears.

Khezzar et al. [33] investigated vertical plunging jets with different roughness levels of the jet in a LES, using the Smagorinsky subgrid scale model. They found that the surface instabilities in the free jet due to turbulence did not change the velocity field in the receiving pool much, but influenced the turbulence field and affected the air entrainment properties. The same model framework was used when Lubin et al. [40] studied air entrainment in breaking waves. They acknowledged the process of air entrainment as important to capture due to its influence on the turbulence generation.

Developments following the path of lower fidelity approaches, introducing an additional model to account for the entrained air, are also reported in the literature. The majority of these efforts are based on Reynolds averaged Navier-Stokes (RANS) equations.

Different ways of introducing air entrainment models into the equation set have been purposed, also varying in the general multiphase regime applied. Normally, the interface capturing methods are used for stratified flows, where the important length scales are several times the cell size of the computational mesh. For dispersed two-phase flows, where a substantial part of the two-phase structures are smaller than the computational grid, a two-fluid (Euler-Euler) framework is generally used. However, at least when treated by low-fidelity approaches, the air entrainment process tends to belong to both regimes, the topology of the surface and the larger bubbles belonging to the stratified flow regime, while the small unresolved bubbles fit into the dispersed flow regime.

Attempts trying to combine a two-fluid Euler-Euler formulation with interface capturing have been reported by several researches [30, 54, 63, 12, 57]. These works generally try to benefit from the features of the interface capturing methods in regions where this is of importance, and then use a dispersed framework in other regions, accounting for air entrainment characteristics in source terms in the momentum equations, and in turbulent model equations.

The work of Cerne et al. [12] constitutes an early attempt here, changing between equation sets for the two regimes by a switching function based on a threshold value for the gradient of the volume fraction across neighbouring cells. Strubelj and Tiselj [57] continued this work. Acknowledging the numerical issues related to switching between the equation sets, they applied a two-fluid formulation for the entire domain, using interface sharpening in relevant regions. Both the above works noted the high dependency of the results on the chosen threshold for the switching function.

Within the framework of OpenFOAM®, Shonibare and Wardle [54] followed a similar path, applying artificial interface compression on top of a two-fluid framework. Addressing the effects of the bubble size distribution on the bubble rise velocity, models to account for variable bubble sizes were introduced. The interface compression was dynamically deactivated if the local mesh size was smaller than a user defined multiple of the mean bubble size. The latter was calculated from the population balance implementation. This model was conceptually tested on a vertical plunging jet in a LES type of framework.

Application of interface compression on top of a two-fluid framework was also presented by Hänsch et al. [27]. In this work they added a continuous gas phase to the MUSIG model [35]. Substantial attention was devoted to the modelling of the interaction between bubbles, turbulence and the free surface, where ideas from the descriptive study of Brocchini and Peregrine [9] were incorporated as a production term in the k-equation within the k-ω SST-model. The model was shown capable of capturing the motion of the flow in the dam break case with obstacle through visual comparison. However, it was noted that the model was still under development, lacking a model to couple the turbulent kinetic energy in the liquid phase to entrainment of air into the dispersed regime.

Introduction of an air flux term to account for the inclusion of air due to processes at and near the interface was proposed by Ma et al. [41]. This model used a single-phase level-set framework to capture the interface. Then air was introduced in a subsequent step based on the turbulence in the liquid phase and entered as a source term within a two-fluid framework. The model was shown to perform well for a hydraulic jump and a vertical plunging jet [41]. Nevertheless, as the surrounding air phase was not included in the model, no natural source of air existed, and the aeration had to be explicitly defined by the air entrainment model.

Building further on the work of Hänsch et al. [27], Höhne and Hänsch [30] introduced an entrainment model to capture droplets above the surface. The model was inspired by the work of Ma et al. [41], but instead of using the framework for entrainment of bubbles, it was used for entrainment of droplets into the continuous air phase. The model was tested on a horizontal two-phase flow.

Another branch of modelling approaches tries to capture air entrainment within the interface capturing methods by including its effects in an additional source term to be activated at the interface. The work of Hirt [28] constitute an early effort within this branch. A source term defined based on expressions of stabilising and perturbing forces, and a balance between these, were added to the advection equation within the Volume of Fluid (VoF) method. The model was implemented in Flow3D® and has been used in publications on stepped spillways [59, 21].

Similarities to the work of Hirt [28] can be found in the air entrainment model by Lopes et al. [39]. In this work, the air flux estimator from the model of Ma et al. [41] was adopted and implemented into an air entrainment model developed within the framework of `interFoam`, which is the VoF solver of OpenFOAM®. The model was validated on a stepped spillway.

Results on air entrainment computations using RANS coupled with two-equation turbulence models, without additional modelling of air entrainment, have also been reported to give accurate predictions on aerated flows [65, 50]. Nevertheless, it might be a conceptual question whether it makes sense to capture the dynamics of the topological changes of an air entrainment problem in a RANS simulation, acknowledging the principle behind the averaging procedure leading to these equations. In an aerated flow, it might be a question whether the topological changes at the interface are noticeably slower than the turbulent time scales of the particular flow.

As the above review reveals, promising results on numerical prediction of aerated flows have been provided in the literature, both using high- and low-fidelity approaches. Nevertheless, as noted several times, aerated flows are challenging to reproduce numerically due to its broad range of length scales, as well as its inherent interaction of turbulence and multiphase structures. As a result of this, modelling effort for this purpose still struggle to work satisfactory and efficiently. The work within this thesis constitutes an effort to contribute to developments related to these challenges.

1.3 Aims and scope of work

This study aims to contribute to the development of numerical prediction of air entrainment in free surface-flows, where the overall goal is to develop a tool or methodology for its prediction, suitable for hydraulic engineering applications. The numerical modelling work is performed within the framework of OpenFOAM®, using its VoF solver, `interFoam`, as a starting point. Based on this, the research objectives of this dissertation are stated as:

- Understanding the process of air entrainment and identify the important components to be modelled.
- Test and review available tools.
- Develop high- and low-fidelity methodologies for the prediction of aerted flows based on the VoF-method.
- Provide tools/methodologies for prediction of air entrainment available for hydraulic engineering applications.

Based on the above research objectives, where the aim is to review, test and develop numerical tools and simulation procedures, an additional aim is to emphasise the importance of proper verification and validation of the methods, and how the choice of modelling parameters might influence the numerical results. A last aim is to use open source tools in this research.

Within the work to achieve the research objectives, flow cases of importance in hydraulic engineering are chosen for numerical studies. More specific, stepped spillway flows, classical hydraulic jumps, and settling basins are considered. Here the two first flow cases are investigated in terms of air entrainment.

The remaining part of this dissertation describes the process of air entrainment (Chapter 2) in general and applied to the considered flow cases, the research methods (Chapter 3), and the developed air entrainment model (Chapter 4). Then the main results are presented in Chapter 5, and discussed against the research objectives and state of the art in Chapter 6. Finally, conclusive remarks are provided in Chapter 7.

Chapter 2

Air entrainment in hydraulic engineering

In this chapter, the concept of air entrainment is defined and explained briefly. Furthermore, a short description of the air entrainment features of the applications considered within this work is provided. These sections will be fruitful as background material for the remaining part of this dissertation, and Chapter 4 and Chapter 5 in particular.

2.1 Air entrainment

The process where air bubbles are drawn into and carried away with the flowing water is termed air entrainment or aeration, and results in a dispersed two-phase flow below the free surface, with a complex interaction of turbulence and multiphase structures. The entrained air influences the transport properties of the flowing water, which motivates investigation from an engineering point of view.

For a general free-surface flow, air will be entrained at the free-surface when the turbulent shear stress at the free-surface exceeds the stabilizing forces of surface tension and buoyancy [53, 22]. The entrainment process is driven by turbulent eddies close to the surface, causing surface disturbances that need to be of a certain size to exceed the mentioned stabilising forces, and create air entrainment [22].

Fundamentally one differs between two causes of air entrainment, local aeration and interfacial aeration, which are both described in [14]. Local aeration is initiated by a discontinuity in the flow path where air bubbles are entrained. This is the kind of aeration that takes place when a plunging jet hits the surface of a stationary pool, or when the supercritical inlet flow of a hydraulic jump meets the subcritical outlet flow. For these flows, researchers often talk about a critical threshold velocity that has to be exceeded for entrainment to occur [34, 53]. These threshold velocities are empirically defined, and yields a measure of the balance between disturbing and stabilising forces at the free-surface. Interfacial aeration is the type of air entrainment process that occurs along, and often parallel to a surface, and is caused by the turbulent forces acting on the surface. This is the kind of aeration that might take place along the surface of a steep channel flow.

The following sections describe aeration properties of the particular cases treated within this work, constituting a stepped spillway and a hydraulic jump. Air entrainment in the latter might involve both local and interfacial aeration, whereas the aeration of a spillway is classified as interfacial aeration.

2.2 Stepped spillway

Recall from Section 1.1 that a spillway constitutes an overflow device, used to protect the dam in flood situations. It should therefore be dimensioned to withstand a certain flood discharge. An important factor to consider regarding this is that flow aeration will take place along the spillway and that this will elevate the water level and increase the needed height of the training walls. Also, as noted in Section 1.1, the presence of air in the water can reduce the damages caused by cavitation. By being able to account for the appearance of air in the water, other preventive cavitation measures can be reduced. The above issues motivate the prediction of flow aeration at stepped spillways.

Aeration along a spillway flow is driven by the action of turbulent forces close to the free-surface, and constitute an example of the interfacial aeration mechanism. The aerated part of the spillway is initiated by the inception point, which is commonly considered to be found where the turbulent boundary layer, developed from the spillway crest, reaches the free-surface [56]. Downstream this point, the properties of the flow are gradually changing until quasi-steady flow conditions are obtained in the uniform flow region [13]. Figure 2.1 gives a conceptual sketch of a stepped spillway, indicating the different flow regions.

The general principles described above are relatively equal for a smooth and stepped spillway. Nevertheless, the steps introduce more turbulence and energy dissipation, and the inception point is found further upstream at the stepped spillway, compared to its smooth counterpart [5, 10]. Due to the above, also the size of the energy dissipator used to protect the downstream river, can be reduced.

Dependent on the discharge, angle and step height, the spillway might be operated in the nappe, alternated or skimming flow regime. Most spillways are operated in the skimming flow regime, which, according to Boes and Hager [6], applies when

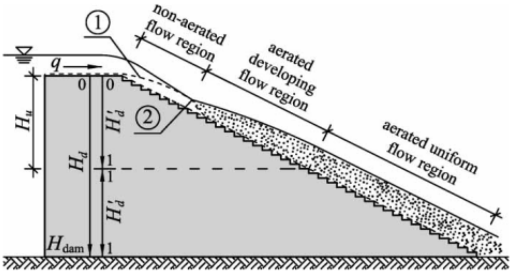

Figure 2.1: Principal sketch of a stepped spillway showing the different flow regions. ① indicates the growing boundary layer from the spillway crest, while ② indicates the inception point. Reprinted from [10], with permission from Taylor & Francis.

$$\frac{h_c}{s} \geq 0.91 - 0.14\tan\theta,$$

where s is the step height of the spillway, θ its angle relative to the horizontal, and $h_c = (q^2/g)^{1/3}$ is the height occurring at critical flow conditions, where q ($\mathrm{m}^2\mathrm{s}^{-1}$) is the specific discharge, and g is the acceleration due to gravity. Furthermore, the step Froude number

$$\mathrm{F}_s = \frac{q}{\sqrt{g \cdot \sin\theta K^3}} \quad ,$$

where $K = s\cos\theta$, is known as the controlling parameter for stepped spillway flows [10].

A vertical cross-section profile of an aerated flow in a stepped spillway is illustrated in Figure 2.2. As shown in the figure, the upper part of the flow consists of a mixture of air and water, and then the air fraction is reduced in the vertical direction. Nevertheless, some air might be present all the way down to the pseudo-bottom, which is an imaginary bottom shown as x in Figure 2.2. Within the steps, a recirculation zone is present, which introduces a mixing layer around the pseudo-bottom. In aerated open channel flow, the free-surface is commonly identified as the location where the volumetric air fraction α_l equals 0.9. This height is generally referred to as h_{90} or Y_{90} [10].

The literature provides several research efforts, reproducing the flow structure of stepped spillways using numerical approaches [67, 21, 38, 52, 59, 39]. Nevertheless, to the best of the author's knowledge, no studies using VoF (RANS or LES) has yet been performed that succeeded in capturing the dynamics of the self-

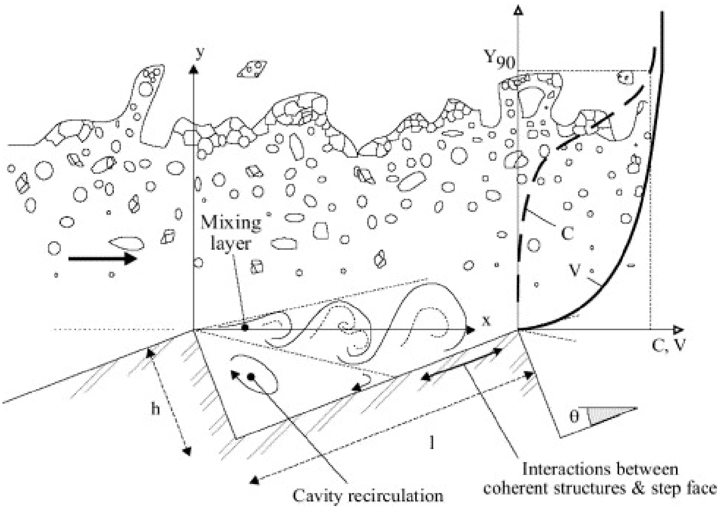

Figure 2.2: Principal sketch of the vertical profile of an aerated stepped spillway flow. The air fraction and the velocity are indicated by C and V respectively. Reprinted from [58], with permission from Elsevier.

aeration along a spillway.

Simulations on stepped spillways using OpenFOAM's VoF solver `interFoam` has been reported in several studies [38, 39]. Still, none of these studies were able to capture air entrainment. In other numerical studies on stepped spillways, the inclusion of air in the flow was reported when an external air entrainment model was included in the VoF framework [59, 21]. However, in [59], the agreement to experimental results was only fear, while a detailed numerical analysis of the aeration properties was missing in [21].

In this work (Paper II), a numerical model to predict the air entrainment features along a spillway is presented and tested on a broad range of step Froude numbers. This model is described in Chapter 4 and a summary of the major findings are provided in Section 5.2.

2.3 Hydraulic jump

A hydraulic jump is an abrupt change in water level in a shallow open channel flow, where the flow goes from super- to sub-critical. This flow phenomenon is frequently seen in rivers and spillways. In nature, a hydraulic jump is prone to arise when high-velocity flows from steep rivers hit a stone or its similar, on its way down the mountains. Downstream a spillway, a hydraulic jump is usually enforced to slow down the water velocity to protect the river from erosion and scour, caused by the forces within the high-velocity water flow. A hydraulic jump that takes place in a rectangular channel is known as a classical hydraulic jump and constitutes the hydraulic jump investigated within this work.

The abrupt change in water level leads to a very complicated flow pattern where turbulent structures interact with the free-surface, promoting air entrainment and energy release. The latter defines its main application in hydraulic engineering as the most used energy dissipator [2]. This has motivated numerous experimental and numerical studies of this phenomenon. To that end, a recent review can be found in [60, 62]. Due to its turbulent and chaotic structure, the hydraulic jump also serves as a mixing device in the chemical industry, and it is used as a flow aerator for environmental purposes.

Figure 2.3 gives a schematic illustration of a hydraulic jump, highlighting its different parts. The toe defines the start of the jump and is found at the location where the water level increases abruptly. Here the high-velocity inlet jet impinges into slower moving water downstream, resulting in air entrainment and a highly turbulent region. The position of the toe is known to oscillate back and forth around its mean location, which also contributes to the transient nature of this phenomenon. Furthermore, the remaining structure of the jump can be divided into several parts. In the upper part preceding the toe, a recirculating flow region is formed, known as the roller. Its downstream length, starting at the toe, is defined as L_r. Below the roller, the wall-jet flow region is found. Here the streamwise velocity is slowly reduced in the downstream direction. Between the wall jet and the roller, a turbulent shear region arises, where the mixing properties are good. Downstream the roller, deaeration will occur. The prevalence of this process will depend on the transport properties of a particular flow. A particular distance downstream the jump, the flow properties are no longer affected by the jump. Here the free-surface stabilises at the new water level, d_2, and normal open channel flow properties are regained.

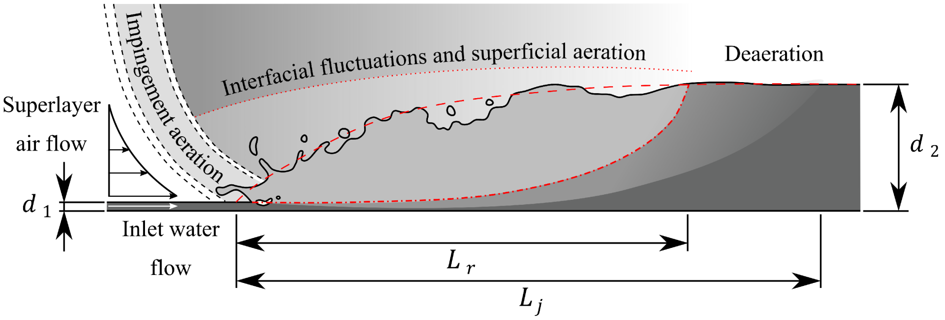

Figure 2.3: Sketch of an hydraulic jump. Reprinted from [60].

The hydraulic jump is usually defined by its inlet Froude number $Fr = u/\sqrt{gd}$, which is also used to classify the jumps. This classification is described in [60]. Since the main use of the hydraulic jump for engineering purposes is as an energy dissipator, an aim should be to release as much energy as possible. The energy release increases with the Froude number, and for $F_r > 9$, as much as 70% energy reduction might be found. Nevertheless, these jumps tend to be very unstable and entrain substantial amounts of air. The most stable jumps are found in the range Fr_1=[4.5,9], which facilitate their use for engineering applications.

Despite the complicated nature of the hydraulic jump, some of its properties can be easily derived analytically, based on the inflow parameters. Derived from the momentum equation the conjugate depth d_2 can be calculated as

$$d_2 = 0.5 d_1 \left((1 + 8\mathrm{Fr}_1^2)^{0.5} - 1 \right).$$

Taking advantage of the above, the jump efficiency can be derived from the change in specific energy and formulated as

$$E_2 = E_1 \frac{(8Fr_1^2 + 1)^{3/2} - 4Fr_1^2 + 1}{8Fr_1^2(2 + Fr_1^2)}.$$

As indicated above, the amount of entrained air also depends on the Froude number. For higher Froude numbers, more air is entrained within the flow. Two different mechanisms for air entrainment are found in hydraulic jumps. At the toe, where the supercritical inlet flow meets the overrolling structure, air is entrained into the water bulk along with the impinging jet. This constitutes the main source of air entrainment in the hydraulic jump. Then an additional air entrainment mechanism is found in the upper region of the roller related to interfacial fluctuations. However, this aeration mechanism is most prominent for high Froude number hydraulic jumps. The different aeration mechanisms are discussed in more detail elsewhere [60].

From a numerical perspective, the hydraulic jump constitutes a very challenging task due to its complicated flow pattern and transient nature. Numerical reproduction of this phenomena is the theme of Paper III, where guidelines on how to reproduce this flow, in a general-purpose finite volume CFD tool, is provided based on a thorough simulation campaign.

Chapter 3

Computational Fluid Dynamics

The work within this thesis constitutes efforts in predicting the flow features of aerated flows by numerical means. This involves solving the general equations for fluid motion – the Navier-Stokes equations. This chapter introduces these equations along with two different approaches to treat turbulence, RANS and LES, both of which are used within this work.

Introductory, (in Section 3.1) the general equations and the different approaches for turbulence treatment are briefly described, then the numerical methods applied in this work discussed in general terms (in Section 3.2-3.3), emphasising factors of significant importance for the results.

3.1 Equations governing fluid motion

As mentioned above, the motion of fluids is described by the Navier-Stokes equations, which are based on the basic principles of conservation of momentum and mass. Strictly speaking, the Navier-Stokes equations only consist of the momentum equations. However, it is currently quite common to include also the continuity equation into this term [1]. The latter terminology is adopted in the remainder of this work. These equations are expressed in different forms dependent on the properties of the particular flow. In this work, we treat the flow as incompressible, and in multiphase flows, we consider the fluids immiscible. For such flows, the Navier-Stokes equations take the following form

$$\frac{\partial \rho \mathbf{u}}{\partial t} + \nabla \cdot (\rho \mathbf{u} \otimes \mathbf{u}) = -\nabla p + \mu \left(\nabla \mathbf{u} + \nabla \mathbf{u}^T \right) + f \tag{3.1}$$

$$\nabla \cdot \mathbf{u} = 0. \tag{3.2}$$

Here ρ is the density, $\mathbf{u}$ the velocity vector, p the pressure, μ the dynamic viscosity, and f represents the sum of any body forces and surface forces, relevant for a particular problem.

Customised to the relevant problem, the above equations can describe the flow down to its smallest scales of motion within the computational mesh, in a direct numerical simulation (DNS). However, this requires a grid fine enough to capture the Kolmogorov scales, which results in dense meshes and demanding computations. These kind of computations are in general too demanding for high Reynolds number flows, which involves the majority of problems of interest for engineering applications. Therefore, the equations are normally transformed to make the solution procedure less computationally demanding.

A common approach for the above is to apply Reynolds averaging [51] to Navier-Stokes equations, and arrive at the Reynolds Averaged Navier-Stokes (RANS) equations. Here the above equations ((3.1)-(3.2)) are ensemble-averaged, where both the velocity and the pressure are divided into an averaged and a fluctuating part,

$$\phi = \overline{\phi} + \phi'.$$

Applied to the instantaneous Navier-Stokes equations, the averaging procedure results in the following equation set,

$$\frac{\partial \rho \bar{\mathbf{u}}}{\partial t} + \nabla \cdot (\rho \bar{\mathbf{u}} \otimes \bar{\mathbf{u}}) = -\nabla \bar{p} + \nabla \left(\mu \left(\nabla \bar{\mathbf{u}} + (\nabla \bar{\mathbf{u}})^T\right) - \rho \overline{\mathbf{u}' \otimes \mathbf{u}'}\right) + f \tag{3.3}$$

$$\nabla \cdot \bar{\mathbf{u}} = 0. \tag{3.4}$$

The equation set above looks quite similar to the instantaneous version, but the averaging procedure introduces the Reynolds stresses ($\rho \overline{\mathbf{u}' \otimes \mathbf{u}'}$) as an additional term in the momentum equation. Since this term cannot be directly expressed by the mean flow quantities, a modelling closure is needed. This is commonly approached by taking advantage of the Boussinesq eddy viscosity approximation [7], assuming that the anisotropic part of the Reynolds stresses can be modelled as structurally similar to the viscous stress. The Reynolds stresses can then be accounted for in an eddy viscosity term, which can be added to the physical viscosity in the momentum equation in an effective viscosity term $\mu_{\mathit{eff}} = \mu + \mu_t$.

Furthermore, models are needed to describe this eddy viscosity. This is done by turbulence models, where two-equation models like k-ϵ [36] and k-ω [64], and their derivatives are among the most used.

Another way to approximate the solution of the Navier-Stokes equations are by LES. Following this approach, the equations are rather filtered than averaged, which means that the smallest scales of the turbulent spectrum, known as subgrid scales (SGS), are filtered out and not resolved in the grid. This provides the possibility to capture the dynamics of turbulent eddies, and the corresponding capability to capture transient motions of the flow. Together with DNS, LES is known as scale-resolving or high-fidelity approaches to the solution of Navier-Stokes equations.

To decide on the threshold for the eddies to be included in the computations, a filtering kernel has to be selected. In a finite volume framework, this is commonly decided by the grid itself, giving a filter size equal to the cubic root of the local grid cell volume. To account for the stresses in the filtered out part of the turbulent spectrum, different SGS modelling frameworks are available in the literature. The most common approach is to employ the Boussinesq approximation, and by that assuming that the SGS are structurally similar to viscous stresses. The approximated stresses can be added to the physical viscosity, as done within the RANS framework described above. The Smagorinsky SGS model [55] and the WALE SGS model [45] are among the most used modelling frameworks for this purpose. Another suggestion for the modelling of SGS involves Implicit Large Eddy Simulations (ILES), see [26] for method reviews. This method was originally proposed for single-phase flow. The consideration behind it is that when applying an interpolation scheme with a substantial degree of upwinding, the dissipative error is expected to be of the same order of magnitude as the stresses modelled by a Boussinesq-type SGS model. Thereby its modelling can be omitted.

For aerated flows, the turbulence prediction is complicated by its interaction with the transient motion of the multiphase structures, which ideally should be captured in a turbulence model for this purpose. Nevertheless, none of the modelling closures that have found widespread use was developed with this goal in mind.

However, conventional two-equation models have been used to model aerated flows [39, 42, 49], which is also the case for the spillway simulations within this work. In the LES on the classical hydraulic jump, the ILES approach discussed above is chosen for the SGS. This means that modelling of these scales is omitted, and they are rather ignored.

As indicated above, the turbulence treatment approaches vary between the flows treated within this work. In some parts of the work (Paper I and II), the RANS equations are solved using two-equation models for turbulence, while other parts of the work (Paper III) treat the turbulence through an LES approach. Furthermore, single-phase simulations are performed for the settling basins, while the remaining work constitutes computations on air entrainment, and belongs to the two-phase flow regime. In the latter works, the Volume of Fluid (VoF) framework [29] is used to express and solve the fluid system. The principles of this method are outlined in Section 3.2.

3.2 Volume of Fluid

As mentioned above, the VoF framework is employed for the air entrainment computations within this work. This framework belongs to the interface capturing methods, which involves routines to track the surface between two immiscible fluids. In flows where these methods are used, the topological changes of the interface are of importance, and the fluids are normally not dispersed in each other. Among the interface capturing methods, the Levels Set method and VoF method are commonly used. A strength associated with the latter is its mass conservation.

According to the VoF framework, a single set of the Navier-Stokes equations (3.1)-(3.2) are solved for both phases, and the interface is located based on the volumetric fraction of the liquid phase α_l within the cells. Given the distribution of this α_l-field, the transport properties are calculated as a linear blending of the phases as

$$\rho = \alpha_l \rho_l + (1 - \alpha_l)\rho_{air}, \qquad \mu = \alpha_l \mu_l + (1 - \alpha_l)\mu_{air}. \tag{3.5}$$

Here ρ denotes the density μ the viscosity, and the indices l and *air* refer to water and air, respectively.

Within this two-fluid framework, the surface tension force f_s, embedded in f in (3.1), enters the picture. The Continuum Surface Force Model [8] is used to express this term in OpenFOAM®.

The core of the VoF framework belongs to the method used to actually capture the location of the interface. As mentioned above, this is done based on α_l, and one generally differs between algebraic and geometric methods. In the algebraic methods, an advection equation is used to distribute the phases according to the velocity field. While in the geometric methods, a sharp interface is conserved by transporting a geometrical reconstructed interface within each time step. In general, the geometric methods are considered the most accurate, but at the expense of efficiency.

In OpenFOAM®, the original VoF solver `interFoam` utilises an algebraic method to capture the interface. In the advection equation used in `interFoam`, a compression term is added to maintain a sharp interface, and the equation is expressed as

$$\frac{\partial \alpha_l}{\partial t} + \nabla \cdot (\mathbf{u}\alpha_l) + \nabla \cdot (\mathbf{u}^r(1 - \alpha_l)\alpha_l) = 0, \tag{3.6}$$

The third term represents the compression term. This term enforces sharpness of the interface by the velocity $\mathbf{u}^r$, which is aligned with the interface normal.

The geometric reconstruction alternative within OpenFOAM® is known as isoAdvector. This algorithm is available through GitHub, and also implemented as `interIsoFoam` in the newer OpenFOAM® versions from the ESI group.

As mentioned above, both interface capturing approaches are used in Paper III, where the routines are compared in terms of accuracy, stability, and computational costs. In Paper II, the algebraic alternative (Equation (3.6)), is used for interface capturing, however, the compression term in the α-equation is modified according to the description provided in Chapter 4.

3.3 Numerical Methods

The computations within this work were performed using three different versions of OpenFOAM®. Also, different solvers were used, including `interFoam`, `interIsoFoam`, `simpleFoam` as well as two customised solvers, `airInterFoam` and `spillwayFlow`. The latter was developed within this work and is described in Chapter 4.

However, all versions of OpenFOAM®, and the solvers therein, use a cell-centred finite volume framework (FVM), which also constitute the standard in industrial CFD. Within this framework, numerical schemes, boundary and initial conditions, linear solvers, as well as generation of the computational mesh, constitute important components and need attention from the user. The nature of these components, as well as consideration and perspectives regarding their implementations in the solution procedure, are briefly described in the proceeding sections.

Numerical schemes

An important component when solving the flow equations within the cell-centred FVM framework is the choice of numerical schemes for spatial interpolation and time integration. Within this framework, the values are contained in the cell centres and have to be provided as fluxes at the cell faces, which defines the purpose of the spatial interpolation procedure.

Generally, linear interpolation can be used for spatial interpolation. However, for the convective term, linear interpolation will lead to dispersive errors. And in RANS simulations, total variation diminishing (TVD) schemes are often used, which was also the case for the spillway simulations within this work.

A different approach is seen for LES and DNS. In such simulations, second-order unbounded schemes are commonly used, despite the known dispersive error. However, different from their RANS counterparts, these computations are run on high-density meshes, which in combination with small time steps, will minimise the appearance of these errors. While the linear interpolation scheme constitutes a general choice in such high-fidelity computations, a second-order upwind scheme commonly appears in industrial LES. The error introduced by this scheme is known to facilitate stability, which promotes its use in industrial settings. However, the stability comes at the expense of accuracy. Both the above schemes were applied within the LESs on the hydraulic jump executed within this work.

In `interFoam`, the boundedness of the α_l-field is ensured within the MULES framework, which is employed in the interpolation of the convective term in the α_l-equation (Equation (3.6)). This is a numerical flux limiting technique based on the Flux Corrected Transport theory [66], developed to guarantee boundedness in multiple dimensions.

For time integration, a higher-order scheme will provide more accurate predictions of transient behaviour. However, in cases where the steady-state behaviour is of interest, like in the spillway and sand trap simulations within this work, the choice of time integration scheme does not matter. By contrast, when the aim is to capture the dynamics of the flow, as in the current computations on the hydraulic jump, the order of the time integration scheme will, in principle, be of importance. However, considering the accuracy of the spatial interpolation schemes available in OpenFOAM®, the numerical errors can be expected to be dominated by these interpolations, at least when the time step is kept low.

Meshing

Due to the fact that the mesh defines the computational domain, its structure is of importance both for the accuracy of the results and the efficiency of the computations. As discussed briefly in Section 3.1, the obtainable accuracy of a simulation strongly depends upon the density of the computational mesh. However, a dense mesh leads to resource-demanding computations, and common practice is to refine the mesh in regions where gradients of resulting quantities are large, and where a dense mesh is needed to capture the phenomenon of interest. For the hydraulic jump regions around the toe and the roller will constitute the region of interest, and mesh refinement should be reasonable. Regarding the size of the domain, the mesh should be large enough to ensure that the investigated phenomena are not unintentionally affected by the boundary conditions. However, since the computational effort depends on the number of cells in the domain, the domain should not be disproportionately large.

A high-quality mesh promotes convergence and facilitates accurate and efficient simulations. Smoothness, skewness, and aspect ratio are measures used to quantify mesh quality. To conserve the smoothness of a mesh, regions of different cell density should be connected by a transition region with a gradual change in cell size. Furthermore, keeping the skewness close to zero, and the aspect ratio close to one tends to reduce the interpolation errors, which is desirable in terms of obtaining an accurate result.

Different mesh generators exist within OpenFOAM®. `blockMesh` is useful for simple meshes and was used to generate the mesh for the hydraulic jump simulations within this work. Then `snappyHexMesh` can be used when the computational domain contains more complex geometries, which applies to some of the sandtrap simulations within this work. Meshes generated by other tools can also be integrated, and different format converters exist.

Boundary and initial conditions

A particular problem is defined by its boundary conditions, which are meant to model the surroundings and drive the flow case. In general, one differs between Dirichlet and Neumann boundary conditions. In a Dirichlet boundary condition, a fixed value is imposed on the boundary. For a Neumann condition, the gradient of the quantity is fixed. Often a zero value is used for the Neumann condition, which means that the quantity does not change in the direction normal to the boundary. For a channel flow, a Dirichlet boundary condition is normally used at the inlet, whilst Neumann conditions often appears at the outlet. Similar set-ups were employed for the different simulation cases within this work. The values for the turbulence quantities at the inlet are usually not known in advance but are as common practice estimated based on turbulence intensity and length scale. A no-slip condition is often employed at the walls, which means that the velocity is zero at the walls. The turbulence treatment at the walls differs between RANS and LES. In the latter one usually try to resolve the turbulent boundary layer close to the wall, whilst in RANS simulations the turbulent quantities are normally calculated by wall functions in this region.

To start a computation, also initial values have to be provided for the different quantities. Proper estimates for the initial values promote convergence towards the solution. Therefore, often more detailed simulations are initiated by results from computations at coarser meshes.

Linear equation solvers

The equations systems in the different solvers used within this work are solved in a segregated manner according to the PISO/SIMPLE pressure-velocity coupling procedures. Leaving out the details of these algorithms, we note that the different equations are solved by linear equation solvers, which has to be specified by the user.

Dependent on the symmetry features of the equation matrices, different solvers should be used. In OpenFOAM® several choices of both symmetric- and non-symmetric solvers exist. The choice within each category should be of no importance for the accuracy of the simulation but might influence the convergence rate and simulation efficiency.

Chapter 4

Air entrainment modelling

To be able to capture air entrainment on a stepped spillway flow in a RANS simulation, an air entrainment model was developed within this work. The model was developed within the framework of `interFoam` and constitutes improvements to Lopes et al. [39]'s `airInterFoam`, developed from the same solver. Even if the theory behind the implemented air entrainment model is general in nature, the solver was developed for, and tested on, a stepped spillway, which led to its name `spillwayFlow`.

The air entrainment model can be divided into three components and constitute an air flux estimator, a transport equation for the volume fraction of air, and a coupling mechanism to integrate the air entrainment model into the VoF solver. The following sections describe these different components briefly, while a more thorough description of the model is provided within Paper II.

4.1 Estimating the flux of entrained air

The air flux estimator is meant to estimate the quantity of air to be transported passed some imaginary surface located below the interface. The expression for this term is adopted from the work of Ma et al. [41], and reads,

$$q = a \cdot \mathrm{Pos}\left(\nabla(\mathbf{u} \cdot \mathbf{n}) \cdot \mathbf{n}\right), \tag{4.1}$$

where,

$$\mathrm{Pos}(x) = \begin{cases} x, & x \geq 0 \\ 0, & x < 0, \end{cases}$$

and $\mathbf{n}$ is the interface normal defined as

$$\mathbf{n} = \nabla\alpha_l / \left(|\nabla\alpha_l| + \varepsilon\right). \tag{4.2}$$

Here ε is a small number added for numerical stability. a (in 4.1) is a length scale associated with the roughness of the interface due to turbulence and incorporates turbulence as a driving force for the air entrainment in the model.

The air flux estimator should be integrated within a source term in the transport equation for the volumetric fraction of entrained air. According to Ma et al. [41], it is assumed that the air entrainment is confined to a surface layer ϕ_{ent} thick, which value should be related to a characteristic length of a particular problem. Then, an expression for the source term of entrained air can be formulated as,

$$S_g = \frac{a}{\phi_{ent}} \mathrm{Pos}\left(\nabla(\mathbf{u} \cdot \mathbf{n}) \cdot \mathbf{n}\right) \delta_{fs}. \tag{4.3}$$

Here, also the surface indicator $\delta_{fs} \in [0,1]$ is included. The task of this function is to filter out the activation of the source term in non-physical regions, and robustness towards grid refinement constitute an important function property. The following section describes the δ_{fs}-function in the developed solver `spillwayFlow`.

Free-surface detection

The interface region is recognised by large gradients in several quantities, which can be used to identify these locations. Within the VoF framework, the volume fraction field α_l stands as a natural choice for this purpose, and the δ_{fs} function in the developed model was based on gradients of this quantity. The general idea when developing the δ_{fs}-function was to activate it fully in cells exceeding a critical gradient of $\nabla\alpha_l$, which was set relatively tight, and then expand its prevalence away from these locations according to an appropriate function or logic. The physical interpretation of this idea is that the largest amount of air will be entrained close to the h_{90}-surface, resulting in full activation of the δ_{fs}-function. Then, due to surface roughness, the region where air entrainment occurs will expand, which will be accounted for by non-zero values of δ_{fs}.

Different options for the expression of δ_{fs} were explored, including the tanh-based function adopted in `airInterFoam`. However, testing of the tanh-based function revealed that its performance was hard to control upon grid refinement, and alternative functions were considered. The latter included a parabola-based, and a purely distance-based function, ending up at a blending of the two. The parabola based function was expressed as

$$\delta_{fs}(\nabla\alpha_l) = \begin{cases} \mathrm{Pos}\left(-\frac{1}{4d}\left(|\nabla\alpha| - |\nabla\alpha_{cr}|\right)^2 + 1\right) & \text{if } \nabla\alpha < |\nabla\alpha|_{cr} \\ 1 & \text{otherwise.} \end{cases} \tag{4.4}$$

Here, $|\nabla\alpha|_{cr}$ yields a critical value for the gradient in the volume fraction α_l. Its value is set to depend on the cell size of the computational mesh Δx as, $|\nabla\alpha_l|_{cr} =$

$1/(4\Delta x)$. Furthermore, d refers to the distance from the vertex of the parabola to its focus, which can be computed as

$$d = 0.25\left(\nabla\alpha_{cr} - \nabla\alpha_{cut}\right)^2,$$

where $\nabla\alpha_{l,cut}$ is an input parameter explicitly defining the lowest $\nabla\alpha_l$ for which the source term may assume non-zero values. The function above was further combined with a distance cut-off, where δ_{fs} was set to zero in cells located further than a distance ϕ_{ent} away from a *sharp* interface defined by $|\nabla\alpha_l|_{cr}$.

The non-zero values of the function are always fixed to the interval $[\nabla\alpha_{l,cut}, \nabla\alpha_{l,cr}]$, which expands upon grid refinement. For the simulations within this work, $\nabla\alpha_{l,cut} = 20$ coupled with $\nabla\alpha_{l,cut} = 1/(4\Delta x)$ were found appropriate and used for all cases.

4.2 The α_g-equation

As mentioned above, the source term (4.3) is introduced into a transport equation for the modelled volume fraction of entrained air, α_g, expressed as,

$$\frac{\partial\alpha_g}{\partial t} + \nabla\cdot(\mathbf{u}_g\alpha_g) + \nabla\cdot(\nu_t\nabla\alpha_g) = S_g. \tag{4.5}$$

Here ν_t is the turbulent viscosity, and $\mathbf{u}_g$ is the velocity of the entrained air, which is set equal to $\overline{\mathbf{u}}$ in our model.

The purpose of the new field α_g is to transfer the entrained air, calculated by the source term, into the α_l-field within the VoF framework. Whenever the α_g-field exists independent of the α_l-field, it can be interpreted as the volume fraction of entrained air (in a particular cell) that could not be captured by the original solver. However, in our model a two-way formulation is applied, which makes the physical meaning of the α_g-field somewhat unclear. Nevertheless, its function is to transfer the effects of entrained air predicted by an air flux estimator, into the α_l-field within the VoF framework.

Modelling air propagation into the corners of the steps

By definition, the air entrainment model introduces air within a surface region close to the h_{90}-surface. The introduced air is then transported along with the flow governed by the α_g-equation. Initial experience with the solver showed that the transport of α_g in (4.5) is dominated by the convective term, and that only limited amounts of air is transported away from the surface. By contrast, in the experimental data by Bung [10], air fractions are found all the way to the pseudo-bottom. Pfister and Hager [47] illustrated the physical mechanism leading to this aeration as a transient generation of air troughs extending from the surface into the bulk flow, where they occasionally hit the step edges and get distributed into the steps.

This transient process is hard to capture in a steady-state simulation, and an ad-hoc approach taking advantage of the diffusion term found in (4.5) was used. More specifically, a factor C_t was added in front of the diffusion term, to magnify its effects. The modified α_g-equation then reads,

$$\frac{\partial \alpha_g}{\partial t} + \nabla \cdot (\mathbf{u}_g \alpha_g) + C_t \cdot \nabla \cdot (\nu_t \nabla \alpha_g) = S_g. \tag{4.6}$$

Here $C_t = 150$ was chosen as a default value based on a broad range of step Froude number simulations.

4.3 Coupling to the VoF solver

In the two-way coupling herein, the air entrainment model is coupled to the VoF solver through manipulation of the artificial compression term in the α_l-equation (3.2),

$$\nabla \cdot (\mathbf{u}^r (1 - \alpha_l) \alpha_l) \, . \tag{4.7}$$

The overall idea is to reduce α_l in regions where α_g is large, and at the same time maintain mass conservation. In the α_l-equation (3.2), the term above (4.7), is originally meant to impose compression at the interface, and the part

$$(1 - \alpha_l)\alpha_l = \alpha_{air}\alpha_l \tag{4.8}$$

is meant to activate this compression close to the interface. In our model we modify this term to introduce negative compression in locations where $\alpha_g > \alpha_{air}$, and thereby influence the α_l-field in these regions. This is done by subtracting α_g from α_{air} in (4.8), arriving at the following expression for the α_l-equation,

$$\frac{\partial \alpha_l}{\partial t} + \nabla \cdot (\overline{\mathbf{u}} \alpha_l) + \nabla \cdot (\mathbf{u}^r (\alpha_{air} - \alpha_g) \alpha_l) = 0. \tag{4.9}$$

Accordingly, the model is active only when $\alpha_g > \alpha_{air}$. In other regions, the compression term (4.7) maintains its original function.

4.4 Inception point estimation

Recall from Section 2.1 that air entrainment is enforced at the free-surface when the turbulence forces at the interface exceed the stabilising forces of surface tension and buoyancy. Within the current model, this force balance is implemented into a parameter-free activation criterion, according to the formulation of perturbating (P_t) and stabilizing (P_d) forces given by Hirt [28],

$$P_t = \rho k, \tag{4.10}$$

$$P_d = \rho |g| a + \frac{\sigma}{a}. \tag{4.11}$$

Here σ represents surface tension, ρ density, and g the acceleration due to gravity. According to the mentioned force balance, the model is activated when $P_t > P_d$.

In addition to this parameter-free activation criterion, the original criterion used in `airInterFoam` is kept within the new solver. Here aeration is activated based on critical values for the turbulent kinetic energy k_c, and velocity u_c, at the free surface according to

$$k > k_c \quad \text{and} \quad \bar{\mathbf{u}} \cdot \mathbf{n} > u_c \quad \text{and} \quad \bar{\mathbf{u}} \cdot \mathbf{g} > u_c, \tag{4.12}$$

where k_c and u_c has to be provided by the user. Since the appropriate critical values depend not only on the flow but also on the turbulence model, these values are not easy to predict in advance. Careful calibration for the selected turbulence model and flow case is therefore necessary.

Chapter 5

Summary of the main results

This chapter provides a summary of the main findings obtained during this research. The presentation is divided into three parts. The first part is devoted to highlighting the influence of modelling parameters in numerical computations. Due to the fact that all of the three scientific papers point out the significant effect the different modelling parameters might have on the numerical predictions, this yields an introductory part to the presentation of the main findings. Within this part, examples are included from all of the three scientific papers.

The last two sections (Section 5.2-5.3) provide results from numerical simulations on two different hydraulic engineering applications – a stepped spillway, and a classical hydraulic jump. For the computations on the stepped spillway, the developed air entrainment solver (Chapter 4) is tested, and for the hydraulic jump a scale-resolving approach is employed.

5.1 Examples of dependence on modelling parameters

The importance of the choice of modelling parameters on numerical results is well known in the community of numerical modellers. The same is true about the importance of proper validation of the results by experimental data. Nevertheless, as noted by Chanson [15], many CFD analyses in hydraulic engineering show a lack of proper verification of the numerical techniques. Also, validation of the results tends to be poor, often relying on depth-averaged quantities. Furthermore, [15] addresses the lack of proper verification and validation to a possible lack of knowledge of available mathematical methods to perform such analyses among general CFD users. Similar concerns were expressed by Blocken and Gualtieri [4], in their publication of necessary iteration steps to verify a numerical model.

The following subsections provide examples of how the turbulence model, different numerical schemes and parameters may influence the computation. The choices lead to slightly, considerable, or completely different results. The above was the theme of Paper I (A.1), showing multiple solutions of Navier-Stokes equations for sand traps, and for Paper III (A.3), examining the influence of modelling parameters on the predictive accuracy of LES on a classical hydraulic jump, and also within the grid dependency study on the stepped spillway in Paper II (A.2).

5.1.1 Dependence on turbulence modelling

As can be adopted from the description given in Chapter 3, the choice of turbulence modelling regime and turbulence model is of importance for the results. The proper choice depends on the needed accuracy, the available resources, as well as the properties of the flow. The following two sections provide examples of solutions of the RANS equations, using different turbulence models. First, a classical hydraulic jump is considered, then results for sandtrap simulations are provided.

Classical hydraulic jump – RANS

In the process of looking into the classical hydraulic jump, reproduction of the experimental results by Murzyn et al. [44] on a hydraulic jump with inflow Froude number 4.8, was carried out. These simulations were performed with `interFoam`, using the realisable k-ϵ turbulence model. Identical simulations have been published by Witt et al. [65], and our simulations were done in terms of validating a general set-up for a classical hydraulic jump.

However, in the process of working with this jump it was noted that by employing different versions of the k-ϵ turbulence model, significant differences were seen for the predicted flow field, also affecting the distribution of air inside the jump, as shown in Figure 5.1. The results provided using the realisable k-ϵ model gave values close to the experimental counterparts by Murzyn et al. [44], and in accordance to the simulations published by Witt et al. [65], using the same numerical solver and set-up. This shows the importance of choosing the proper turbulence model for a particular case. Such information is normally found in the documentation of a particular turbulence model, or based on computations of similar flows reported in the literature. Often these sources can at least be used as a starting point for the testing of different turbulence models on a particular case. Recall from Section 2.3 that the hydraulic jump is characterised by an inflow jet and a surface roller with an overturning recirculating flow, and a shear region separating the two. This constitutes features where the realisable k-ϵ has been proven to perform superior to the standard k-ϵ model, which was also the case for the results shown in Figure 5.1.

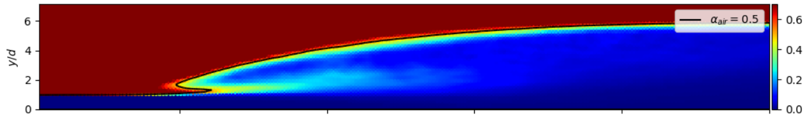

(a) realisable k-ϵ

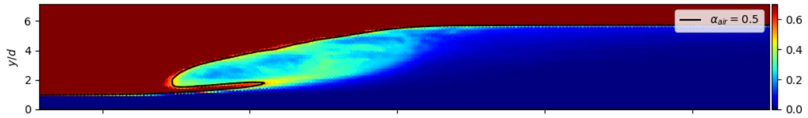

(b) k-ϵ

Figure 5.1: Comparison of simulations of a classical hydraulic jump with inflow Froude number 4.8 using different versions of the k-ϵ turbulence model.

Settling basin simulations

Paper I reports findings where the path of the main water jet proceeding an expansion zone, varied depending on the employed modelling parameters. These simulations were done on settling basins, also referred to as sandtrap, where the efficiency of the structure might depend on the path of the main jet and the accompanying recirculation zone. In simulations of one of the sandtraps, the main jet was predicted on different sides in the upper part of the tunnel dependent on the choice of turbulence model (see Figure 5.2). Interestingly, according to the

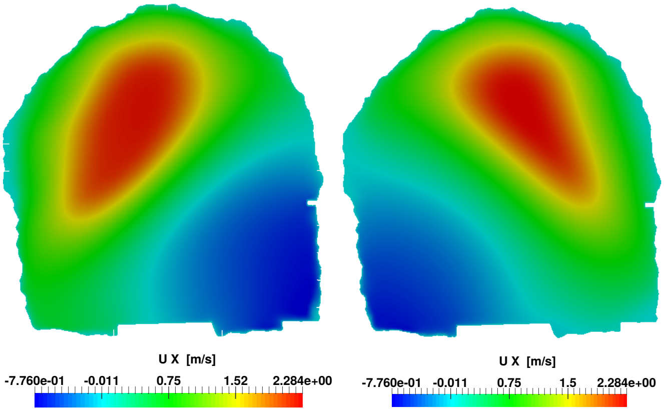

(a) RNG k-ϵ **(b)** k-ϵ

Figure 5.2: Streamwise velocity profiles (u_x) of a cross section in Tonstad sand trap. The path of the jet at this cross section alters completely when the turbulence model is changed from the standard $k - \epsilon$ to the RNG $k - \epsilon$ model.

field measurements, the jet follows the tunnel centre, which is not captured by these computations. The only means of validation for these simulations were velocity measurements, taken at a horizontal line at different lengths downstream the expansion zone. This makes it difficult to analyse the phenomena in details. However, the purpose of this work (Paper I) was more to highlight the effect of changing the turbulence model for this particular simulation, and not actually to state the preferable one.

Even if these simulations were performed at settling basins, the highlighted issues might relate to other hydraulic components as well, and to CFD computations in general.

5.1.2 Grid sensitivity

A basic requirement for a CFD calculation is to obtain a grid independent solution. However, this might not always be obtainable within the available resources or time frame. The following sections show some cases where the effects of grid refinement are considered.

Settling basin simulations

Figure 5.3 shows the effects on the lateral velocity profile a certain distance downstream the tunnel expansion when the grid is refined in simulations on one of the settling basins reported in Paper I. Dependent on the density of the grid, the jet follows the left, right, or the centre of the tunnel. Remarkably, the coarsest grid

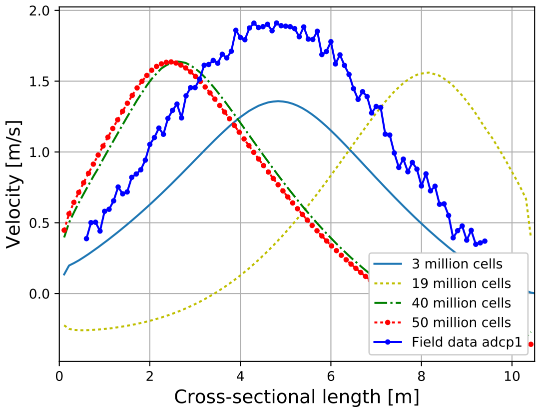

Figure 5.3: Lateral profiles of streamwise velocities (u_x) from the ADCP at Tonstad sand trap using different grid resolutions. The cases were calculated on four different grids containing 3 million, 19, 40 and 50 million cells respectively.

predicts the jet in the middle of the tunnel, which is in accordance with the field measurements. The actual reason for this was not thoroughly investigated in the paper, but most probably the employed modelling was not accurate enough to capture the considered phenomenon, and further investigation would be needed to reveal the actual causes.

Classical hydraulic jump

A central aim of the LES simulations on the hydraulic jump (Paper III) was to investigate the influence of different modelling parameters on the predictive accuracy of the computations. Of considerable importance for industrial use of LES, is the computing time needed to perform a particular simulation. This is governed by several modelling parameters, the grid density being among the most crucial. Acknowledging that more details of the flow can be captured by a denser grid, analyses within this work provide measures on how the predicted accuracy of different flow quantities is reduced by gradually coarsening the grid. Figure 5.4 illustrates how the prediction of the turbulent kinetic energy k is affected by the grid coarsening. At the finest grid ($\Delta x2$), several modelling parameter combinations are able to capture the structure of k with relatively good accuracy. This is true even at the location closest to the toe ($x' = 0.5$). Due to the flow structure, this location is more challenging to capture numerically than the locations further downstream ($x' = 1$, $x' = 2$). The second coarsest grid ($\Delta x3$) still captures the main features relatively accurate, but at the most downstream length ($x' = 2$), a non-physical peak starts to emerge. At the coarsest grid ($\Delta x3$), most of the parameter combinations fail to predict this quantity.

Stepped spillway

As noted several times above, a grid dependence study is an integral part of a CFD-analysis. However, the reliability of such studies depends on choosing a quantity suitable for the model, and phenomena under inspection, to be included in the grid dependency study. An example of how this can go wrong can be provided from the stepped spillway simulations within this work (Section 5.2). These computations aimed to predict the aeration of stepped spillway flows. Here, testing of `airInterFoam` (AIF) revealed that air entrainment features like void fraction and surface height, were very sensitive to grid refinement (see Figure 5.5(b)). Nevertheless, looking at the velocity, the situation was different, and the computations seem to be grid independent already at the coarsest grid G1 5.5(a). However, this model is meant to capture aeration of the flow, and a quantity describing an air entrainment feature would be the proper choice to examine in a grid dependence study.

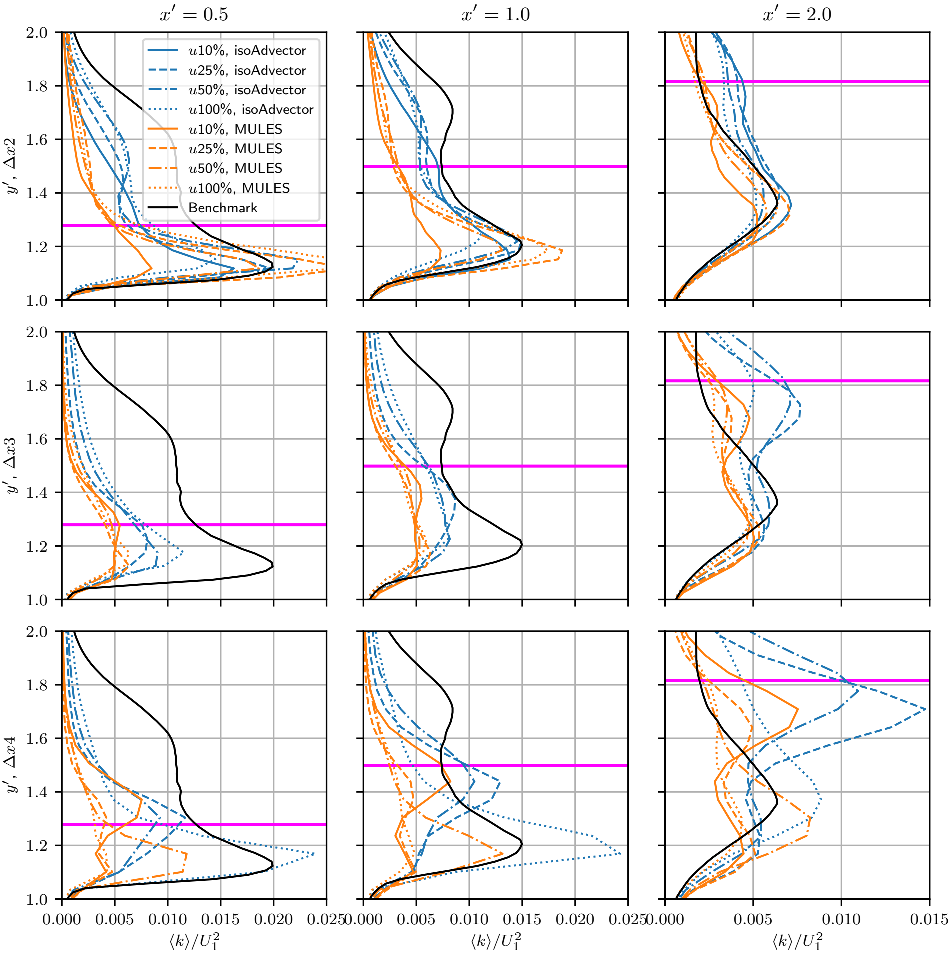

Figure 5.4: The profiles of $\langle k \rangle / U_1^2$ obtained in the simulation campaign. x' denotes the distance from the toe of the jump.

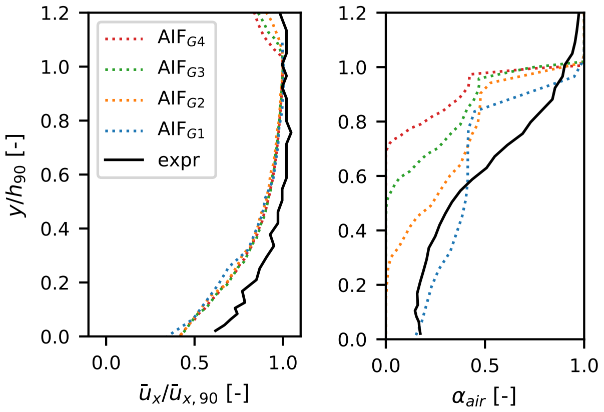

(a) Velocity **(b)** Void fraction

Figure 5.5: Grid sensitivity of the different result parameters, velocity and void fraction. Vertical profiles for uniform flow conditions for step Froude number F_s=2.7. `airInterFoam` (AIF) simualtions for different grids compared to experimental results by Bung [10].

5.1.3 Discretization scheme

As emphasised in Section 3.3, the choice of schemes for spatial interpolation of the convective terms can be of great importance in terms of stability and accuracy of a numerical simulation. Due to the fact that the mentioned properties not necessarily reinforce each other, one might have to consider compromising accuracy in favour of stability. However, in a CFD computation it is important to have an idea of which interpolation scheme is suitable for different flows, as well as a decent knowledge about the effects of applying a more accurate scheme. The following section provides examples from computations resulting in substantial changes in the flow field by changing interpolation schemes. These examples are from the sandtrap simulations (Paper I). Next, some examples from the hydraulic jump simulations (Paper III) are provided. Here the effects on the predictive capabilities of the solver are inspected when using gradually less accurate schemes.

Settling basin simulations

Figure 5.6 illustrates results from one of the sandtrap computations included in Paper I. Using the second-order upwind scheme, the jet follows the sandtrap bottom, while the first-order interpolation scheme predicts this high-velocity zone close to the surface. Interestingly, the latter shows good accuracy towards measurements. The fact that the first-order discretisation scheme predicts a more correct velocity field than a second-order scheme is remarkable as most guidelines for CFD

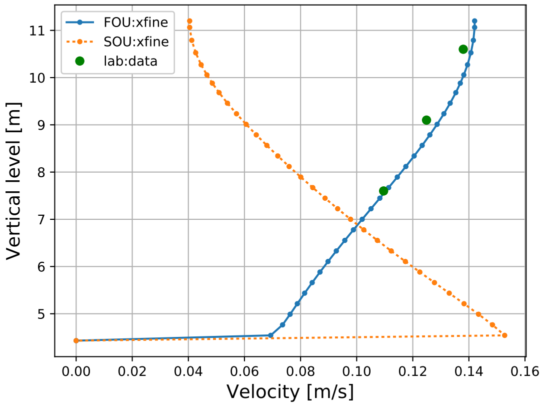

Figure 5.6: Computed and measured velocities in streamwise direction (u_x) for a vertical line 67.5 m downstream the inlet of the sandtrap. The labels refer to the discretization scheme, FOU=first order upwind scheme, SOU=second order upwind scheme.

computations recommend the usage of a second-order scheme.

Classical hydraulic jump

While the purpose of the sandtrap simulations was more to exemplify that (completely) different solutions were produced employing interpolation schemes of different order of accuracy, without investigating the phenomenon thoroughly, the contrary was true within the work on the hydraulic jump (Paper III).

Recall from the method description in Section 3.3, that the stability of a computation might improve by the application of more dissipative schemes for spatial interpolation of the convective term in the momentum equation. To that end, the second-order upwind scheme is commonly used. Within the work on the hydraulic jump, the above issue was addressed by employing a linear blending of the central difference scheme and the second-order upwind scheme, testing the effect of upwinding by gradually increasing its linear weight. Somewhat surprisingly, the overall best accuracy for several of the interesting quantities was obtained at high degree of upwinding. This is also reflected in the turbulent kinetic energy profiles (Figure 5.4). Here the degree of upwinding is identified by its percentage in the labels.

As given above, a positive effect of higher degree of upwinding can be a more stable velocity field, where parasitic errors are avoided. However, the increased stability will be on the expense of resolving small-scale turbulent motions, leading to a less accurate prediction of the velocity field. Nevertheless, more accurate predictions for several of the interesting quantities were provided using a high degree of upwinding. Even if this result was a bit surprising, one should keep in mind that any parasitic error in the velocity field will be transferred into the advection of the interface. This will affect the prediction of aeration features like the void fraction.

5.2 Numerical modelling of stepped spillways

Recall from Section 2.2 that air entrainment for skimming flow along a stepped spillway belongs to the interfacial air entrainment mechanism, where air is entrained into the flow from turbulence close to the surface. As mentioned in Section 2.2, no studies using VoF (RANS or LES), without external air entrainment modelling, have been reported to succeed in reproducing self-aeration along a spillway. A reason might be that such simulations have not been attempted. Another possibility is that these simulations are too complex.

However, most probably it should be possible to reproduce self-aeration at a spillway using a high-fidelity approach, coupled with an interface capturing method. On the other hand, the air bubbles formed as white water in a spillway flow will be very small and their number very large. To capture the fate of the single bubbles will therefore be very computationally demanding, and most likely not suitable for engineering applications.

From RANS computations within this work using `interFoam`, no air entrainment was seen for 2D simulations, even on very fine grids, and neither on moderately refined 3D grids. For all simulations, the free surface was steady, with no fluctuating features. This indicates a total disability of `interFoam`, ran in RANS mode, to capture the self-aeration process, even on grids that should be small enough for the physical scales to be captured. However, the outcome of this is that no aeration occurs, which motivates the need for an additional air entrainment model to capture air entrainment for these kinds of flows. A major part of the work within this thesis was devoted to this theme, where an air entrainment model was developed. A description of this model is given in Chapter 4, while a summary of results applying the model on stepped spillway flows are provided in the following section.

5.2.1 Testing of air entrainment models

In this part of the work, the focus was devoted to the development of a highly efficient approach for the calculation of aerated spillway flow, combining the interface capturing solver in OpenFOAM®(`interFoam`) with additional modelling of air entrainment. The work aimed to develop a model able to reproduce important self-aerating features of a general stepped spillway flow in the skimming flow regime.

Through a review of relevant literature it was found that the model `airInterFoam` [39] was already implemented in OpenFOAM®, and validated on a stepped spillway. Due to its possible potential for use in hydraulic engineering applications, further testing of this solver was of interest and constitutes the first part of the analyses within this work. An extensive simulation campaign, including four different step Froude numbers, sensitivity to model parameters and grid resolution, was applied to carefully evaluate the performance of the solver.

The conducted simulation campaign included four different step Froude numbers in the range, $2.7 \leq \mathsf{F_s} \leq 13$. These conditions were chosen to match experimental model cases executed by Bung [10], which were used to validate the results. Important areation features like void fraction profiles and surface elevation were used to evaluate the performance of the models. Corresponding simulations using `interFoam` (IF) were preformed and included as a reference in the validation of the results. The main results are summarised in the following sections.

Tesing of `airInterFoam`

Applying similar settings as reported in [39], `airInterFoam` (AIF) was identified to perform reasonably well for the chosen range of $\mathsf{F_s}$, both in terms of void fraction, surface elevation and velocity. An example of this is shown in Figure 5.7 for the void fractions in the uniform region of the spillway.

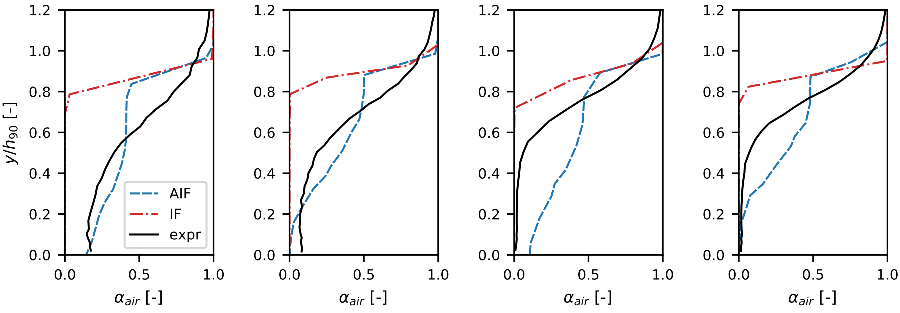

(a) $\mathsf{F_s}$=2.7 **(b)** $\mathsf{F_s}$=4.6 **(c)** $\mathsf{F_s}$=8.28 **(d)** $\mathsf{F_s}$=13

Figure 5.7: Vertical void fraction profiles for uniform flow conditions. Spillway flows with different Froude numbers at the coarsest grid G1. `airInterFoam` (AIF) simulations compared to `interFoam` (IF) simulations and experimental results by Bung [10].

While the model were shown to perform reasonably well for the tested $\mathsf{F_s}$ on the coarsest grid, G1, its predictive accuracy was significantly reduced when the grid was refined, finally approaching the behaviour of IF. Figure 5.8 illustrates how the predicted surface height approaches the corresponding IF-prediction upon grid refinement. The black lines show experimental values. The difference between the solid and the dashed black lines, respectively representing the h_{90}-line and the equivalent clear water depth, illustrates the importance of considering air entrainment when calculating spillway flow.

Note from Figure 5.8 that a higher surface is predicted by IF at G1 then for AIF at G4. This indicates that more air is *entrained* using IF at the coarsest grid, than

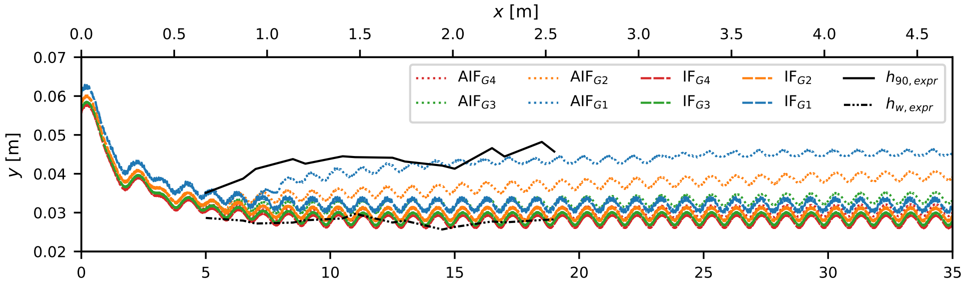

Figure 5.8: Surface elevation for AIF simulations at different grids (G1-G4) compared to IF simulations and physical model results by Bung [10]. F_s=2.7.

using AIF on the finest grid, and is a purely numerical effect. The main cause of this is that less numerical diffusion contributes to the transport of the entrained air as the grid is refined. However, inspection identifies shrinkage of the region in which the source term in the air entrainment model is non-zero as an additional cause.

Motivated by the fact that the effects of the air entrainment model were reduced, and partly ceased to work, upon grid refinement, efforts on developing the model were made, resulting in the improved solver `spillwayFlow` (SPF). The proceeding section summarises the modelling efforts towards the developed solver, and shows the main results obtained with it.

Developments

Recall from Section 4.3 that air was introduced at the free-surface by negative compression of the interface. Then, to be able to approach some kind of grid independence, the uncontrolled numerical diffusion should be kept to a minimum, while introducing diffusion by negative compression of the interface at locations decided by the solver.

Extensive testing of the different parameters available within the model were executed in an effort to adjust the behaviour of the model. The approach was to look at the possibilities of broaden the region where the source term was active, which could be justified by the fact that the surface is roughened as air is entrained. Then the free surface is transformed into a region of white water, and the resulting scenario is that air will be entrained at a broader region.

Finally, developments including adjusting the surface indicator function and adding a diffusion term to the α_g-equation were purposed to improve the solver's behaviour, in the new solver. The purposed developments, as well as the principles behind the original model, are given in Chapter 4.

The developments gave improved behaviour for all $\mathsf{F_s}$-cases, and the solution became substantially more robust towards grid refinement. Nevertheless, as shown in Figure 5.9, complete grid independence was not obtained.

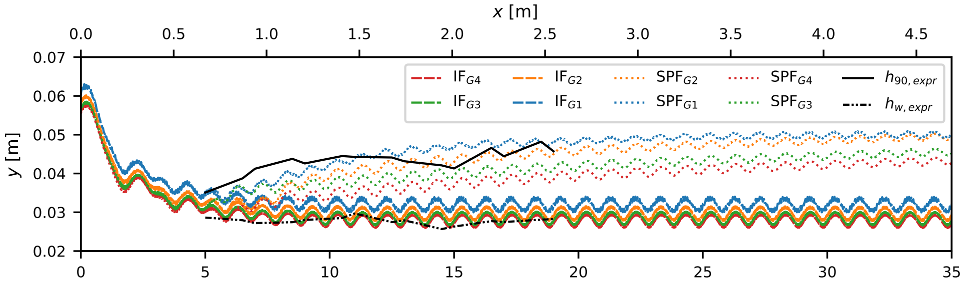

Figure 5.9: Surface elevation for SPF simulations at different grids (G1-G4) compared to IF simulations and physical model results by Bung [10]. $\mathsf{F_s}$=2.7.

Within this solver, efforts implementing a parameter-free air entrainment activation were also performed. Since the location of the inception point is of crucial importance for the operation of a stepped spillway, this would be very beneficial to achieve. The implemented criteria were based on Equation (4.10)-(4.11), which model a force balance between perturbing and stabilising forces at the interface. Unfortunately, results showing sensible results were only possible to achieve using the variable density corrected turbulence framework by [24]. The latter might indicate turbulence to be more accurately predicted by this turbulence modelling framework. Even though the activation criteria were proven to perform well for certain $\mathsf{F_s}$, its performance could not be considered sufficiently accurate on a broad range of step Froude numbers.

Using the above activation criteria, the aeration activation depends solely on the predicted turbulence. As noted in Section 1.2, turbulence prediction is not easy in the proximity of the free surface for a multiphase flow, which might explain the observed challenges.

5.3 Numerical modelling of hydraulic jumps

The fact that the hydraulic jump is the most used energy dissipator in hydraulic engineering, as well as its complex flow structure, makes it a relevant case for testing the predictive capabilities of a numerical solver towards aerated flows. Also, much research has been done at the classical hydraulic jump, which makes it a preferable choice in terms of validation.

Our starting point on the investigation of the hydraulic jump was to reproduce the experimental results by Murzyn et al. [44], containing data for four different inlet Froude number jumps (2.0, 2.4, 3.7, 4.8). Similar to what was reported by Witt et al. [65], the jump with Froude number 4.8 was reproduced in good agreement to the experimental data using `interFoam` and the realisable k-ϵ-model for turbulence modelling. However, the grid resolution needed to capture the bubble size range necessary to produce results in good agreement to the experimental data were at a range also suitable for LES.

Due to the above, and also acknowledging the uncertainty related to the turbulence modelling and ensemble-averaging (ref Section 1.2), it was decided to use a scale-resolving procedure in this work. To that end, DNS results for a hydraulic jump of Froude number 2, were found as a suitable reference for validation. The quality of these data for validation purposes was considered to overcome the fact that the most interesting jumps in industrial settings belong to the Froude number range [4.5,9].

The following sections summarise the purpose of, and main results from, our LESs performed on a classical hydraulic jump with inlet Froude number 2. The numerical methods used in the work are described within Chapter 3, and a thorough presentation of the results is provided in Paper III, available in Appendix A.3.

5.3.1 LES of a hydraulic jump with Froude number 2

The purpose of the work was two-fold. A central aim was to produce the best results achievable with the numerics available within the framework of the employed solvers (see Section 3.3), and thereby reveal whether OpenFOAM® is capable of reproducing this kind of flow using scale-resolving approaches. This is a costly simulation, not intended for industrial use, but useful in terms of understanding the physics of the flow. An equally important aim was to investigate how the accuracy of the simulations is reduced when applied to coarser meshes and cheaper numerical methods, which can be available for engineering purposes. Based on a thorough simulation campaign, this will provide guidelines for the use of LES for this flow, considering accuracy on the one hand, and computation effort and stability issues on the other. Following from the fact that the hydraulic jump computations referred to herein were LES, they were carried out on a three dimensional computational mesh.

Benchmark case

As already mentioned, the first part of this work constituted an effort on reproducing the best results possible to achieve with the numerics available in the solver. In this part of the work, the DNS simulation by Mortazavi et al. [43] is used as a reference.

To arrive at an accurate prediction, the theoretical height of the jump $(d_2 - d_1)$ was discretized by 81 cells, and a total of 83 million cells were utilised for the computational mesh. The cell sizes in the region involving the jump were comparable to the corresponding measure employed in the DNS reference [43]. In this region the mesh consisted of cubic cells, which can be considered optimal in terms of numerical efficiency. The `interFoam` solver was employed in this simulation, which means that the algebraic interface capturing scheme was used. As mentioned in Section 3.2, geometric interface capturing is considered more accurate. Since the intention in this part of the work was to push the accuracy to its limit within OpenFOAM® this routine appears as a natural choice. However, due to stability issues, only the `interFoam` simulations were able to produce reliable results. Nevertheless, `interFoam` constitutes the original routine for VoF calculation in OpenFOAM® and is available in all OpenFOAM® versions, which also defends its use in the current context.

The computations gave results close to the reference DNS simulation for most of the considered flow features. Figure 5.10 and 5.11 show some key results from this simulation, illustrating the resulting void fraction and velocities from the toe ($x' = 0$), and at several locations downstream. Especially, the void fraction plots

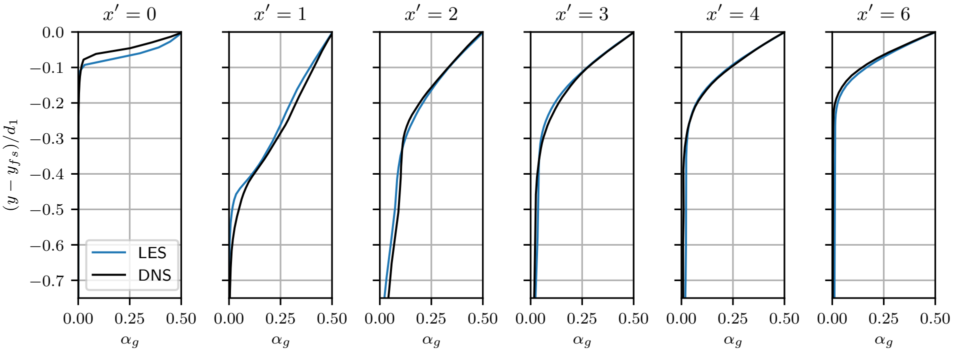

Figure 5.10: The profiles of $\langle \alpha \rangle$ in the benchmark simulation.

show impressive correspondance with the DNS simulation. Here, the different curves can only be clearly separated at the locations closest to the toe, which constitute the most transient region within the jump, and therefore appear as the most demanding region to reproduce. Good accuracy is also achieved for the velocities (see Figure 5.11), with an exception for the air-phase velocities close to the toe. However, the velocities in the water-phase are predicted in accordance with the reference also in these regions. In addition to void fraction and velocity, turbulent measures and higher-order moments of velocity were inspected and found to agree well with the corresponding DNS results.

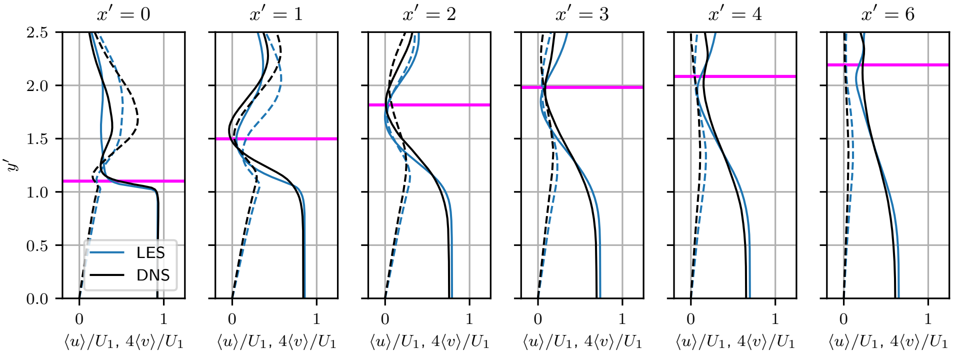

Figure 5.11: The profiles of $\langle u \rangle$ and $4\langle v \rangle$ obtained in the benchmark simulation. The magenta line shows the location of the interface.

As an overall impression, these result proved that high-quality reproduction of an aerated flow, as the hydraulic jump, is achievable using the general-purpose finite volume based code OpenFOAM®.

Instabilities

Despite the impressive accuracy achieved with the high-resolution efforts, stability issues were experienced in several of the simulation attempts. These challenges were addressed to two possible causes; the treatment of the surface tension by the Continuous Force Model, and the treatment of the gravity term in the momentum equation, both which might result in acceleration of the flow.

Caused by a numerical imbalance between the surface tension and the pressure gradient across the interface, the Continuous Force Model model can produce parasitic currents across the interface between the phases [11]. Furthermore, a segregated pressure-velocity coupling algorithm like PISO can give rise to a numerical imbalance between the dynamic pressure gradient and the density gradient terms, which might result in high velocities in the gas phase close to the surface.

The nature of these possible issues leads to the fact that a denser grid and a more detailed interface capturing approach not necessarily promotes a more stable simulation, which stands in contradiction to the case of a single-phase LES, where a denser grid dampens instabilities.

Influence of modelling parameters

As indicated above, an aim for this work was to develop a methodology and thereby provide guidelines for the use of scale-resolving modelling of the classical hydraulic jump. To be able to provide such guidelines, the most important modelling parameters have to be considered. Recall from Chapter 3, that the accuracy of the result of a multiphase VoF simulation depends on modelling parameters like the choice of interface capturing routine, the employed interpolation scheme for the convective terms, and on the density of the grid. This results in a need to consider the optimal balance of accuracy, stability, and computation costs for a particular simulation case, which motivate the extensive simulation campaign performed in this work.

As given in Section 3.2, and briefly discussed above, two different interface capturing schemes are publicly available for OpenFOAM; the algebraic formulation, within `interFoam` and the MULES framework (referred to as MULES in the following), and isoAdvector, which captures the interface through a geometric reconstruction of the surface. The simulation campaign performed in this work, revealed that the geometric reconstruction alternative, isoAdvector, defeats its algebraic counterpart in terms of accuracy. Therefore, this scheme is preferable if tracking the fate of the entrained bubbles is of importance. Furthermore, this interface capturing scheme led to more time-consuming computations, and was generally more prone to stability problems, compared to the algebraic alternative.

The density of the grid is a substantial contributor to the cost of a particular simulation. An important purpose of this work was, therefore, to inspect the resulting accuracy as the grid was 2, 3 and 4 times coarser than the one applied in the benchmark simulation. As expected, all resulting quantities showed the best accuracy on the most refined grid. This was especially true in the regions closest to the toe, which constitute the most chaotic regions. Here, only the $\Delta x2$-grid where able to reproduce the results from the benchmark simulation with acceptable accuracy. However, the largest grid dependence was found when inspecting the turbulent kinetic energy k (Figure 5.4). The effect of grid resolution on this quantity was discussed in Section 5.1.

As noted in Section 3.3, some degree of upwinding within the spatial interpolation of the convective term in the momentum equation might be advantageous in terms of computation stability. Employing a linear blending of the second-order upwind scheme and the linear interpolation scheme, the investigation within this work revealed that the degree of upwinding affects the resulting velocity field to a small extent, but noticeably affects the α-field. As a general result, more accurate reproduction of the α-field was seen for high degree of upwinding. This indicates that a stable velocity field might be more important than reproducing steep velocity gradients in terms of predicting an accurate α-field. This was further discussed in Section 5.1.

Summarised the combination of parameters resulting in the best overall accuracy was isoAdvector interface capturing method on the densest grid ($\Delta x2$), combined with 100% upwinding. This parameter combination is then recommended for simulations where accuracy is of crucial importance, and cannot be compromised in favour of simulation costs and stability. Changing the interface capturing scheme to MULES, reduces simulation costs, and results in more stable simulations. These settings are therefore recommended if increased efficiency and stability can motivate a modest reduction in accuracy. The $\Delta x3$ grid reduces simulation cost significantly, and still maintains a predictive accuracy suitable for industrial simulations. Furthermore, the accuracy was significantly impaired on the coarsest grid ($\Delta x4$), which cannot be recommended for analyses of the flow pattern within the hydraulic jump.

Chapter 6

Discussion

This chapter provides a discussion of the scientific contributions of this work. Initially, the main results are highlighted, before the different modelling methods, and research strategies are discussed in terms of strengths and limitations. Finally, perspectives on future research are given.

6.1 Main findings and contributions to the state of the art

The solver `spillwayFlow`, developed as a highly economical approach combining interface capturing with additional modelling of air entrainment, was shown to perform with acceptable accuracy for four different step Froude number spillway flows. The model was developed based on prior advances within the field, and a major part of the work was devoted to thorough testing of the air entrainment model by Lopes et al. [39]. The latter revealed that the effects of this solver were significantly reduced upon grid refinement, which motivated the new developments. The advances upon prior art within the work on the stepped spillway – testing of `airInterFoam` and the development of `spillwayFlow` – can be listed as follows:

- Development of an improved air entrainment model for spillways. The model is proven to work well on four different stepped spillway flows within the skimming flow regime.
- Thoroughly testing of the predictive capabilities of a published air entrainment model on a broad range of stepped spillway flows.

These advances are useful in terms of obtaining correct water level predictions for aerated spillway flow, which is of importance both in structure design and to ensure its safe operation. Additionally, since air in the water can reduce damages caused by cavitation (as mentioned in Section 2.2), its accurate prediction can be of importance as a mean of identifying possible reductions in the need for other protective measures. Also, the reported advances can be useful in further developments within the field and can be tested and adjusted for similar applications involving interfacial air entrainment.

The LES on the dense computational grid was proven to reproduce the complicated aerated flow system within a classical hydraulic jump in agreement to corresponding DNS results reported in the literature. Furthermore, the modelling procedure was proven to perform reasonably well at coarser grids, suitable for industrial LES. The advances upon prior art can be listed as follows:

- Provides, to the best of the authors' knowledge, the first scale-resolving analysis reported on a hydraulic jump performed within the framework of OpenFOAM®.
- Provides quantifications on the differences between an algebraic and a geometric routine for interface capturing for the particular flow, in terms of:
  - Computing time
  - Accuracy
  - Stability
- Provides guidelines for the prediction of this flow by a systematic simulation campaign exploring the influence of different modelling parameters.

As a commonly used energy dissipator in hydraulic engineering, the correct prediction of the flow structure of the hydraulic jump is of importance to the hydraulic engineer. Since the results herein are produced by numerics comparable to yielding solvers in the engineering community, the results of this work might have the potential to facilitate the use of LES in industrial settings.

The comparison of the geometric and algebraic method for interface capturing can yield as background information for which scheme to choose for different purposes and accuracy demands. Since the isoAdvector interface capturing scheme (`interIsoFoam`) constitutes a relatively new supplement to the VoF solvers in OpenFOAM®, its comparison to known solvers might accelerate its use, and contribute in defining its applications. On the other hand, the reported stability problems can motivate future research efforts to resolve these issues.

Studies of influences of modelling parameters across the different scientific papers demonstrated how different settings might drastically influence the numerical result. This doesn't constitute advancement to prior art, but complements earlier statements, and constitutes a reminder of the importance of conducting proper numerical analyses, and choosing the proper settings for a particular problem.

6.2 The applied methods: strengths and limitations

As stated in Section 1.3, this thesis aims to contribute to the development of numerical prediction of air entrainment in free-surface flows. The premise was to do this within the framework of OpenFOAM®, more specific using the VoF solver `interFoam` as the starting point. This was approached using two different methods for turbulence treatment, RANS and LES.

This section provides a discussion about the different approaches used in this work. The methods are discussed in terms of strengths and limitations, and also in light of alternative choices used for prediction of similar problems.

Combining VoF with explicit modelling of air entrainment – stepped spillway

The approach employed for the stepped spillway predictions was to combine VoF with additional modelling of air entrainment within a RANS framework. As given in Section 1.2, several efforts using similar frameworks on predictions of aerated flow are reported in the literature, varying in the general multiphase framework applied. Some of the works were trying to couple interface capturing techniques into a two-fluid framework, and another branch constitutes efforts to couple an explicit aeration model to the advection equation within the VoF framework. In this work, an early premise was to follow the latter path. In retrospect, it can be questioned whether it could have been a better approach to start a bit wider, considering and testing out different paths, and then go further with the most promising.

Nevertheless, a strength of the chosen methodology is its simple formulation and high efficiency. The method also conserves the ability to capture a sharp interface in non-aerated regions, which might be a challenge using a two-fluid framework. On the negative side, the proposed method does not account for processes like bubble breakup and coalescence in the momentum equation.

A challenge with the modelling of air entrainment in a RANS framework is connected to its dependence on the turbulence, which modelling is challenging for aerated flows. Keeping the latter in mind, it is likely that the progress in modelling developments within aerated flows, depends on the development of turbulence models suited for this purpose.

The use of LES for simulations for the spillway was not considered. To the author's knowledge, no high-quality LES have been reported on spillway flows. However, it would be interesting to investigate the capability of LES to reproduce this aerated flow. Here, the air entrainment belongs to interfacial aeration, which differs in nature from the local aeration mechanism encountered the hydraulic jump.

LES – classical hydraulic jump

For the prediction of the hydraulic jump, a high-fidelity LES approach was chosen. Other possible choices for this analysis would be to use a RANS approach, with or without the addition of an additional air entrainment model.

By computing the hydraulic jump using a scale-resolving approach, the transient motion of the surface structures and the fate of the entrained bubbles can be captured. Even if RANS simulations on hydraulic jumps using `interFoam` have shown the ability to predict this flow using the realisable k-ϵ-model, an advantage using a scale-resolving approach is the avoidance of the uncertainty related to time averaging and scale separation. The latter issues arising from the interaction between turbulent eddies and topological changes of multiphase structures. Regarding this, a possibility for the hydraulic jump simulations could have been to coarsen the grid to the point where a steady surface would be predicted, and then use an additional air entrainment model to capture air entrainment. Nevertheless, efforts in this direction within the current work led to inaccurate prediction of both the free surface position and the turbulent field. The conclusion from these efforts was that at the grid resolution needed to provide a relatively accurate prediction of the average free-surface location, the amount of entrained air was not underestimated in the `interFoam` simulations. Then a need for additional air entrainment modelling was not identified for this flow.

A drawback using scale resolving methods is the time consumption and resource demand, which reduces its availability for high Reynolds number flow and in industrial settings. Nevertheless, the approach within this work was to investigate the predictive accuracy of the solvers when applied to coarser grids, not technically suitable for an LES, but commonly seen in industrial LES. At coarser grids, the computations are less resource- and time demanding, but of course, to a cost in the predictive accuracy.

In the LES, it was chosen not to model the subgrid stresses, which is in accordance with previous research on similar problems [20]. A challenge with turbulence modelling for aerated flows arises from its interaction with the unresolved multiphase structures, which is not considered in the commonly used turbulence models developed for single-phase. Therefore, omitting the modelling of these small scale structures might be an appropriate choice. Another reason for choosing this approach emerges from the fact that the study aims to investigate the predictive accuracy of LES at grids too coarse to be technically suited for LES. In this setting, the use of SGS models, intended to model a range of the turbulent spectre is considered not very accurate.

Single-phase RANS simulations

A part of the work included in this thesis constitutes single-phase RANS simulations performed on different settling basins. The work aimed to provide examples of cases where the result was heavily dependent on the modelling parameters. A more appropriate choice within the scope of this thesis would have been to perform these simulations on cases more relevant for the main theme of the thesis, which is prediction of aerated flows. Still, the chosen cases provided valuable examples on significant dependence of modelling parameters.

6.3 Future perspectives

Explicit air entrainment modelling

In the developed model, an air flux term is added at the free surface. The magnitude of this air flux term, as well as its activation, depends on the turbulence in the flow. As stated above, turbulence prediction in an aerated case is not trivial as it depends on the interaction between bubbles, surface structures and the turbulent eddies, and would constitute a reasonable topic in future research efforts. Work in this direction has been reported elsewhere [9, 30].

In our developed model, transport of air away from the surface was identified as an issue. Within this work, the issue was addressed by adding a diffusion term for this purpose. This improved the predictive accuracy of the model, but the provided solution might be viewed as a little ad-hoc. Based on this, an issue for further research would be to look into the air transport underneath the surface region.

Predicition of aerated flows by LES

In this work, a classical hydraulic jump with inflow Froude number 2 was simulated by LES. A reasonable next step could be to perform similar simulations at hydraulic jumps with higher Froude numbers, utilising the experiences gained within the current work.

Also, interesting perspectives for further research could be to do LES on other aerated flows of importance to engineering applications. The vertical plunging jet might be one such example. This flow has been widely studied both experimentally and numerically but, to the author's knowledge, no high-quality LES analysis of the flow has been reported in the literature. However, the air entrainment process appearing in the hydraulic jump and the plunging jet both belongs to the local aeration mechanisms, and it would be even more interesting to investigate the potential of LESs on stepped spillways or other interfacial aeration flows.

Chapter 7

Conclusion

The overall aim for this PhD-work was to develop a methodology for calculating air entrainment applicable for hydraulic engineering applications and thereby provide a tool for the hydraulic industry. Accordingly, this work provides methods to predict two different aerated flows which both play significant roles within hydraulic engineering. Besides this, considerable efforts were devoted to quantitative and qualitative testing of the influence of various modelling parameters.

More specifically, a numerical solver was developed and employed for aeration of stepped spillway flows. Here a highly economical approach, combining interface capturing with additional modelling of air entrainment, was developed and validated for four different step Froude number flows. The model was integrated into the framework of `interFoam`, and proven to perform in acceptable accordance to experimental data for the tested scenarios, and constitutes improvements upon prior art.

Furthermore, LES performed on a classical hydraulic jump proved the predictive capabilities of OpenFOAM®'s VoF solvers `interFoam` and `interIsoFoam` to reproduce the complicated flow pattern within this flow in excellent agreement to corresponding DNS predictions. Also, the predictive accuracy, of these algebraic and geometric interface capturing alternatives, was tested at coarser grids and employing cheaper numerical methods, providing experience on the modelling of such flows using an LES approach. A remarkable observation from the testing regime was that the most accurate prediction of several of the important quantities was obtained at high degrees of upwinding for the interpolation of the convective term in the momentum equation. Furthermore, geometric interface capturing was found to have favourable accuracy compared to its algebraic counterpart, but at the cost of stability and computational demand.

The importance of considering the influences of modelling parameters was highlighted throughout the work. In particular, within the analyses on the hydraulic jump, the predictive accuracy of the solvers was analysed as the numerical schemes and methods were changed systematically. A different approach was employed within Paper I, which presents two cases where the predicted flow path changes substantially based on the modelling parameters. Results from these studies constitute a reminder of the importance of conducting proper numerical analyses and choosing suitable parameter settings for a particular problem.

As a premise for the current PhD-work, all computations and implementations were performed within the framework of OpenFOAM®. Furthermore, both the developed model, the simulations cases, and the results files are made publicly available. In this way, the developments will be accessible both for the research community and the industry in the future.

Bibliography

[1] B. Andersson, R. Andersson, L. Hakansson, M. Mortensen, R. Sudiyo, and B. van Wachem. *Computational Fluid Dynamics for Engineers*. Cambridge University Press, 2011. doi: 10.1017/cbo9781139093590. URL `https://doi.org/10.1017/cbo9781139093590`.

[2] A. Bayon-Barrachina and P. A. Lopez-Jimenez. Numerical analysis of hydraulic jumps using OpenFOAM. *Journal of Hydroinformatics*, 17(4): 662–678, 2015. ISSN 1464-7141. doi: 10.2166/hydro.2015.041. URL `https://doi.org/10.2166/hydro.2015.041`.

[3] Bekkeinntakkommiteen. Bekkeinntak på kraftverkstunneler. Technical report, 1986. Sluttrapport fra Bekkeinntakkommiteen.

[4] B. Blocken and C. Gualtieri. Ten iterative steps for model development and evaluation applied to computational fluid dynamics for environmental fluid mechanics. *Environmental Modelling & Software*, 33:1–22, July 2012. doi: 10.1016/j.envsoft.2012.02.001. URL `https://doi.org/10.1016/j.envsoft.2012.02.001`.

[5] R. M. Boes and W. H. Hager. Two-phase flow characteristics of stepped spillways. *Journal of Hydraulic Engineering*, 129(9):661–670, Sept. 2003. doi: 10.1061/(asce)0733-9429(2003)129:9(661). URL `https://doi.org/10.1061/(asce)0733-9429(2003)129:9(661)`.

[6] R. M. Boes and W. H. Hager. Hydraulic design of stepped spillways. *Journal of Hydraulic Engineering*, 129(9):671–679, Sept. 2003. doi: 10.1061/(asce)0733-9429(2003)129:9(671). URL `https://doi.org/10.1061/(asce)0733-9429(2003)129:9(671)`.

[7] J. Boussinesq. *Essai sur la theorie des eaux courantes*. Paris: Imprimerie Nationale, 1877.

[8] J. Brackbill, D. Kothe, and C. Zemach. A continuum method for modeling surface tension. *Journal of Computational Physics*, 100 (2):335 – 354, 1992. ISSN 0021-9991. doi: http://dx.doi.org/10.1016/0021-9991(92)90240-Y. URL `http://www.sciencedirect.com/science/article/pii/002199919290240Y`.

[9] M. Brocchini and D. H. Peregrine. The dynamics of strong turbulence at free surfaces. part 1. description. *Journal of Fluid Mechanics*, 449:225–254, Dec. 2001. doi: 10.1017/s0022112001006012. URL `https://doi.org/10.1017/s0022112001006012`.

[10] D. B. Bung. Developing flow in skimming flow regime on embankment stepped spillways. *Journal of Hydraulic Research*, 49(5):639–648, sep 2011. doi: 10.1080/00221686.2011.584372. URL `https://doi.org/10.1080/00221686.2011.584372`.

[11] J. C. Cano-Lozano, R. Bolaños-Jiménez, C. Gutiérrez-Montes, and C. Martínez-Bazán. The use of Volume of Fluid technique to analyze multiphase flows: Specific case of bubble rising in still liquids. *Applied Mathematical Modelling*, 39(12):3290–3305, 2015. ISSN 0307904X. doi: 10.1016/j.apm.2014.11.034. URL `https://doi.org/10.1016/j.apm.2014.11.034`.

[12] G. Cerne, S. Petelin, and I. Tiselj. Coupling of the interface tracking and the two-fluid models for the simulation of incompressible two-phase flow. *Journal of computational physics*, 171(2):776–804, 2001.

[13] H. Chanson. Stepped spillway flows and air entrainment. *Canadian Journal of Civil Engineering*, 20(3):422–435, June 1993. ISSN 0315-1468, 1208-6029. doi: 10.1139/l93-057. URL `http://www.nrcresearchpress.com/doi/10.1139/l93-057`.

[14] H. Chanson. *Environmental hydraulics of open channel flows*. Elsevier Butterworth Heinemann, Amsterdam Boston, 2004. ISBN 9780750661652.

[15] H. Chanson. Hydraulics of aerated flows: qui pro quo? *Journal of Hydraulic Research*, 51(3):223–243, 2013. doi: 10.1080/00221686.2013.795917. URL `http://dx.doi.org/10.1080/00221686.2013.795917`.

[16] H. Chanson and C. Gualtieri. Similitude and scale effects of air entrainment in hydraulic jumps. *Journal of Hydraulic Research*, 46(1):35–44, jan

2008. doi: 10.1080/00221686.2008.9521841. URL `https://doi.org/10.1080/00221686.2008.9521841`.

[17] H. Chanson, S. Aoki, and A. Hoque. Physical modelling and similitude of air bubble entrainment at vertical circular plunging jets. *Chemical Engineering Science*, 59(4):747 – 758, 2004. ISSN 0009-2509. doi: http://dx.doi.org/10.1016/j.ces.2003.11.016. URL `http://www.sciencedirect.com/science/article/pii/S0009250903005669`.

[18] C. D. Chosie and J. G. Vasconcelos. Kinematics of entrapped air pockets in stormwater storage tunnels. In *World Environmental and Water Resources Congress 2013*. American Society of Civil Engineers, May 2013. doi: 10.1061/9780784412947.161. URL `https://doi.org/10.1061/9780784412947.161`.

[19] S. S. Deshpande, M. F. Trujillo, X. Wu, and G. Chahine. Computational and experimental characterization of a liquid jet plunging into a quiescent pool at shallow inclination. *International Journal of Heat and Fluid Flow*, 34: 1–14, Apr. 2012. doi: 10.1016/j.ijheatfluidflow.2012.01.011. URL `https://doi.org/10.1016/j.ijheatfluidflow.2012.01.011`.

[20] S. S. Deshpande, M. F. Trujillo, X. Wu, and G. Chahine. Computational and experimental characterization of a liquid jet plunging into a quiescent pool at shallow inclination. *International Journal of Heat and Fluid Flow*, 34:1 – 14, 2012. ISSN 0142-727X. doi: http://dx.doi.org/10.1016/j.ijheatfluidflow.2012.01.011. URL `http://www.sciencedirect.com/science/article/pii/S0142727X12000197`.

[21] Dong, Wang, Vetsch, Boes, and Tan. Numerical simulation of air–water two-phase flow on stepped spillways behind x-shaped flaring gate piers under very high unit discharge. *Water*, 11(10):1956, Sept. 2019. doi: 10.3390/w11101956. URL `https://doi.org/10.3390/w11101956`.

[22] D. Ervine and H. Falvey. Behaviour of turbulent water jets in the atmosphere and in plunge pools. *Proceedings of the Institution of Civil Engineers*, 83(1): 295–314, Mar. 1987. doi: 10.1680/iicep.1987.353. URL `https://doi.org/10.1680/iicep.1987.353`.

[23] H. T. Falvey and J. H. Weldon. Case study: Dillon dam trashrack damage. *Journal of Hydraulic Engineering*, 128(2):144–150, Feb. 2002. doi: 10.1061/(asce)0733-9429(2002)128:2(144). URL `https://doi.org/10.1061/(asce)0733-9429(2002)128:2(144)`.

[24] W. Fan and H. Anglart. varRhoTurbVOF: A new set of volume of fluid solvers for turbulent isothermal multiphase flows in OpenFOAM. *Computer Physics Communications*, 247:106876, Feb. 2020. doi: 10.1016/j.cpc.2019.106876. URL `https://doi.org/10.1016/j.cpc.2019.106876`.

[25] K. Frizell and B. Mefford. Designing spillways to prevent cavitation damage. 1991.

[26] F. F. Grinstein, L. G. Margolin, and W. Rider, editors. *Implicit large eddy simulation: computing turbulent fluid dynamics*. Cambridge University Press, Cambridge ; New York, 2007. ISBN 9780521869829. OCLC: ocm71778963.

[27] S. Hänsch, D. Lucas, T. Höhne, and E. Krepper. Application of a new concept for multi-scale interfacial structures to the dam-break case with an obstacle. *Nuclear Engineering and Design*, 279:171–181, Nov. 2014. doi: 10.1016/j.nucengdes.2014.02.006. URL `https://doi.org/10.1016/j.nucengdes.2014.02.006`.

[28] C. Hirt. Modeling turbulent entrainment of air at a free surface. *Flow Science, Inc*, 2003.

[29] C. Hirt and B. Nichols. Volume of fluid (vof) method for the dynamics of free boundaries. *Journal of Computational Physics*, 39(1):201 – 225, 1981. ISSN 0021-9991. doi: http://dx.doi.org/10.1016/0021-9991(81)90145-5. URL `http://www.sciencedirect.com/science/article/pii/0021999181901455`.

[30] T. Höhne and S. Hänsch. A droplet entrainment model for horizontal segregated flows. *Nuclear Engineering and Design*, 286:18–26, May 2015. doi: 10.1016/j.nucengdes.2015.01.013. URL `https://doi.org/10.1016/j.nucengdes.2015.01.013`.

[31] V. Jesudhas, R. Balachandar, V. Roussinova, and R. Barron. Turbulence characteristics of classical hydraulic jump using DES. *Journal of Hydraulic Engineering*, 144(6):04018022, 2018. ISSN 0733-9429. doi: https://ascelibrary.org/doi/10.1061/(asce)hy.1943-7900.0001427. URL `10.1061/(asce)hy.1943-7900.0001427`.

[32] J. A. Kells and C. D. Smith. Reduction of cavitation on spillways by induced air entrainment. *Canadian Journal of Civil Engineering*, 18(3):358–377, June 1991. doi: 10.1139/l91-047. URL `https://doi.org/10.1139/l91-047`.

[33] L. Khezzar, N. Kharoua, and K. T. Kiger. Large eddy simulation of rough and smooth liquid plunging jet processes. *Progress in Nuclear Energy*, 85: 140–155, Nov. 2015. doi: 10.1016/j.pnucene.2015.06.011. URL `https://doi.org/10.1016/j.pnucene.2015.06.011`.

[34] H. Kobus. Local air entrainment and detrainment. *Symposium on Scale Effects in Modelling Hydraulic Structures*, 1984. URL `http://dx.doi.org/10.18419/opus-559`.

[35] E. Krepper, D. Lucas, T. Frank, H.-M. Prasser, and P. J. Zwart. The inhomogeneous MUSIG model for the simulation of polydispersed flows. *Nuclear Engineering and Design*, 238(7):1690–1702, July 2008. doi: 10.1016/j.nucengdes.2008.01.004. URL `https://doi.org/10.1016/j.nucengdes.2008.01.004`.

[36] B. Launder and B. Sharma. Application of the energy-dissipation model of turbulence to the calculation of flow near a spinning disc. *Letters in Heat and Mass Transfer*, 1(2):131–137, Nov. 1974. doi: 10.1016/0094-4548(74)90150-7. URL `https://doi.org/10.1016/0094-4548(74)90150-7`.

[37] L. Lia and G. Krszus. Luftlommer i vanntunneler. Technical report, 2004.

[38] P. Lopes, J. Leandro, R. F. Carvalho, and D. B. Bung. Alternating skimming flow over a stepped spillway. *Environmental Fluid Mechanics*, 17(2):303–322, Oct. 2016. doi: 10.1007/s10652-016-9484-x. URL `https://doi.org/10.1007/s10652-016-9484-x`.

[39] P. Lopes, J. Leandro, and R. F. Carvalho. Self-aeration modelling using a sub-grid volume-of-fluid model. *International Journal of Nonlinear Sciences and Numerical Simulation*, 18(7-8), dec 2017. doi: 10.1515/ijnsns-2017-0015. URL `https://doi.org/10.1515/ijnsns-2017-0015`.

[40] P. Lubin, S. Vincent, S. Abadie, and J.-P. Caltagirone. Three-dimensional large eddy simulation of air entrainment under plunging breaking waves. *Coastal Engineering*, 53(8):631–655, June 2006. doi: 10.1016/j.coastaleng.2006.01.001. URL `https://doi.org/10.1016/j.coastaleng.2006.01.001`.

[41] J. Ma, A. A. Oberai, D. A. Drew, R. T. Lahey, and M. C. Hyman. A comprehensive sub-grid air entrainment model for rans modeling of free-surface bubbly flows. *The Journal of Computational Multiphase Flows*, 3(1):41–56, 2011.

[42] J. Ma, A. A. Oberai, D. A. Drew, R. T. Lahey, and M. C. Hyman. A comprehensive sub-grid air entrainment model for rans modeling of free-surface bubbly flows. *The Journal of Computational Multiphase Flows*, 3(1):41–56, 2011.

[43] M. Mortazavi, V. L. Chenadec, P. Moin, and A. Mani. Direct numerical simulation of a turbulent hydraulic jump: turbulence statistics and air entrainment. *Journal of Fluid Mechanics*, 797:60–94, May 2016. doi: 10.1017/jfm.2016.230. URL `https://doi.org/10.1017/jfm.2016.230`.

[44] F. Murzyn, D. Mouaze, and J. Chaplin. Optical fibre probe measurements of bubbly flow in hydraulic jumps. *International Journal of Multiphase Flow*, 31(1):141–154, jan 2005. doi: 10.1016/j.ijmultiphaseflow.2004.09.004. URL `https://doi.org/10.1016/j.ijmultiphaseflow.2004.09.004`.

[45] F. Nicoud and F. Ducros. *Flow, Turbulence and Combustion*, 62(3):183–200, 1999. doi: 10.1023/a:1009995426001. URL `https://doi.org/10.1023/a:1009995426001`.

[46] A. B. of Shipping. Air lubrication technology. Technical report, 2019.

[47] M. Pfister and W. H. Hager. Self-entrainment of air on stepped spillways. *International Journal of Multiphase Flow*, 37(2):99–107, Mar. 2011. doi: 10.1016/j.ijmultiphaseflow.2010.10.007. URL `https://doi.org/10.1016/j.ijmultiphaseflow.2010.10.007`.

[48] O. Pozos-Estrada, I. Pothof, O. A. Fuentes-Mariles, R. Dominguez-Mora, A. Pedrozo-Acuña, R. Meli, and F. Peña. Failure of a drainage tunnel caused by an entrapped air pocket. *Urban Water Journal*, 12(6):446–454, June 2015. doi: 10.1080/1573062x.2015.1041990. URL `https://doi.org/10.1080/1573062x.2015.1041990`.

[49] Z. Qian, X. Hu, W. Huai, and A. Amador. Numerical simulation and analysis of water flow over stepped spillways. *Science in China Series E: Technological Sciences*, 52(7):1958–1965, June 2009. doi: 10.1007/s11431-009-0127-z. URL `https://doi.org/10.1007/s11431-009-0127-z`.

[50] X. Qu, L. Khezzar, D. Danciu, M. Labois, and D. Lakehal. Characterization of plunging liquid jets: A combined experimental and numerical investigation. *International Journal of Multiphase Flow*, 37(7):722 – 731, 2011. ISSN 0301-9322. doi: http://dx.doi.org/10.1016/j.ijmultiphaseflow.2011.02.006. URL `http://www.sciencedirect.com/science/article/pii/S0301932211000516`.

[51] O. Reynolds. IV. On the dynamical theory of incompressible viscous fluids and the determination of the criterion. *Philosophical Transactions of the Royal Society of London. (A.)*, 186:123–164, Dec. 1895. doi: 10.1098/rsta.1895.0004. URL https://doi.org/10.1098/rsta.1895.0004.

[52] S.-R. Sabbagh-Yazdi and H. Rezaei-Manizani. Multi-layer computation of coupled finite volume solution of depth- averaged flow in steep chute spillways considering air concentration effects. 2008.

[53] K. Sene. Air entrainment by plunging jets. *Chemical Engineering Science*, 43(10):2615 – 2623, 1988. ISSN 0009-2509. doi: http://dx.doi.org/10.1016/0009-2509(88)80005-8. URL http://www.sciencedirect.com/science/article/pii/0009250988800058.

[54] O. Y. Shonibare and K. E. Wardle. Numerical investigation of vertical plunging jet using a hybrid multifluid–VOF multiphase CFD solver. *International Journal of Chemical Engineering*, 2015:1–14, 2015. doi: 10.1155/2015/925639. URL https://doi.org/10.1155/2015/925639.

[55] J. Smagorinsky. General circulation experiments with the primitive equations. *Monthly Weather Review*, 91(3):99–164, Mar. 1963. doi: 10.1175/1520-0493(1963)091<0099:gcewtp>2.3.co;2. URL https://doi.org/10.1175/1520-0493(1963)091<0099:gcewtp>2.3.co;2.

[56] L. G. Straub and A. G. Anderson. Experiments on self-aerated flow in open channels. *J.Hydraul.Div.*, 84(7):1–35, 1958. URL www.scopus.com.

[57] L. Strubelj and I. Tiselj. Two-fluid model with interface sharpening. *International Journal for Numerical Methods in Engineering*, 85(5):575–590, 2011. ISSN 1097-0207. doi: 10.1002/nme.2978. URL http://dx.doi.org/10.1002/nme.2978.

[58] M. Takahashi, C. Gonzalez, and H. Chanson. Self-aeration and turbulence in a stepped channel: Influence of cavity surface roughness. *International Journal of Multiphase Flow*, 32(12):1370–1385, Dec. 2006. doi: 10.1016/j.ijmultiphaseflow.2006.07.001. URL https://doi.org/10.1016/j.ijmultiphaseflow.2006.07.001.

[59] D. Valero and D. Bung. Hybrid investigation of air transport processes in moderately sloped stepped spillway flows. In *E-proceedings of the 36th IAHR World Congress 28 June - 3 July, 2015, The Hague, the Netherlands*, pages 1 – 10, 2015.

[60] D. Valero, N. Viti, and C. Gualtieri. Numerical simulation of hydraulic jumps. Part 1: Experimental data for modelling performance assessment. *Water*, 11(1):1–16, 2018. doi: 10.3390/w11010036. URL `https://doi.org/10.3390/w11010036`.

[61] J. G. Vasconcelos and S. J. Wright. Geysering generated by large air pockets released through water-filled ventilation shafts. *Journal of Hydraulic Engineering*, 137(5):543–555, May 2011. doi: 10.1061/(asce)hy.1943-7900.0000332. URL `https://doi.org/10.1061/(asce)hy.1943-7900.0000332`.

[62] N. Viti, D. Valero, and C. Gualtieri. Numerical simulation of hydraulic jumps. Part 2: Recent results and future outlook. *Water*, 11(1):1–18, 2018. doi: 10.3390/w11010028. URL `https://doi.org/10.3390/w11010028`.

[63] K. E. Wardle and H. G. Weller. Hybrid multiphase cfd solver for coupled dispersed/segregated flows in liquid-liquid extraction. *International Journal of Chemical Engineering*, 2013, 2013.

[64] D. C. Wilcox. Reassessment of the scale-determining equation for advanced turbulence models. *AIAA Journal*, 26(11):1299–1310, Nov. 1988. doi: 10.2514/3.10041. URL `https://doi.org/10.2514/3.10041`.

[65] A. Witt, J. Gulliver, and L. Shen. Simulating air entrainment and vortex dynamics in a hydraulic jump. *International Journal of Multiphase Flow*, 72:165 – 180, 2015. ISSN 0301-9322. doi: https://doi.org/10.1016/j.ijmultiphaseflow.2015.02.012. URL `http://www.sciencedirect.com/science/article/pii/S0301932215000336`.

[66] S. T. Zalesak. Fully multidimensional flux-corrected transport algorithms for fluids. *Journal of Computational Physics*, 31(3):335–362, 1979. ISSN 10902716. doi: 10.1016/0021-9991(79)90051-2.

[67] J. Zhan, J. Zhang, and Y. Gong. Numerical investigation of air-entrainment in skimming flow over stepped spillways. *Theoretical and Applied Mechanics Letters*, 6(3):139–142, May 2016. doi: 10.1016/j.taml.2016.03.003. URL `https://doi.org/10.1016/j.taml.2016.03.003`.

[68] F. Zhou, F. E. Hicks, and P. M. Steffler. Transient flow in a rapidly filling horizontal pipe containing trapped air. *Journal of Hydraulic Engineering*, 128(6):625–634, June 2002. doi: 10.1061/(asce)0733-9429(2002)128:6(625). URL `https://doi.org/10.1061/(asce)0733-9429(2002)128:6(625)`.

Appendix A

Scientific papers

A.1 Paper I: Multiple solutions of Navier-Stokes equations computing water flow in sand traps

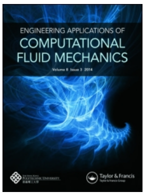

Taylor & Francis
Taylor & Francis Group

Engineering Applications of Computational Fluid Mechanics

ISSN: 1994-2060 (Print) 1997-003X (Online) Journal homepage: https://www.tandfonline.com/loi/tcfm20

Multiple solutions of the Navier-Stokes equations computing water flow in sand traps

Silje K. Almeland, Nils R. B. Olsen, Kari Bråveit & Pravin R. Aryal

To cite this article: Silje K. Almeland, Nils R. B. Olsen, Kari Bråveit & Pravin R. Aryal (2019) Multiple solutions of the Navier-Stokes equations computing water flow in sand traps, Engineering Applications of Computational Fluid Mechanics, 13:1, 199-219, DOI: 10.1080/19942060.2019.1566094

To link to this article: https://doi.org/10.1080/19942060.2019.1566094

ENGINEERING APPLICATIONS OF COMPUTATIONAL FLUID MECHANICS
2019, VOL. 13, NO. 1, 199–219
https://doi.org/10.1080/19942060.2019.1566094

Taylor & Francis
Taylor & Francis Group

Multiple solutions of the Navier-Stokes equations computing water flow in sand traps

Silje K. Almeland[a], Nils R. B. Olsen[a], Kari Bråveit[b] and Pravin R. Aryal[c]

[a]Department of Civil and Environmental Engineering, Norwegian University of Science and Technology, Trondheim, Norway; [b]Norwegian Water Resources and Energy Directorate, Trondheim, Norway; [c]Ministry of Energy, Water Resources and Irrigation, Kathmandu, Nepal

ABSTRACT

Two cases are presented wherein the main flow pattern in sand traps changes considerably as a function of discretization scheme, grid resolution and turbulence model. Both cases involve channel flows directed into a desilting basin, where the main current changes from one part of the geometry to the other. The CFD computations are validated with field or laboratory measurements. The first case presented is one of the sand traps of Khimti hydro power plant in Nepal. According to the laboratory measurements, the recirculation zone for this case is close to the bed, with the main current following the water surface. This is reproduced by the numerical model when using a first-order upwind scheme. Using a second-order upwind scheme, the main current is close to the bed, and the recirculation is formed at the surface. The second case is one of the sand traps of Tonstad hydro power plant in Norway. CFD computations predict the main flow field to follow the right or the left sides or the centre of the expansion region, depending on the discretization scheme, grid resolution and turbulence model. Field measurements show that the main current follows the centre of the expansion zone.

ARTICLE HISTORY
Received 7 May 2018
Accepted 4 January 2019

KEYWORDS
Khimti hydro power plant; multiple solutions; numerical modeling; Sand trap; CFD; Tonstad hydro power plant

1. Introduction

Since its early emergence in the field of aerodynamics (Hess & Smith, 1967), computational fluid dynamics (CFD) is currently employed to predict fluid flow characteristics in a diverse range of engineering applications. Real-life case studies using CFD have recently been performed in combustion engineering (Akbarian et al., 2018), thermal engineering (Ramezanizadeh, Nazari, Ahmadi, & wing, 2018) and also within numerous applications of water engineering. Numerical models to predict the amount of pollutants in rivers were developed by Chau and Jiang (2002, 2004) and used for the analyses of the Pearl River Estuary. In hydraulic engineering, CFD is considered an effective technique for computation of water and sediment flow in sand traps or desilting basins. The physical modeling alternative can be problematic with regards to the induced scale effects, particularly for scaling down the sediment particle size from prototype to model scale. The numerical model then has to compute both the flow pattern and the concentration of the sediments. This has been carried out successfully both for suspended particle movements (Olsen & Skoglund, 1994; Ruether, Singh, Olsen, & Atkinson, 2005) and for computation of bed elevation changes (Esmaeili et al., 2017; Ruether & Olsen, 2006; Török, Baranya, & Rüther, 2017). Furthermore, Olsen and Kjellesvig (1999) computed bed elevation changes in a sand trap with satisfactory results. Even if successful CFD calculations have been achieved for sand traps, the geometry of the sand trap has an expansion zone that introduces a complex flow pattern which is challenging to reproduce numerically. This article presents two case studies where multiple flow fields are identified for the flow field downstream the expansion zone.

The solution of the Navier-Stokes equations depends on several input parameters such as the overall geometry of the settling basin, its wall roughness, the discharge, to name a few. A number of solution algorithms are also available for the different terms in the Navier-Stokes equations. Diverse range of turbulence models exist, and it is possible to choose among several discretization schemes for the convective and transient terms. Furthermore, disparate variants of grid and cell configurations are available.

The grid resolution or cell density is often an important parameter in deciding the accuracy of the computed flow gradients. It is commonly acknowledged that variations in the numerical algorithms can give

CONTACT Silje K. Almeland silje.k.almeland@ntnu.no

different accuracy of the results, meaning small variations in the solution appear. This article focuses on some rare instances where the main flow pattern of the solution changes significantly as a function of the choice of numerical algorithm. Such cases have also been observed in other fields of fluid mechanics. Durrani, Cook, and McGuirk (2015) computed thermally buoyancy driven flow in a ventilation system, where a box was filled with fluid and a thermal element was placed in the bottom of the box. Perforations in the box were opened/closed to model inflow and outflow of fluid. Three different steady-state flow fields were obtained, all of them were observed in experimental results. Kamenetskiy et al. (2014) computed flow over a wing of an air plane during stall, wherein both the Spalart-Allmaras and the $k - \omega$ turbulence models were used. A numerical technique termed implicit residual smoothing (IRS) (Jameson & Baker, 1983) was used to find different flow solutions. The $k - \omega$ model was found more robust to generate multiple solutions than the one-equation Spalart-Allmaras model. However, two solutions were also found using the $k - \omega$ model. Xu, Lin, and Si (2014) obtained multiple solutions for the Navier-Stokes equations when solved for an unsteady, laminar, incompressible flow in a porous expanding channel, maintaining constant the wall suction Reynolds number and the expansion ratio. Robinson (1976) found that three numerical solutions exist for laminar, incompressible, steady flow in a parallel plate porous channel with uniform suction at both walls, when the wall suction Reynolds number exceeded a certain value. Up to three different solutions were found for a single suction Reynolds number as a function of varying skin friction. Also, two solutions were found by an analytical approach. This verifies that the Navier-Stokes equations can have multiple solutions irrespective of the numerical method in use. Kantoush, Bollaert, and Schleiss (2008) performed a series of numerical and laboratory experiments on sediment deposition in a rectangular basin. An objective was to test the sensitivity of different flow and sediments parameters and different turbulence closure schemes. In the physical model experiments, deposition in the basin systematically developed along the left bank, although the inflow and outflow were positioned symmetrically along the centre line of the basin. Although asymmetric patterns were encountered most frequently, symmetrical behavioral patterns were also observed from time to time. This behavior was also identified in the results from the numerical model. The simulations generally produced an asymmetric flow pattern that easily switched side according to the assumptions made for the initial- and boundary conditions. The results were similarly sensitive to the choice of turbulence model. In addition, performing three-dimensional simulations on a shallow basin, Esmaeili, Sumi, Kantoush, Haun, and Rüther (2016) found the symmetric behavior of the flow field to be sensitive to small disturbances in the boundary conditions. Viroulet et al. (2017) observed two different steady-state regimes for granular flow over a smooth two-dimensional bump in a small scale physical modeling study. Dependent on the initial number of particles placed in front of the bump, either the formation of a detached jet downstream or a shock upstream the bump was identified.

In the present study, multiple solutions were found for the flow field of desilting basins in two different hydro power plants. The numerical solution was investigated for different grids, discretization schemes, and turbulence models.

2. Numerical models

Two different CFD programs were utilised in the present study, SSIIM 1 and OpenFOAM. The SSIIM 1 program is a freeware, while OpenFOAM is an open source program. Both programs use a finite volume method to solve the Reynolds averaged Navier-Stokes equations for steady- and incompressible fluid flow. The system of equations that was solved, is given in Equation (1)–(2):

$$\nabla \cdot \mathbf{U} = 0 \tag{1}$$

$$\nabla \cdot (\rho \mathbf{U}\mathbf{U}) = -\nabla p + \rho \mathbf{g} + \mu \nabla^2 \mathbf{U} \tag{2}$$

where $\mathbf{U}$ [m/s] is the fluid velocity, ρ [kg/m^3] the fluid density, p the pressure, $\mathbf{g}$ [m/s^2] the gravitational acceleration, and μ [kg/m s^2] is the total dynamic viscosity. The SIMPLE method (Patankar & Spalding, 1972) was used to solve the pressure field. The programs used different types of three-dimensional grids. The SSIIM 1 program used a structured non-orthogonal grid, where geometry details were modeled by blocking out cells. The OpenFOAM program used orthogonal, unstructured grids, based on hexahedral cells.

For both cases, sensitivity analyses for grid resolution and discretization scheme were performed. The turbulence was modeled by RANS. All simulations for the Khimti case used the standard $k - \epsilon$ model (Launder & Spalding, 1974) for turbulence modeling. For the Tonstad case, the standard $k - \epsilon$ model, the realizable $k - \epsilon$ model (Shih, Liou, Shabbir, Yang, & Zhu, 1995) and the RNG $k - \epsilon$ model (Yakhot, Orszag, Thangam, Gatski, & Speziale, 1992) were tested in a sensitivity analysis. Further, the near-wall behavior was modeled with wall functions. A brief description of the wall models used in these simulations is given in Section 2.1–2.2 of this article.

2.1. Discretization scheme

For both cases, the convective terms in the Navier-Stokes equations were discretized with two different numerical approaches, a first- and a second-order upwind scheme. The second-order scheme used for the Khimti case was not bounded, whilst for the Tonstad simulations, a bounded scheme was applied. Regarding the turbulence variables, the first-order upwind scheme was chosen due to its favorable stability properties.

The behavior of the flow field for the Khimti case seemed to be highly dependent on the discretization scheme in use. This is illustrated and presented in Section 3.1 of this article.

2.2. Wall function

The near-wall behavior was computed by wall functions. The near-wall region consists of three main parts, the laminar sub-layer, the buffer layer and the logarithmic layer. In the laminar sub-layer, the laminar law is valid ($u^+ = y^+$)[1], and in the logarithmic layer, the logarithmic law (3) holds,

$$u^+ = \frac{1}{\kappa}\ln\left(y^+\right) + B = \frac{1}{\kappa}\ln\left(Ey^+\right) \tag{3}$$

Here $\kappa \approx 0.4$, is the von Karman's constant and the additive constant $B \approx 5.0 - 5.4$ (Schlichting, 1979). These equations have previously been developed and validated for smooth walls. Experiments for rough surfaces (Nikuradse & Nikuradse, 1933) have indicated that the behavior of the flow field follows the same logarithmic slope as for smooth walls. Nevertheless, for a rough wall, the curve of the logarithmic line in the u^+ vs y^+ diagram is shifted in the negative u^+-direction by a magnitude of ΔB. Then the logarithmic law for a rough wall is given as in Equation (4):

$$u^+ = \frac{1}{\kappa}\ln\left(y^+\right) + B - \Delta B(k_s^+, C_s) \tag{4}$$

where ΔB is a function of the dimensionless sand-grain roughness $k_s^+ = u_t k_s/\nu_t$ and a roughness constant C_s. y^+ and u^+ used in Equation (4) and (3) represent the dimensionless distance from the wall and the dimensionless velocity, respectively. These variables are defined in Equation (5):

$$\begin{aligned} u^+ &= \frac{u}{u_\tau} \\ y^+ &= \frac{u_\tau y}{\nu} \end{aligned} \tag{5}$$

where $u_\tau = \sqrt{\frac{\tau_{wall}}{\rho}}$ is the shear velocity, u is the velocity parallel to the wall and y is the wall normal distance (Versteeg, 2007).

All simulations for the Khimti case were run with a rough wall function approach. In SSIIM the near-wall behaviour for rough walls is based on Schlichting wall law (Schlichting, 1979), given in Equation (6):

$$u^+ = \frac{1}{\kappa}\ln\left(\frac{30y}{k_s}\right) \tag{6}$$

where k_s is a roughness parameter.

For the simulations on Tonstad sand trap, a rough wall function was adopted. In OpenFOAM, the choice of wall function is specified through the turbulent viscosity ν_t. The rough wall function, implemented in an OpenFOAM case as `nutkRoughWallFunction`, utilises a roughness equation in the form of Equation (4) to account for the roughness effects (OpenFOAM the openfoam foundation, n.d.). This is equivalent to manipulating the parameter E in Equation (3).

3. The khimiti sand trap

The Khimti-I hydro power plant is located on the Khimti River in the Koshi basin of Eastern Nepal. This run-of-the river hydro power project is equipped with a sand trap, as the sediment concentrations in the Khimti river can be substantial. The sand trap is concrete lined and operates under open channel flow conditions. It has two basins, where only one (the left) was investigated in the study. The length of the sand trap is 135 m, including the inlet section. Considering the fact that the inlet section is slightly skewed compared to the direction of the sand trap, a divide wall was constructed to establish a more uniform flow profile in the transverse direction. The maximum channel width is 12 m and the maximum depth is 7.7 m. The sand trap was investigated in a physical model study at the Tribhuvan University in Nepal, where velocity profiles of water flow within the sand trap were measured by anchored floats (Hydroconsult, 1997). The construction material of the physical model was plywood supported by steel frames. Transparent acrylic glass and extruded foam were used within the transition bends at the upstream end of the model. The physical model was built at a geometric scale ratio of 1:15 and the other hydraulic parameters were scaled according to Froude's law. The discharge into the prototype sand trap was 15.05 m^3/s. The vertical profile of the water velocity was measured for different vertical lines at different locations downstream of the sand trap inlet. Flow anchors at three different water depths were used for these measurements. The floats were timed over a length of 1 m.

In the present study, the flow field of the sand trap was predicted by a numerical model, where the flowing water was treated as an incompressible fluid. The sand

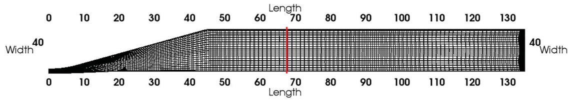

Figure 1. Plan view of Khimti sand trap. Flow direction is from left to right. The red line placed at 67.5 m, indicates the cross-section where the measurements presented in Figure 3 and 4 were performed.

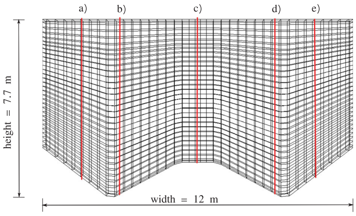

Figure 2. Cross-sectional view of Khimti sand trap at 67.5 m. The different lines correspond to the locations of the different velocity measurements. Given as distances from the left wall, the locations for the different vertical lines are, $a = 1.5$ m, $b = 3$ m, $c = 6$ m, $d = 9$ m and $e = 10.5$ m. The cross-section shown in this figure corresponds to the location of the velocity measurements presented in Figure 4.

trap was modeled in full size. The measurements from the physical model study were used to validate the results from the numerical model. A plan view of the computational domain is given in Figure 1. Vertical profiles of streamwise velocities were measured at a location 67.5 m downstream the inlet (see Figure 1). As illustrated in Figure 2, several vertical profiles were measured along this cross-section. These locations correspond to 1.5, 3, 6, 9 and 10.5 m from the upper wall in Figure 1.

The water discharge was specified at the sand trap inlet, and a zero gradient boundary condition was given for the outlet. The initial streamwise flow velocity (u_x) in the internal part of the sand trap was estimated according to the continuity equation. The remaining velocities (u_y and u_z) were initially set to zero. The near-wall behaviour was calculated by wall functions (Equation (6)). A roughness height of $k_s = 0.0017$ m was used for the concrete walls. This is similar to a Manning-Strickler value of 90 (Mayer-Peter & Mueller, 1948; Rijn, 1982), which is tabulated as a typical value for cement lined channels (Elger, Williams, Crowe, & Roberson, 2013).

3.1. Effect of discretization scheme

Longitudinal sections of the sand trap (side view), showing the velocity fields predicted by the different discretization schemes, are given in Figure 3. These figures show that the predicted flow field varied significantly depending on the discretization scheme in use. Figure 3(a) illustrates that the first-order upwind scheme predicts a jet at the water surface, and a recirculation zone towards the bed. On the other hand, the second-order upwind scheme computes the highest velocities close to the bed. Here a recirculation zone is found towards the free surface (see Figure 3(b)).

Measured and computed velocity values for the vertical lines (a), (b), and (e) in Figure 2 are compared in Figure 4. According to the measurements, the first-order upwind scheme gives a more accurate velocity profile than the second-order upwind scheme for all vertical lines (see Figure 4). The best correlation with the measurements are found for the vertical profile 3 m from the left edge of the sand trap (see Figure 4(b)). For the lines 1.5 and 9 m from the left edge of the sand trap, the correlation between the laboratory measurements and the first-order upwind simulations are not as good as for the profiles 3 m from the left edge. Nevertheless, the results from the calculations using the first-order scheme still appear to produce solutions closest to the measured values (see 4(a),4(c)).

3.2. Grid sensitivity

Three different grid configurations were used to carry out the computations. Identical boundary conditions were used for all grids, but they differed in cell density. The coarsest, middle and finest grid contained 38,000 cells, 303,000 cells and 1.2 million cells, respectively. The simulations using the different grid resolutions resulted in similar flow fields (see Figure 5). Nevertheless, the velocity measurements for the first-order upwind scheme tended to have a better correspondence with the measured data as the grid resolution was increased (see Figure 5(a)). Further grid refinement was problematic as SSIIM 1 was not parallelized with message passing interface (MPI) and therefore not able to fully utilise the advantages of high-performance computing (HPC) clusters.

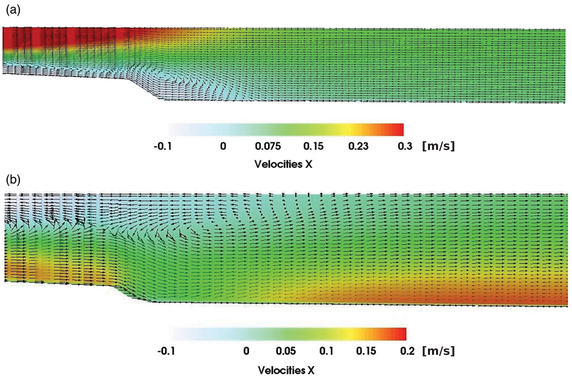

Figure 3. Longitudinal profiles with velocity vectors u_X through the Khimti Sand Trap (side view). (a) Computed with a first-order upwind scheme, here the recirculation zone is located towards the bottom of the sand trap. (b) Computed with a second-order upwind scheme, here the location of the recirculation zone is close to the surface.

3.3. *Discussion*

The fact that the first-order discretization scheme predicts a more correct velocity field than a second-order scheme is remarkable as most guidelines for CFD computations recommend the usage of a second-order scheme instead of a first-order scheme (Franke, Hellsten, Schlunzen, & Carissimo, 2011). Note that the second-order upwind scheme used in these simulations is not bounded. Therefore, it may produce unrealistic overshoots/undershoots in its extrapolation of a variable value. This provides a possible explanation for the findings in Section 3.1 of this article. Aryal and Olsen (2001) found results with similar overshooting problems for the second-order upwind scheme when doing simulation at the same sand trap.

Using the first-order upwind scheme, a recirculation zone was located close to the bed of the sand trap, whilst for the second-order upwind scheme, the recirculation zone was located close to the free surface. Regarding the sand trap efficiency, a recirculation zone close to the bottom could swirl up sediments from the bottom of the sand trap, and work against the sediment settling. This illustrates the importance of an accurate prediction of the flow pattern in the sand trap with respect to sand trap efficiency calculations. Similar observations with multiple stable flow configurations have been identified in physical model studies conducted for shallow water flows (Kantoush et al., 2008; Viroulet et al., 2017).

4. The Tonstad sand trap

The Tonstad hydro power plant is located in southwestern Norway. In terms of electricity production, it is the largest hydro power plant in Norway. Prior to being directed into the turbines for power generation, the water enters one of the three parallel sand traps. The flow within the sand traps is pressurised. The sand traps are rock blasted and unlined, resulting in large roughness elements with complex geometry. The flow in one of these sand traps was computed by Bråtveit and Olsen (2015) using the commercial program STAR-CCM+. Lateral profiles of horizontal velocities were measured in the sand trap using field Acoustic Doppler Current Profilers (ADCP) as described by Bråtveit and Olsen (2015). The numerical results obtained in connection to this study showed variability in the placement of the maximum velocity at these lines. The inlet jet tended to follow paths on different sides of the tunnel depending on the grid type and grid resolution.

The fact that multiple solutions can be produced by different grids for the numerical model is an important issue to consider when dealing with CFD. The intention of the present study was to investigate this phenomenon and to see which parameters influenced the results. From field measurements performed by Bråtveit and Olsen (2015), velocity measurements were available for a horizontal line at a cross-section just downstream the expansion zone (cf. Figure 6). The vertical position of

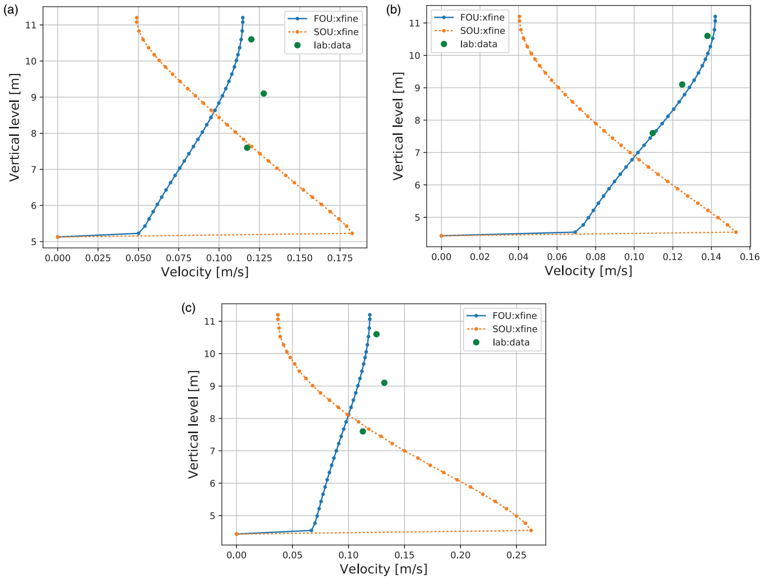

Figure 4. Computed and measured velocities in streamwise direction (u_x) for three vertical profiles in the Khimti sand trap. All velocity profiles are measured at different vertical lines 67.5 m downstream the sand trap inlet. Subfigures (a), (b) and (c) corresponds to line (a), (b) and (e) in Figure 2, respectively. The labels refer to the discretization scheme, FOU = first-order upwind scheme, SOU = second-order upwind scheme. (a) 1.5 m from horizontal edge, (b) 3 m from horizontal edge and (c) 9 m from horizontal edge.

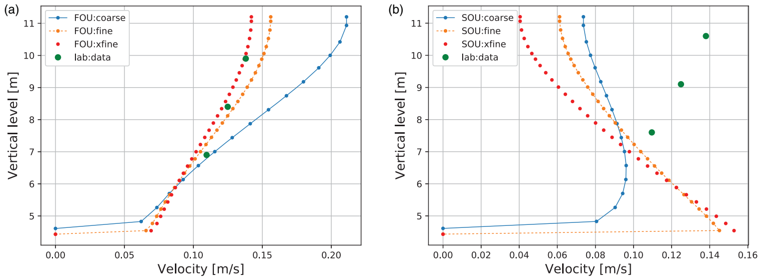

Figure 5. Sensitivity on grid resolution. Computed and measured streamwise velocities (u_x) for three vertical profiles in the Khimti sand trap. All velocity profiles are measured at different vertical lines 67.5 m downstream the sand trap inlet. Both sub figures a) and b) correspond to line b) in Figure 2. The labels refers to the discretization scheme, FOU = first-order upwind scheme, SOU = second-order upwind scheme, and *coarse, fine, xfine*, refers to the different grid resolutions.(a) FOU = first-order upwind scheme. (b) SOU = second-order upwind scheme.

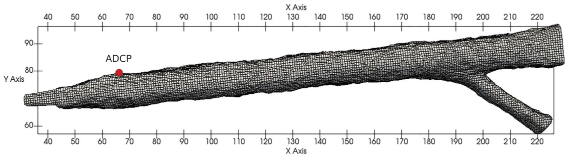

Figure 6. Model of Tonstad sand trap 3. Top view. Coordinates in meters.

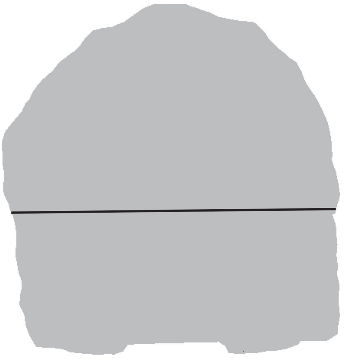

Figure 7. The cross-sections of the Tonstad sand trap where the ADCP measurements were done. The horizontal line in the figure corresponds to the line were the velocities were measured. The longitudinal position of this cross-section is indicated in Figure 6.

the ADCP is illustrated in Figure 7. These measurements were employed for validation of the numerical model.

The tunnel section was 200 m long, had a maximum height of 10 m, and a maximum width of 15 m. A generated mesh of the model is illustrated in Figure 6. A stereo-lithography (STL) file, made from a scanned point cloud of the tunnel, was available and used for the mesh generation. The tunnel was modeled in full size. The mesh was constructed by using `blockMesh` and `snappyHexMesh`, which are the meshing tools incorporated in OpenFOAM. The different ADCP devices were placed at different locations along the tunnel. The simulations were run with the `simpleFoam` solver in OpenFOAM. This is the OpenFOAM implementation of the SIMPLE routine (Patankar & Spalding, 1972) and contains both the standard SIMPLE version and its consistent formulation, SIMPLEC (OpenFOAM the openfoam foundation, n.d.). In this study, the consistent version SIMPLEC was utilised.

4.1. Boundary and initial conditions

The volumetric flow rate was set constant at the inlet, with a magnitude of 75 m^3/s. This value has been estimated by previous efficiency analyses of the turbines (Bråtveit & Olsen, 2015). The pressure flux was fixed at the inlet, whilst the turbulent variables k, ϵ, and ν_t were set to initial values, in accordance with Equations (7)–(9) (Versteeg, 2007):

$$k = \frac{3}{2}(UI)^2 = 0.0295\text{m}^2\text{s}^{-2} \tag{7}$$

$$\epsilon = \frac{C_\mu^{3/4} k^{3/2}}{l} = 2.01 \cdot 10^{-3}\ \text{m}^2\text{s}^{-3} \tag{8}$$

$$\nu_t = C_\mu \frac{k^2}{\epsilon} = 0.039\text{m}^2\text{s}^{-1} \tag{9}$$

The values for k and ϵ were based on the given discharge, and an assumption of a turbulent intensity (I) of 5%. The dissipation length scale, l, was estimated to be 10% of the width of the inlet, which was measured to 3.9 m. The turbulent model constant C_μ was set to 0.09. The velocity at the outlet was governed by the pressure, which was set to the value of $6 \cdot 10^5$ Pa. This pressure was also the initial value for the pressure in the sand trap. k and ϵ were set to zero gradient at the outlet. At the walls, the velocity was set to zero, and a zero gradient boundary condition was applied for the pressure. The near-wall behavior of k, ϵ, and ν_t was decided by wall functions, as described in Section 2.2. A rock-blasted tunnel has complex geometry with several roughness scales. When the grid is made finer, more roughness details are resolved. The outer boundary of the grid will therefore change according to the grid size. The sand grain roughness height k_s should account for the roughness that will not be captured by the grid. A requirement stated in the CFD literature is that $k_s < \frac{\Delta x}{2}$ (Blocken, Stathopoulos, & Carmeliet, 2007), where Δx in this case refers to the cell size of the cell adjacent to the surface. Based on the range of the near-wall grid sizes ($\Delta x = 0.03755 - 0.0625$) used in the simulations, the sand grain roughness height, k_s, was set to 0.01 m. The roughness constant, C_s, was set to 0.5 (ref. Equation (4)). This is given as a default value

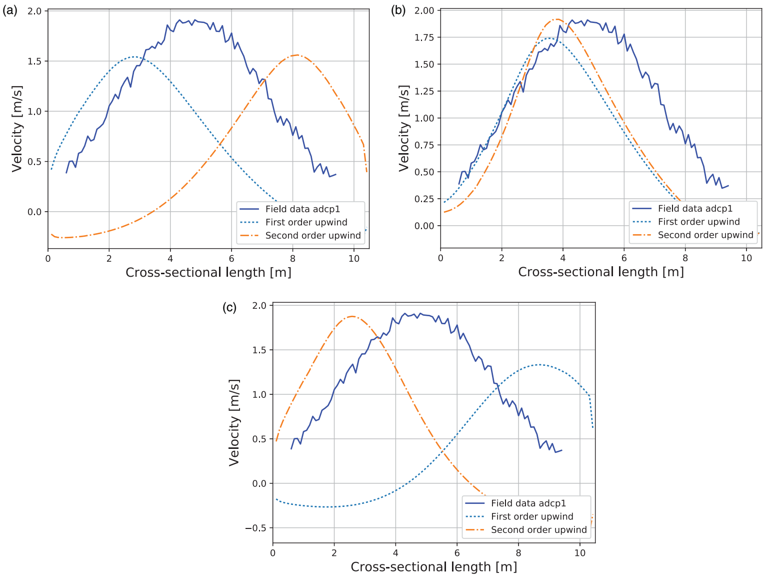

Figure 8. Lateral profiles of streamwise velocities (u_x) from the ADCP at Tonstad sand trap for first- and second-order upwind scheme for different turbulence models. These cases are simulated on grids with 19 million cells and grid sizes of $\Delta x = 0.25 - 0.125 - 0.0625$ m, where the grid is refined towards the wall. Each refinement layer consists of six cells. (a) $k - \epsilon$. (b) realizable $k - \epsilon$. (c) RNG $k - \epsilon$.

in the literature (Blocken et al., 2007). The flow within the sand trap was considered incompressible. Initially, the tunnel was filled with stagnant water, with a pressure of $6 \cdot 10^5$ Pa.

4.2. Results Tonstad

4.2.1. Discretization scheme

The simulation outputs from the Khimti sand trap model predicted a total change in the flow pattern, strongly dependent on the order of the discretization scheme used. Based on this, a remarkable point for the analysis on Tonstad was to investigate whether the same would apply to this sand trap. The first- and second-order upwind schemes were used to test this hypothesis. The effect of the discretization scheme was tested for different grid sizes. The results from these simulations are depicted in Figures 8 and 9. Figure 8 illustrates the results obtained from simulations on the grid with 19 million cells. From these (Figures 8 (a and c)), it is evident that the jet converges towards different sides of the tunnel depending on the discretization scheme, both for the standard $k - \epsilon$- and the RNG $k - \epsilon$ models. The change of the discretization scheme appears to have limited effect on the results from the realizable $k - \epsilon$ model (Figure 8(b)).

Figure 9 illustrates the corresponding results using a refined grid with 50 million cells. At this grid resolution, the choice of discretization scheme does not seem to have any significant influence on the flow pattern at the ADCP. For both grid resolutions, the results generated using the realizable $k - \epsilon$ model seem to demonstrate the highest correspondence with the field measurements. The magnitude of the maximum velocity is calculated with relatively good accuracy. Nevertheless, the location of this maximum velocity is relatively skewed compared to the field measurements. This applies to all computation results presented in Figure 9. The field measurements show a relatively symmetric flow pattern. Also, the recirculation zone

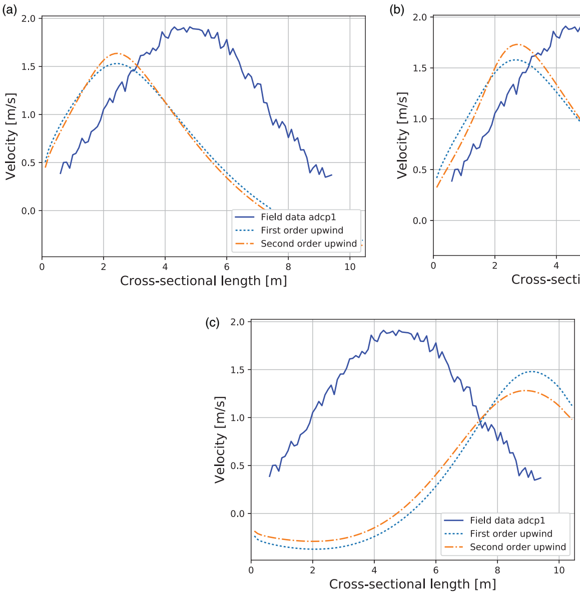

Figure 9. Lateral profiles of streamwise velocities (u_x) from the ADCP at Tonstad sand trap for first- and second-order upwind scheme for different turbulence models. These cases are simulated on grids with 50 million cells and grid sizes of $\Delta x = 0.15 - 0.075 - 0.03755$ m, where the grid is refined towards the wall. Each refinement layer consists of six cells. (a) $k - \epsilon$ (b) realizable $k - \epsilon$ (c) RNG $k - \epsilon$.

found in the calculations is not identified in the field measurements.

The calculated flow field of the entire tunnel cross-section at the location of the ADCP is illustrated in Figure 10. These Figures 10(a,b) are from simulations on the 19 million cells grid using the RNG $k - \epsilon$ turbulence model. In Figure 10(a,b), recirculation zones are identified in the lower right and left corner, respectively. These zones are also recognized in Figure 11, which shows a top view of the flow situation. Apart from the fact that the jet follows trajectories on different sides of the tunnel, the flow situation seems similar in the two cases. A recirculation zone is formed at a lower side wall, and the maximum velocity is located in the upper part of the tunnel. Nevertheless, the results indicate that the length of the high-velocity jet is longer for the second-order scheme than for the first-order scheme (Figure 11).

4.2.2. *Grid sensitivity*

A basic requirement for a CFD calculation is to obtain a grid independent solution (Versteeg, 2007). As the calculation domain gets sufficiently large, and the flow attains a highly turbulent state, the cell density needed to obtain a grid independent solution might be computationally demanding. Nevertheless, the starting point in this study was to carry out simulations starting with a coarse grid, and refining the grid until a grid independent solution was obtained. The effects of grid refinement towards the wall were also examined. All simulations within this grid sensitivity analysis were calculated using the second-order upwind discretization scheme for the convective term in Navier-Stokes equation.

The grid sensitivity analysis for the standard $k - \epsilon$ model is shown in Figures 12(a), 13 and 14. From these depictions, it is evident that the path of the jet at the ADCP is predicted at different locations depending upon

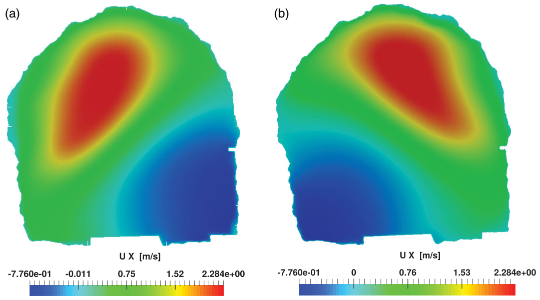

Figure 10. RNG $k - \epsilon$. Streamwise velocity profiles (u_x) of the cross-section of the ADCP at Tonstad sand trap. The ADCP is measuring along a horizontal line in the middle part of the cross-section (cf. Figure 7). The path of the jet at this cross section alters completely as function of the discretization scheme when a grid of 19 million cells is used. (a) Second-order upwind and (b) first-order upwind.

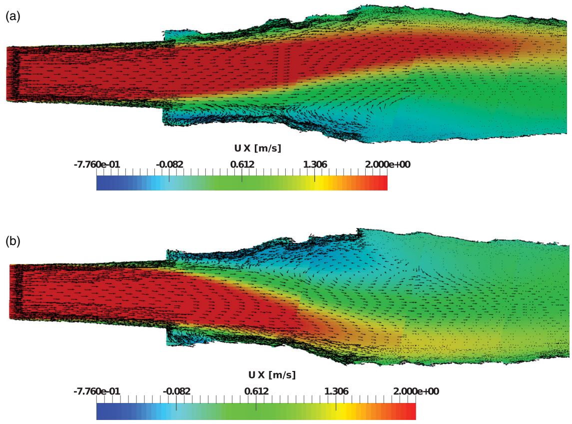

Figure 11. RNG $k - \epsilon$. Streamwise velocity profiles (u_x) for the first part of the tunnel of Tonstad sand trap, top view. The first 40 meters of the sand trap is shown, which includes the region measured by the ADCP. The vertical coordinate of this cross-section corresponds to the velocity profile measured by the ADCP (cf. Figure 8(c) and Figure 7). The path of the jet in this section alters completely as function of the discretization scheme when a grid of 19 million cells is used. (a) RNG $k - \epsilon$ – second-order upwind and (b) RNG $k - \epsilon$ – first-order upwind.

the grid resolution. For the coarsest grid (3 million cells), the location of the jet is predicted to be in the upper centre of the tunnel. This location corresponds with the field measurements. Nevertheless, the magnitude of the velocity is considerably lower than in the field measurements. The maximum velocity calculated on the finer grids corresponds better with the field measurements (see Figure 12(a)). For the finest grids (40 and 50 million cells), the jet appears to converge to the left side of the tunnel. This is not in accordance to the field measurements. Increasing the number of cells from 40 to 50 million seemingly had limited effect on the result. Different from the results at the finer grid resolutions, a recirculation zone is found along the whole width of the

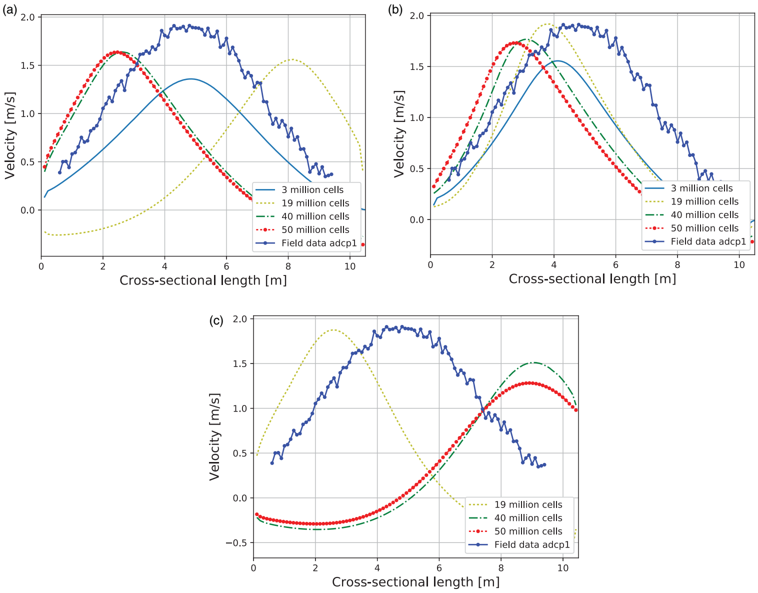

Figure 12. Lateral profiles of streamwise velocities (u_x) from the ADCP at Tonstad sand trap using different grid resolutions. For each turbulence model the cases were calculated on three different grids containing 19, 40 and 50 million cells, respectively. For the standard $k-\epsilon$- and the realizable $k-\epsilon$ model, an additional case with 3 million cells and no wall refinement was calculated as well. (a) $k-\epsilon$. (b) realizable $k-\epsilon$. (c) RNG $k-\epsilon$.

tunnel floor at the cross-section of the ADCP for the coarsest grid resolution (see Figure 14).

Unlike the results for the standard $k-\epsilon$ model, the realizable $k-\epsilon$ model predicts results that are relatively insensitive to the grid resolution (see Figure 12(b)). For all tested grid resolutions, the jet converged towards the left side of the tunnel. As the grid was refined, the path of the jet tended to be predicted further away from the middle of the tunnel and closer to the wall. This feature was also identified using the standard $k-\epsilon$ model.

In addition to the standard $k-\epsilon$ and the realizable $k-\epsilon$ model, the RNG $k-\epsilon$ turbulence model was tested. The corresponding results using this model are illustrated in Figure 12(c). Contradictory to what was observed for the other turbulence models, the jet tends to converge to the right side of the tunnel for the finer grid resolutions (40 and 50 million cells) for the RNG $k-\epsilon$ model. Nevertheless, at the coarsest grid resolution used for this turbulence model (19 million cells), the jet converges to the opposite side of the tunnel. This was another instance, where considerable variability in simulation outputs were observed, as a result of changing a numerical input parameter of the calculation.

4.2.3. Sensitivity of turbulence model

To investigate the effect of changing the turbulence model, several versions of the $k-\epsilon$ model were tested at different grids. Figure 15, 16 and 17 present the results from this analysis. At each grid resolution tested, one of the turbulence models predicts the jet to follow a path on the opposite side of the tunnel than the other two. At the coarsest grid resolution (19 million cells), the results using the standard $k-\epsilon$ model converges to the right side of the tunnel, while the jet shifts to the other side using the other turbulence models. For the finer grid resolutions, it is the RNG $k-\epsilon$ model that

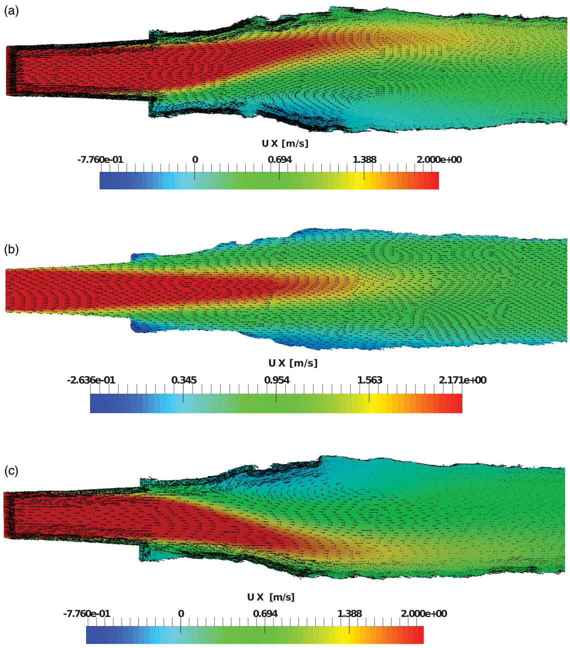

Figure 13. Standard $k - \epsilon$ turbulence model. Streamwise velocity profile (u_x) of the first part of the tunnel of Tonstad sand trap, top view. The first 50 m of the sand trap is shown, which includes the region measured by the ADCP. The vertical coordinate of these cross-sections corresponds to the velocity profile measured by the ADCP (cf. Figure 7 and Figure 12). The path of the jet in this section alters completely as function of grid resolution. (a) 40 million cells, (b) 3 million cells and (c) 19 million cells.

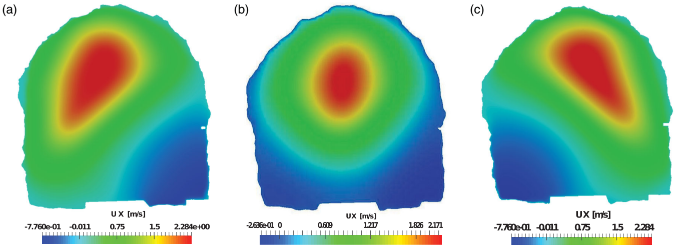

Figure 14. Standard $k - \epsilon$. Streamwise velocity profile (u_x) of the cross-section of the ADCP at Tonstad sand trap. The ADCP are measuring along a horizontal line in the upper part of the cross-section (cf. Figure 7). The path of the jet at this cross section alters completely as function of the grid size for the standard $k - \epsilon$ model. (a) 40 million cells, (b) 3 million cells and (c) 19 million cells.

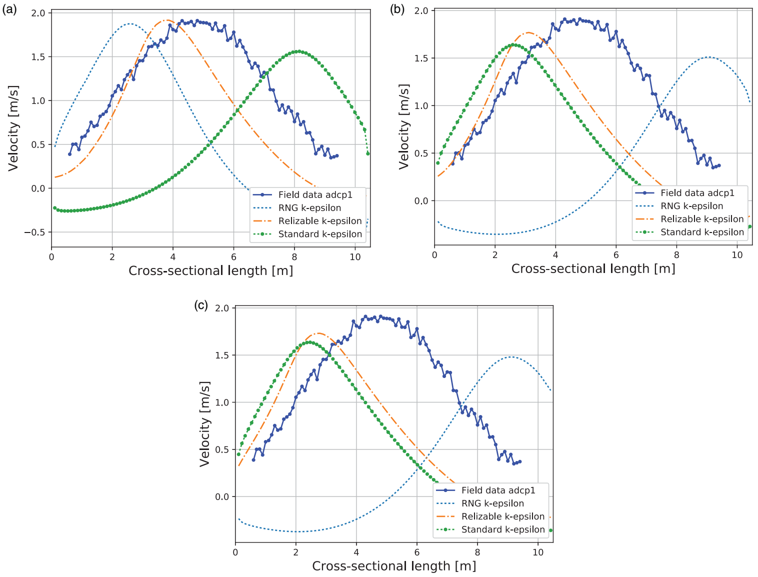

Figure 15. Lateral profiles of streamwise velocities (u_x) from the ADCP at Tonstad sand trap. Sensitivity on turbulence model for the different grid sizes. (a) 19 million cells, (b) 40 million cells and (c) 50 mill cells.

predicts the jet to follow the right side of the tunnel, while the other models predict it to the left side. The situation is similar for the two finest grid resolutions (40 million cells and 50 million cells). These results can also be identified from the previous sections (Section 4.2.2 and Section 4.2.1).

4.2.4. Stationary vs. transient simulations

A working hypothesis was that the different solutions could probably result if the jet was in fact oscillating between the left and the right side of the tunnel. To investigate if this could be the case, the field data was further analysed. In Figure 18, development of the field data are plotted for a period with stable production. For the plotted period, the production was relatively stable at 300 MW. Each line on the plot is averaged over 10-min intervals. Figure 18(a) suggests that minor fluctuations in velocity peaks were observed. For the first 10 min, the velocity peak was located around 3.5 m from the tunnel wall. For the next 10 min, it was located more to the centre, and for the next period, the peak was located around 5.5 m from the tunnel wall. Further, it gradually transitions back for the next two time periods. Nevertheless, changes in position for the velocity peak were not as prominent as for the simulated data. Figure 18(b) plots the field data for another time period of stable production. From this figure, any prominent trend in position change of the jet is hard to identify. The small variations in the time averaged values might be caused by limited quality of the measurements (Bråtveit & Olsen, 2015). The variations between the time averaged values from the different time intervals are largest far away from the wall (see Figure 18(b)). Based on the findings of Bråtveit and Olsen (2015), the quality of the measurements are considered satisfactory only up to a distance of 5 m away from the ADCP apparatus. For the time period plotted in 18(b), the correlation between the time averaged measurements for the different time intervals, appears to be relatively high the first 5 m from the ADCP.

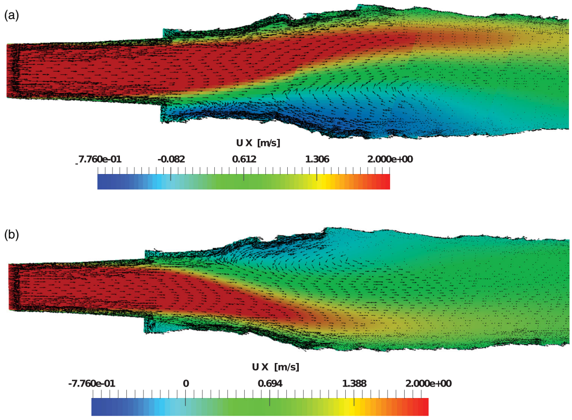

Figure 16. Standard $k-\epsilon$ vs RNG $k-\epsilon$ turbulence model. Streamwise velocity profiles (u_x) for the first part of the tunnel of Tonstad sand trap, top view. The vertical coordinate of this cross-section corresponds to the velocity profile measured by the ADCP (cf. Figure 7 and Figure 15). The path of the jet at this cross-section alters completely when the turbulence model is changed from the standard $k-\epsilon$ to the RNG $k-\epsilon$ model. (a) RNG $k-\epsilon$. (b) Standard $k-\epsilon$.

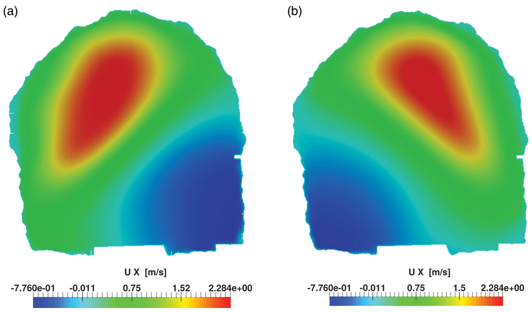

Figure 17. Standard $k-\epsilon$ vs RNG $k-\epsilon$ turbulence model. Streamwise velocity profiles (u_x) of the cross-section of the ADCP at Tonstad sand trap. The ADCP is measuring along a horizontal line in the upper part of the cross-section (cf Figure 7). The path of the jet at this cross-section alters completely when the turbulence model is changed from the standard $k-\epsilon$ to the RNG $k-\epsilon$ model. (a) RNG $k-\epsilon$. (b) Standard $k-\epsilon$.

4.3. Discussion Tonstad sand trap

The observed results demonstrate that there exist multiple solutions of the Navier-Stokes equations for the flow field within this sand trap. This corresponds to findings by Bråtveit and Olsen (2015). All simulations appear to converge to steady solutions, but different computational setups predict different trajectories for the jet at the expansion zone of the tunnel. Using identical boundary conditions, the jet converges to solutions on either sides of the tunnel, and in the centre, depending on the discretization scheme, grid resolution, and the turbulence

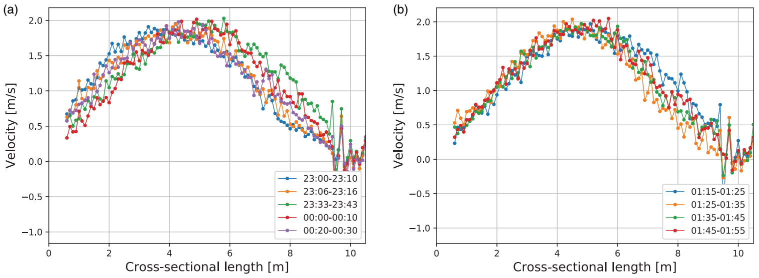

Figure 18. Lateral profiles of streamwise velocities (u_x) for the ADCP at Tonstad sand trap. Analysis of field data. Time averaged over 10 min, two periods plotted. First period starts from 23:00:00 at the 15th of February 2012 and the second period starts from 01:15:00 at the 16th of February 2012. For both periods the production is approximately stable at a rate of 300 MW. (a) 23:00:00-00:30:00. (b) 01:15:00-01:55:00.

model utilised. Similar observations were identified by Kantoush et al. (2008). In a numerical experiment of sedimentation settling, the main flow tended to follow one of the sides of the basin. By applying small changes to the assumptions in the initial- and boundary conditions, the main flow switch to follow the other side of the basin. This behavior was further confirmed by laboratory experiments.

The role of the sand trap in a hydro power tunnel is to reduce the size of the sediments that are transported with the flow. The main purpose of this is to avoid severe damage to the turbine blades. This is done by decreasing the velocity of the water flow, which in turn allows for sediments to settle. To reduce the velocity of the inlet flow, many sand traps are equipped with an expansion zone. Increasing the width of the tunnel will reduce the flow velocity, which increases the amount of sediment settling. In addition, the expansion will introduce turbulence and recirculation zones and create a complicated flow pattern. Recirculation zones and turbulence will lead to swirling of the sediments, and thereby work against the process of sediment settling. This is very unfavorable for effective hydraulic performance of the sand trap (Brox, 2016). In addition to the magnitude of the velocity, important factors influencing the trap efficiency will then be the length and extension of the high-velocity inlet jet, as well as the placement of the recirculation zone. In this study, the path of the inlet jet and the placement of the recirculation zone were changed dependent of the set up of discretization scheme, grid resolution and turbulence model. In many sand traps, a series of tranquilizing racks are placed in the expansion zone to enhance the flow conditions with regards to sediment settling. The purpose of these racks is to homogenise the flow and thus reduce the turbulent velocity fluctuations (Paschmann, Fernandes, Vetsch, & Boes, 2017) in turbulent regions of the expansion zone. Nevertheless, construction of such racks has not been common in Norwegian hydro power plants and was not present in the expansion section of Tonstad sand trap. For this sand trap, a high-velocity jet downstream of the expansion zone was identified both from the field measurements and in the results from the numerical simulations.

Changing the discretization scheme from first- to second-order upwind moved the jet from the left- to the right-hand side of the tunnel, when calculated on the grid of 19 million cells. These results were found both for the standard $k - \epsilon$ model and the RNG $k - \epsilon$ model. Apart from the fact that the jet followed trajectories on either sides of the tunnel, the flow patterns were similar for the different discretization schemes tested. For both schemes, a high-velocity jet followed one side of the tunnel, and a recirculation zone was found at the opposite side. Whether the jet follows the left or right side of the tunnel is of little importance for the sediment settling, as long as the remaining flow features are similar. The length of the high-velocity jet seemed to be larger using the more accurate second-order discretization scheme. This could affect the efficiency of the sediment settling (Nøvik, Dudhraj, Olsen, Bishwakarma, & Lia, 2014).

For the finer grid resolutions, no significant differences were detected between the different discretization schemes. More equal results for first- and second-order discretization schemes are expected as the grid resolution increases (Versteeg, 2007). This is due to the fact that numerical diffusion, which might be an issue for first-order discretization schemes, is reduced (Versteeg, 2007). In other words, numerical diffusion will introduce inaccuracy to the calculations, but should in principle not lead to results that are totally different as seen from this study.

Changing the grid from relatively coarse (3 million cells) to finer (19, 40 and 50 million cells) made the jet follow the middle, right and left side of the tunnel, when using the standard $k-\epsilon$ model for turbulence modeling. Similar to the sensitivity analysis on discretization scheme, the flow pattern was comparable, but on different sides of the tunnel. This means that with regard to sand trap efficiency, this should not be of significant importance. Nevertheless, for the coarsest grid resolution, the jet was predicted to follow the upper centre of the tunnel and a recirculation zone was spanning the whole width of the ground section of the tunnel. This might affect the efficiency of the sand trap.

All converged solutions considered, it is evident that in the majority of the cases, the jet follows the left wall of the tunnel. This is not according to what is seen from the field data, where the jet seems to follow the middle of the tunnel. Nevertheless, similar behavior was identified by (Kantoush et al., 2008) in a physical model. For the majority of the experiments, the flow was aligned along one of the sides of the basin, and occasionally it changed to the other side.

To investigate whether the multiple solutions found in the simulations could be due to some transient features of the flow, the field measurements were analysed to consider whether the jet was in fact oscillating between the left and right side of the tunnel. Any prominent oscillations could not be proved to exist based on the available field measurements. The fact that velocity measurements are only available for one horizontal line at three cross-sections of the tunnel, and also that questions are raised concerning the validity of the measurements data for the right side of the tunnel (Bråtveit and Olsen (2015), limits the ability to draw strict conclusions regarding the behaviour of the flow and the accuracy of the flow field calculations.

To be able to draw further conclusions on this, field measurements covering more features of the flow would be required. Moreover, transient simulations using detached eddy simulation (DES) or large eddy simulation (LES) could be performed. In these models, the motions of the turbulent eddies are captured, which gives an improved capability to capture transient features within the flow. Nevertheless, the use of LES in flows with Reynolds number in the range of 10^6, as in this case, has shown to be challenging (Catalano, Wang, Iaccarino, & Moin, 2003). The use of LES might have greater applicability replicating physical model studies, where the Reynolds number will be smaller.

Based on the analysis of the field data and the magnitude of the Reynolds number, simulations based on LES were not performed in the current study.

5. Conclusion

Durrani et al. (2015), Kamenetskiy et al. (2014) and Robinson (1976) reported multiple solutions when solving the steady Navier-Stokes equations. The current study introduces new examples where the solutions of the Navier-Stokes equations solved by CFD are not unique. The findings from the mentioned studies suggest that interpretation of results from CFD computations should be treated with caution. The results should be validated by physical measurements, and sensitivity analyses for grid resolution, turbulence model and discretization scheme should be carried out.

The results from CFD simulations done at Khimti- and Tonstad hydro power plants, failed to produce a unique solution for a flow field within a sand trap, using a RANS model. The main reason for this is that the expansion zone, which is the crucial part of the sand trap, creates a complicated flow pattern where a high turbulent zone is created. None of the sand traps included in this study were equipped with tranquilizing racks, which could have had a beneficial impact on the flow pattern by homogenising the flow.

According to the current study findings, changes in input parameters as discretization scheme, grid resolution and turbulence model could have significant impacts on the computed flow pattern within sand traps. If CFD computations are performed with the aim of deciding the settling efficiency, discrepancies could arise due to changes in the numerical parameters investigated in this study. Nevertheless, major part of the sediment settling takes place downstream the expansion zone. Here, the fluid velocity is reduced, and a more uniform flow field exists.

The study of the Khimti sand trap suggests that the boundedness of the discretization scheme might be of higher importance than its order, with regards to accurately predicting the flow pattern within a sand trap.

To further validate the results from these case studies, transient analyses using DES could be performed. Field measurements covering more features of the flow would be required to be able to further validate the CFD calculations.

Note

1. u^+ =non-dimensional velocity, $y^+ =$ non-dimensional position

Acknowledgements

The authors acknowledge the support and cooperation of NOTUR for providing computational time on Vilje and Fram HPC clusters.

Disclosure statement

No potential conflict of interest was reported by the authors.

References

Akbarian, E., Najafi, B., Jafari, M., Ardabili, S. F., Shamshirband, S., & Chau, K.w. (2018). Experimental and computational fluid dynamics-based numerical simulation of using natural gas in a dual-fueled diesel engine. *Engineering Applications of Computational Fluid Mechanics*, *12*(1), 517–534. doi:10.1080/19942060.2018.1472670.

Aryal, P., & Olsen, N. R. (2001). 3D CFD modelling of water flow in the sand trap of Khimti Hydropower Plant, Nepal. In *Proceedings of the 4th international conference on hydropower development, Bergen, Norway*.

Blocken, B., Stathopoulos, T., & Carmeliet, J. (2007). CFD simulation of the atmospheric boundary layer: Wall function problems. *Atmospheric Environment*, *41*(2), 238–252. Retrieved from http://www.sciencedirect.com/science/article/pii/S135223100600834X

Bråtveit, K., & Olsen, N. R. B. (2015). Calibration of horizontal acoustic doppler current profilers by three dimensional cfd simulations. *Engineering Applications of Computational Fluid Mechanics*, *9*(1), 41–49. doi:10.1080/19942060.2015.1004807.

Brox, D. (2016). Design and functional requirements of rock traps for pressure tunnels. *The International Journal on Hydropower and Dams*, 46–52.

Catalano, P., Wang, M., Iaccarino, G., & Moin, P. (2003, Aug). Numerical simulation of the flow around a circular cylinder at high reynolds numbers. *International Journal of Heat and Fluid Flow*, *24*(4), 463–469. doi10.1016/s0142-727x(03)00061-4

Chau, K., & Jiang, Y. (2002, Apr). Three-dimensional pollutant transport model for the pearl river estuary. *Water Research*, *36*(8), 2029–2039. doi:10.1016/s0043-1354(01)00400-6

Chau, K., & Jiang, Y. (2004). A three-dimensional pollutant transport model in orthogonal curvilinear and sigma coordinate system for pearl river estuary. *International Journal of Environment and Pollution*, *21*(2), 188. doi:10.1504/ijep.2004.004185

Durrani, F., Cook, M. J., & McGuirk, J. J. (2015). Evaluation of LES and RANS CFD modelling of multiple steady states in natural ventilation. *Building and Environment*, *92*(Supplement C), 167–181. Retrieved from http://www.sciencedirect.com/science/article/pii/S0360132315001936

Elger, D., Williams, B., Crowe, C., & Roberson, J. (2013). *Engineering fluid mechanics* (10th ed. si version). Singapore: Wiley.

Esmaeili, T., Sumi, T., Kantoush, S. A., Haun, S., & Rüther, N. (2016). Three-dimensional numerical modelling of flow field in shallow reservoirs. *Proceedings of the Institution of Civil Engineers – Water Management*, *169*(5), 229–244. doi:10.1680/jwama.15.00011

Esmaeili, T., Sumi, T., Kantoush, S., Kubota, Y., Haun, S., & Rüther, N. (2017, Nov). Three-dimensional numerical study of free-flow sediment flushing to increase the flushing efficiency: A case-study reservoir in japan. *Water*, *9*(11), 900. doi:10.3390/w9110900

Franke, J., Hellsten, A., Schlunzen, K. H., & Carissimo, B. (2011). The cost 732 best practice guideline for cfd simulation of flows in the urban environment: A summary. *International Journal of Environment and Pollution*, *44*(1/2/3/4), 419. doi:10.1504/IJEP.2011.038443

Hess, J., & Smith, A. (1967). Calculation of potential flow about arbitrary bodies. *Progress in Aerospace Sciences*, *8*, 1–138. doi:10.1016/0376-0421(67)90003-6

Hydroconsult, B.P.C. (1997). *Khimti 1 hydropower project hydraulic model study* (Final Report). Kathmandu: River Research Laboratory.

Jameson, A., & Baker, T. (1983, July). Solution of the euler equations for complex configurations. *6th Computational Fluid Dynamics Conference Danvers*. doi:10.2514/6.1983-1929.

Kamenetskiy, D. S., Bussoletti, J. E., Hilmes, C. L., Venkatakrishnan, V., Wigton, L. B., & Johnson, F. T. (2014, August). Numerical evidence of multiple solutions for the reynolds-averaged Navier-Stokes equations. *AIAA Journal*, *52*(8), 1686–1698. doi:10.2514/1.J052676.

Kantoush, S. A., Bollaert, E., & Schleiss, A. J. (2008, Sep). Experimental and numerical modelling of sedimentation in a rectangular shallow basin. *International Journal of Sediment Research*, *23*(3), 212–232. doi:10.1016/s1001-6279(08)60020-7

Launder, B., & Spalding, D. (1974). The numerical computation of turbulent flows. *Computer Methods in Applied Mechanics and Engineering*, *3*(2), 269–289. Retrieved from http://www.sciencedirect.com/science/article/pii/0045782574900292

Mayer-Peter, E., & Mueller, R. (1948). Formulas for bed load transport. In *Proceedings from the Second Meeting of the International Association for Hydraulic Structures Research, Stockholm, Sweden*.

Nikuradse, J., & Nikuradse, J. (1933). Laws of flow in rough pipes. *VDI Forschungsheft*, 361.

Nøvik, H., Dudhraj, A., Olsen, N., Bishwakarma, M.B., & Lia, L. (2014). Numerical modeling of nonuniform flow in settling basins. *HYDRO Nepal Journal*, *14*, 27–35.

Olsen, N. R., & Kjellesvig, H. M. (1999). Three-dimensional numerical modelling of bed changes in a sand trap. *Journal of Hydraulic Research*, *37*(2), 189–198.doi:10.1080/00221689909498305

Olsen, N. R. B., & Skoglund, M. (1994). Three-dimensional numerical modeling of water and sediment flow in a sand trap. *Journal of Hydraulic Research*, *32*(6), 833–844. doi:10.1080/00221689409498693

Paschmann, C., Fernandes, J. N., Vetsch, D. F., & Boes, R. M. (2017). Assessment of flow field and sediment flux at alpine desanding facilities. *International journal of river basin management*, *15*(3), 287–295.

Patankar, S., & Spalding, D. (1972). A calculation procedure for heat, mass and momentum transfer in three-dimensional parabolic flows. *International Journal of Heat and Mass Transfer*, *15*(10), 1787–1806. Retrieved from http://www.sciencedirect.com/science/article/pii/0017931072900543

Ramezanizadeh, M., Nazari, M. A., Ahmadi, M. H., & wing Chau, K. (2018). Experimental and numerical analysis of a nanofluidic thermosyphon heat exchanger. *Engineering Applications of Computational Fluid Mechanics*, *13*(1), 40–47. doi:10.1080/19942060.2018.1518272

OpenFOAM the openfoam foundation (n.d.). Retrieved from https://openfoam.org.

Rijn, L. C. (1982). Equivalent roughness of alluvial bed. *Journal of the Hydraulics Division*, *108*(10), 1215–1218.

Robinson, W. A. (1976, Jan). The existence of multiple solutions for the laminar flow in a uniformly porous channel with suction at both walls. *Journal of Engineering Mathematics*, *10*(1), 23–40.

Ruether, N., & Olsen, N. R. B. (2006). 3D modeling of transient bed deformation in a sine-generated laboratory channel with two different width to depth ratios. In *Proceedings of river flow 2006 conference, Lisbon, Portugal*.

Ruether, N., Singh, J. M., Olsen, N. R. B., & Atkinson, E. (2005, Mar). 3-D computation of sediment transport at water intakes. *Proceedings of the Institution of Civil Engineers – Water Management*, *158*(1), 1–7. doi:10.1680/wama.2005.158.1.1

Schlichting, H. (1979). *Boundary-layer theory* (7th ed.). New York, NY: McGraw-Hill.

Shih, T. H., Liou, W. W., Shabbir, A., Yang, Z., & Zhu, J. (1995). A new k-epsilon eddy viscosity model for high reynolds number turbulent flows. *Computers and Fluids*, *24*(3), 227–238. Retrieved from http://www.sciencedirect.com/science/article/pii/004579309400032T

Török, G., Baranya, S., & Rüther, N. (2017). 3d CFD modeling of local scouring, bed armoring and sediment deposition. *Water*, *9*(1), 56. doi:10.3390/w9010056

Versteeg, H. (2007). *An introduction to computational fluid dynamics : The finite volume method* (2nd ed.). Harlow: Pearson/Prentice Hall.

Viroulet, S., Baker, J. L., Edwards, A. N., Johnson, C. G., Gjaltema, C., Clavel, P., & Gray, J. M. N. T. (2017, February). Multiple solutions for granular flow over a smooth two-dimensional bump. *Journal of Fluid Mechanics*, *815*, 77–116. doi:10.1017/jfm.2017.41

Xu, H., Lin, P., & Si, X. (2014). A study of multiple solutions for the navier-stokes equations by a finite element method. *Numerical Mathematics: Theory, Methods and Applications*, *7*(1), 107–122.

Yakhot, V., Orszag, S. A., Thangam, S., Gatski, T. B., & Speziale, C. G. (1992, July). Development of turbulence models for shear flows by a double expansion technique. *Physics of Fluids A*, *4*, 1510–1520.

A.2 Paper II: An improved air entrainment model for stepped spillways

An improved air entrainment model for stepped spillways

Silje Kreken Almeland[a,*], Timofey Mukha[b], Rickard E. Bensow[b]

[a]*Norwegian University of Science and Technology, Department of Civil and Environmental Engineering, NO-7491 Trondheim, Norway*
[b]*Chalmers University of Technology, Department of Mechanics and Maritime Sciences, Hörsalsvägen 7A, SE-412 96 Gothenburg, Sweden*

Abstract

Numerical modelling of flow in stepped spillways is considered, focusing on a highly economical approach combining interface capturing with explicit modelling of air entrainment. Simulations are performed on spillways at four different Froude numbers, with flow parameters selected to match available experimental data. First, experiments using the model developed by Lopes et al. (Int. J. Nonlin. Sci. Num., 2017) are conducted. An extensive simulation campaign is used to carefully evaluate the predictive accuracy of the model, the influence of various model parameters, and sensitivity to grid resolution. Results reveal that, at least for the case of stepped spillways, the number of parameters governing the model can be reduced. A crucial identified deficiency of the model is its sensitivity to grid resolution. To improve the performance of the model in this respect, modifications are proposed for the interface detection algorithm and the transport equation for the volume fraction of entrained air. Simulations using the improved model formulation demonstrate better agreement with reference data for all considered flow conditions. A parameter-free criterion for predicting the inception point of air entrainment is also tested. Unfortunately, the accuracy of the considered conventional turbulence models proved to be insufficient for the criterion to work reliably.

Keywords: Air entrainment modelling, numerical modelling, CFD, OpenFOAM, self-aeration, stepped spillway

---

1. Introduction

Along with a renewed interest in stepped spillways as a flood overflow structure and energy dissipator in hydraulic engineering, attempts at gaining a better physical description of spillway flows have also intensified. A process that is especially challenging to study by means of both physical and numerical experiments, is the self-aeration of the spillway. Yet, since large quantities of entrained air lead to higher flow depths, release energy, and reduce the potential for damage caused by cavitation, accurate prediction of aeration is crucial for spillway design. In this work, mathematical modelling and simulation of air entertainment is in focus. To put the present contribution into context, a brief review of the physics of air entrainement in spillways is given below, followed by an overview of past attempts of accounting for them in a numerical setting.

Generally, air entrainment is driven by turbulent motion and occurs when the turbulent forces at the free surface overcome the stabilizing effects of surface tension and buoyancy [10]. Applied to spillways, it has since the early work of Straub and Anderson [26] been widely accepted that the onset of self-aeration takes place when the turbulent boundary layer, developed from the crest, reaches the free surface. This location is commonly referred to as the 'inception point'. Several contributions consider the onset of the aeration in detail [6; 33; 28], and empirical relations exist for the distance to the inception point from the spillway crest

---

[*] Corresponding author

Email addresses: `silje.k.almeland@ntnu.no` (Silje Kreken Almeland), `timofey@chalmers.se` (Timofey Mukha), `rickard.bensow@chalmers.se` (Rickard E. Bensow)

Preprint submitted to Applied Mathematical Modelling *September 11, 2020*

[2; 18; 4]. Boes and Hager [2] proposed a computable definition of the inception point as the location where the pseudo-bottom air concentration is 0.01.

Downstream of the inception point, entrainment quickly leads to a complete distortion of the perceivable air-water interface into a thick layer occupied by a mixture of the two phases. Furthermore, experimental data exhibits a non-negligible concentration of air all the way down to the surface of steps. The work of Pfister and Hager [22] presents a detailed account of the transport mechanism responsible for that. It is shown that transiently occurring air throughs can penetrate deep enough to hit the edge of the steps. This leads to brake-up and eventual entrapment of air pockets in the recirculating flow occupying the corners of the steps.

An important property of stepped spillway flow is that it eventually reaches a state where its average properties no longer alter in the streamwise direction. The associated distributions of flow variables are referred to as uniform conditions. The part of the flow preceding this state is called the development region. Empirical expressions for the extent of the development region have been given by several authors [4; 1], as well as relations for the surface height in the different flow regions along the spillway [4; 2; 18].

When it comes to numerical modelling of the complicated multiphase physics discussed above, one can generally distinguish two approaches. One is to try to explicitly capture these phenomena using a high-fidelity scale-resolving simulation framework. This necessitates using very dense computational grids and therefore consuming vast amounts of computational resources. For this reason, results from such simulations of spillways have not yet been reported in the literature. However, works on other aerating flows can be found, e.g. [21] for the case of the hydraulic jump.

The alternative approach is to introduce an additional model accounting for the entrainment of air. Different ways of introducing such modelling have been proposed, also varying in the general multiphase simulation methodology into which they are fit. Efforts within the framework of the two-fluid model (also referred to as Euler-Euler) have been reported in [12; 30; 31; 17; 20]. In the context of interface-capturing methods, such as Volume of Fluid (VoF), the general idea is to introduce air entrainment as a subgrid model. Here the study of Hirt [13] can be distinguished as pioneering. This model was implemented in Flow3D® and has been used in publications on stepped spillways [27; 9]. Lopes et al. [16] incorporated the entrained air flux estimator developed in [17] into a VoF framework by introducing a separate transport equation for the entrained air. The solver is implemented in OpenFOAM®, and results from stepped spillway simulations are presented in the article.

In this work, we present further developments of the model by Lopes et al. [16]. To motivate the need for improvements, results from a simulation campaign, in which the model in its current formulation is applied to spillway flow at four different Froude numbers, are presented. The simulations constituting the campaign vary in the employed grid resolutions and parameters of the model. Results from the second campaign, in which the model is modified as proposed here, are then presented, demonstrating better accuracy and robustness. The article is supplemented by a dataset containing all the simulation results.[1]

The reminder of this article is structured as follows. Section 2 describes the computational methods used in the performed computations. In Section 3, the setup of the stepped spillway simulations is discussed. Section 4 presents the air entrainment model developed by Lopes et al. [16]. Section 5 contains results from the simulation campaign in which the model of Lopes et al. [16] is used. Improvements to the air entrainment model are then proposed in Section 6, and corresponding simulation results are provided in Section 7. Concluding remarks are given in Section 8.

2. Computational fluid dynamics methods

2.1. Governing equations

The flow was simulated using the Volume of Fluid (VoF) multiphase modelling technique [14], in which a single set of governing equations is solved for all phases and the location of the interface is identified based on the values of the cell volume fraction of the liquid phase, α_l. Both fluids are considered incompressible and

---

[1] 10.6084/m9.figshare.12782339

immiscible. Furthermore, RANS turbulence modelling is adopted, leading to the following set of governing equations.

$$\frac{\partial \rho \overline{u}}{\partial t} + \nabla \cdot (\rho \overline{u} \otimes \overline{u}) = -\nabla \overline{p}_{\rho g h} - g x \nabla \rho + \nabla \left(\mu \left(\nabla \overline{u} + (\nabla \overline{u})^T \right) - \rho \overline{u' \otimes u'} \right) + f_s \tag{1}$$

$$\nabla \cdot \overline{u} = 0. \tag{2}$$

Here the overbar denotes the Reynolds average, ρ is the density, μ is the dynamic viscosity, u is the velocity vector, $p_{\rho g h} = p - \rho g \cdot x$ is the dynamic pressure, and f_s is the surface tension force. The latter is approximated using the Continuous Force Model, see [3] and also [24] for a detailed discussion in the context of OpenFOAM®. The term $\rho \overline{u' \otimes u'}$ represents the Reynolds stresses, which are to be approximated by the turbulence model.

An algebraic approach to account for the evolution of α_l is adopted, with the associated transport equation originally formulated as

$$\frac{\partial \alpha_l}{\partial t} + \nabla \cdot (\overline{u} \alpha_l) + \nabla \cdot (u^c (1 - \alpha_l) \alpha_l) = 0, \tag{3}$$

in OpenFOAM®'s VoF solvers. The third term in the equation is artificial and is meant to introduce additional compression of the interface to ensure its sharpness. However, here the formulation of this term is modified in order to accommodate it into the air entertainment modelling framework. The details are provided in Section 4. The definition of u^c is nevertheless not altered: It is aligned with the interface normal, and its magnitude is computed as $C_\alpha |\overline{u}|$, where C_α is an adjustable constant, here set to 1.

Given α, the material properties of the fluids are readily obtained as

$$\rho = \alpha_l \rho_l + (1 - \alpha_l) \rho_{air}, \qquad \mu = \alpha_l \mu_l + (1 - \alpha_l) \mu_{air}. \tag{4}$$

The indices l and air are used to refer to the water and air, respectively.

What remains to be discussed is the choice of turbulence model, which for the case of the stepped spillway is far from trivial. In principle, the model should be able to properly account for the interaction between the turbulent and multiphase structures in order to provide accurate prediction in the aerated region of the flow. None of the closures that have found widespread use were developed with this goal in mind. Nevertheless, it is common for conventional two-equation models to be used for aerated flows. In [16], which is the work this article largely builds upon, the k-ω SST model [19] is used for stepped spillway simulations. In [17], it is employed in simulations of a plunging jet and a hydraulic jump. For the latter, many studies also use the k-ϵ model and its variations, a comprehensive list of references can be found in Table 5 in [29]. Qian et al. [23] found the realisable k-ϵ model to be favourable for stepped spillway flow. Based on the above, we consider both the k-ω SST and the realisable k-ϵ model [25] and test which of them leads to better predictive accuracy.

It is pointed out in [11] that in the implementation of the above (and also other) turbulence models in OpenFOAM® the viscous diffusion terms are not treated consistently in regions with a non-zero density gradient. Since in the simulations of the spillway presented here a density gradient is present across the whole aerated part of the flow, this issue can have a significant effect on the results. The authors of [11] also provide alternative implementations, in which the inconsistency is resolved. Here, we test using both the default and the improved implementations.

2.2. Numerical methods

The computations are performed using OpenFOAM® version 5, provided by the OpenFOAM Foundation. This CFD tool is based on cell-centered finite volume discretization, which is de facto the industry standard. Two custom solvers are used in the study, implementing the air entraiment modelling presented in Sections 4 and 6. Both of them represent modifications of the solver `interFoam`, which is distributed with OpenFOAM®. This solver implements the VoF methodology discussed in Section 2.1. The governing equations are solved in segregated manner using a variant of the PISO algorithm [15].

A crucial component of the numerical setup is the selection of the spatial interpolation and time integration schemes. Generally, linear interpolation can be used in space except when considering convective fluxes. In the momentum equation, the latter are interpolated using the `limitedLinearV` scheme, which is a TVD scheme based on the Sweby limiter. The limiter is computed based on the direction of most rapidly changing gradient and then applied to all three velocity components. This improves stability but at a certain expense in terms of accuracy. For the convection of α in equation (3), a TVD scheme using the SuperBee limiter is used. The van Leer limiter was also considered, but SuperBee led to better results on coarser meshes due to being more compressive. Unfortunately, in a multi-dimensional setting, using a TVD scheme does not guarantee that the values of α will be bounded between 0 and 1. Therefore, OpenFOAM® utilizes an additional flux limiting technique, referred to as MULES. It is based on the Flux Corrected Transport theory developed Zalasak [32], more details can be found in [8]. The convective fluxes in the turbulence equations are discretized using the second order upwind scheme, called `linearUpwind`. This scheme is unbounded, but no significant effect of parasitic oscillations was observed even on coarse grids. Finally, as discussed in Section 4.2 below, the air entrainment model adds an advection-diffusion equation for the flow variable α_g, meant to indicate the distribution of the volume fraction of entrained air , to the system. Here, a TVD scheme using the van Leer limiter is employed.

The first-order implicit Euler scheme was used for time-stepping. The choice is not of particular importance here because the flow eventually arrives to an essentially steady state. Nevertheless, a CFL number ≤ 1 was neccessay to maintain in order to keep the simulations stable. This was achieved using adaptive time-stepping.

3. Simulation cases

This section presents the setup of the stepped spillway simulations used to evaluate the performance of the entrainment modelling. In order to have a reference with respect to which the accuracy of simulation results can be analysed, the flow and spillway parameters are selected to match those in the experiments of Bung [4]. These were performed on four different spillways combining two selections for the angle (θ =18.4, 26.6°) with two for the step height ($s = 0.03, 0.06$ m). For each spillway, measurements were made for three flow discharge values ($q = 0.07, 0.09, 0.11$ m^{2}s^{-1}). The parameters θ, s, and q can be used to construct the step Froude number, which can be considered the main controlling parameter of the flow [18; 5],

$$\mathsf{F_s} = \frac{q}{\sqrt{g\ \sin\theta K^3}}. \tag{5}$$

Here $K = s\cos\theta$ is the step induced macro-roughness and g is the acceleration due to gravity. The experiments of Bung cover twelve different Froude numbers in the range, $2.7 \leq \mathsf{F_s} \leq 13$. For the simulations four values fairly evenly distributed across this range have been selected: 2.7, 4.6, 8.3, and 13.0. The values of θ, s, and q in the four simulation cases are provided in Table 1. This table also provides the values of some auxiliary geometrical parameters, the definition of which can be found in Figure 1. The figure also shows the origin and orientation of the employed Cartesian coordinate system.

Table 1: Setup for the different simulation cases. The number of cells are given in 10^3.

$\mathsf{F_s}$(-)	θ(°)	s(m)	q(m^{2}s^{-1})	L_x(m)	L_s(m)	h_{win}(m)	$n_{cells,G1}$	$n_{cells,G2}$	$n_{cells,G3}$	$n_{cells,G4}$
2.7	26.6	0.06	0.07	5.23	0.134	0.10	89	354	1 414	5 647
4.6	18.4	0.06	0.11	7.41	0.190	0.13	122	482	1 917	7 646
8.3	18.4	0.03	0.07	7.41	0.095	0.10	119	466	1 840	7 317
13.0	18.4	0.03	0.11	7.41	0.095	0.13	119	466	1 840	7 317

All the simulations are performed on 2D domains. This is chiefly motivated by the fact that the investigated modelling methodology is low-fidelity and most suitable for quick evaluations of the integral characteristics of the flow. Any 3D effects due to sidewalls are expected to be negligible with respect to the overall accuracy of the flow predictions. Additionally, using 2D domains it seems to be ensured that, even

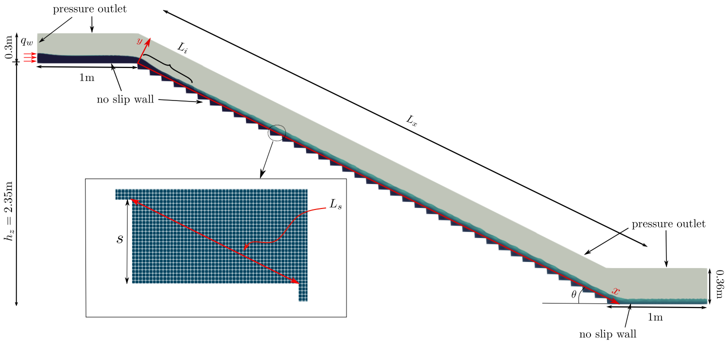

Figure 1: Sketch of the geometry of the simulation case, identifying the geometric parameters, and also the employed boundary conditions.

on dense grids, no air entrainment is resolved by the VoF. This is shown by the `interFoam` computations on grid G4. By contrast, in a 3D setting, it is more likely that some interface perturbations eventually start getting captured. Investigating the performance of the entrainment modelling in such a scenario is of interest, but lies out of scope of the current work.

The same boundary conditions were used for all cases, with the exception of the discharge q prescribed at the water inlet. The height of the inlet was adjusted to ensure sub-critical inflow conditions. A zero gradient condition was used for the pressure, while Dirichlet conditions were applied to k, ϵ, and ω. The values were set assuming 5% turbulent intensity and 10% of the critical height as the turbulent length scale.

For the outlet, a zero gradient condition was prescribed for velocity, pressure, α_l and α_g. For k, ϵ, and ω the OpenFOAM `inletOutlet` boundary condition was applied. It acts as a zero gradient condition in case of outflow, but for backflow a homogeneous Dirichlet condition is applied instead.

No slip conditions were used at the walls, with a zero gradient condition set for α_l and α_g. The turbulent quantities were estimated by regular wall laws, in OpenFOAM named as `kqRWallFunction`, `epsilonWallFunction`, `omegaWallFunction` and `nutkWallFunction`, for k, ϵ, ω, and ν_t respectively.

For the top boundary the total pressure was fixed, and a `pressureInletOutletVelocity` condition was applied for the velocity. Similar to `inletOutlet`, this imposes a zero gradient for outflow, whereas for backflow, it assigns a velocity based on the flux in the patch normal direction. The `inletOutlet` boundary condition was used for α_l, α_g, k, ϵ, and ω.

The material properties of the fluids were set to correspond to air and water. The values are provided in Table 2.

The computational grids were constructed using Pointwise®, and consist of square cells with the exception of a small strip close the top boundary, where unstructured meshing was necessary to account for the slope of the geometry. Four grids with increasing cell density, denoted G1, G2, G3, and G4, were constructed for each of the four spillways. In each consecutive grid the edge length of the square cells is halved. On the coarsest grid G1, the edge length is 5 mm, which corresponds to what was used in the simulations by Lopes et al. [16]. This can be related to the the critical height of the spillway flow, defined as $h_c = \left(q^2/g\right)^{1/3}$.

Table 2: Simulation parameters.

Property	**Value**
Liquid density, ρ_1	1000 kg/m^3
Gas density, ρ_2	1 kg/m^3
Liquid kinematic viscosity, ν_1	$1 \cdot 10^{-6}$ m^2/s
Gas kinematic viscosity, ν_2	$1.48 \cdot 10^{-5}$ m^2/s
Surface tension coefficient, σ	0.07

Depending on the flow case, on the G1 grid, h_c is discretised by either 15 or 21 cells. The numbers for the G4 grid are, respectively, 126 and 171. The densities are not adjusted to remain equal with respect to h_c across all flow conditions, because experiments showed that the relevant parameter for entrainment modelling is the resolution of the interface. The number of cells in each mesh is given in Table 1.

In conclusion, additional characteristic scales of spillway flow are defined. These will be used for non-dimensionalising the results. At a given x, the height h_{90} is defined as the y-coordinate of the point where $\alpha_{air} = 0.9$. The velocity u_{90} is defined as the x-component of the mean velocity vector at $y = h_{90}$. Similar scales can be defined with respect to other α_{air} values, e.g. h_{50}.

4. Air entrainment modelling

This section presents the air entrainment model developed by Lopes et al. [16]. One can split the model into three components: an estimator for the flux of entrained air, a transport equation for the volume fraction of entrained air, and a coupling procedure between the model and the VoF framework. Sections 4.1, 4.2, and 4.3 each focus on one of these components. Additionally, for the stepped spillway, estimating the location of the inception point is necessary and this constitutes an additional component of the model, which is treated in Section 4.4.

4.1. Estimating the flux of entrained air

A key component of the model is the estimation of the quantity of entrained air carried passed some imaginary surface located below the interface. The estimate was proposed by Ma et al. [17]:

$$q = a \cdot \operatorname{Pos}\left(\nabla(u \cdot n) \cdot n\right), \tag{6}$$

where a is a length scale associated with the roughness of the interface due to turbulence,

$$\operatorname{Pos}(x) = \begin{cases} x, & x \geq 0 \\ 0, & x < 0, \end{cases}$$

and n is the interface normal defined as

$$n = \nabla\alpha_l / \left(|\nabla\alpha_l| + \varepsilon\right). \tag{7}$$

Here ε is a small number added for numerical stability.

It is assumed that entrainment is confined to a layer of thickness ϕ_{ent} close to the surface. Therefore, in order to obtain a volumetric air entrainment rate, q can be divided by ϕ_{ent}. Note, however, that (6) is by definition not restricted to being non-zero only in the vicinity of the interface. Theoretically, entrainment can be incorrectly predicted in regions where it should not take place. For this reason, in [16], q is additionally multiplied by some function δ_{fs}, which is non-zero only close to the interface. The final form of the volumetric air entrainment rate estimate is

$$S_g = \frac{a}{\phi_{ent}} \operatorname{Pos}\left(\nabla(u \cdot n) \cdot n\right) \delta_{fs}. \tag{8}$$

It remains to define how a, ϕ_{ent}, and δ_{fs} are computed. The common approach for a is to equate it to the turbulent length scale as predicted by the RANS model. The value of ϕ_{ent} should be related to some characteristic length scale of the problem.

Within the VoF framework, the α_l-field stands out as the natural choice as a basis for the development of an interface indicator function such as δ_{fs}. Typically, the interface is defined as the isosurface $\alpha_l = 0.5$, however this is only accurate when the interface is sharp. In the presence of air entrainment, a more robust metric is the magnitude of the gradient of α, which can be expected to reach its maximum close to the boundary between the continuous air region and the air-water mixture. Hänsch et al. [12] used the gradient of α and a function based on tanh to find the interface as part of their air entrainment model. This function was adopted by Lopes et al. [16] and reads as

$$\delta_{fs} = \frac{1}{2}\tanh\big[\beta\Delta x(|\nabla\alpha_l| - |\nabla\alpha_l|_{cr})\big] + 0.5. \tag{9}$$

Here $|\nabla\alpha_l|_{cr}$ is a constant representing the critical value of the gradient that is expected to be reached in the interface cells. Its estimate can be computed based on the size of the grid cell, Δx: $|\nabla\alpha_l|_{cr} = 1/(4\Delta x)$. The parameter β can be used to control the extent of the interface region with respect to the chosen $|\nabla\alpha_l|_{cr}$, and thus provides an opportunity to broaden or restrict the number of cells in which the source term is active.

4.2. The α_g-equation

The source term (8) is introduced into an additional equation for the modelled volume fraction of entrained air, α_g:

$$\frac{\partial\alpha_g}{\partial t} + \nabla\cdot(u_g\alpha_g) + \nabla\cdot(\nu_t\nabla\alpha_g) = S_g. \tag{10}$$

Here ν_t denotes the turbulent viscosity. The velocity of the entrained air, u_g, is either set to be equal to $\overline{u}$ or alternatively modified according to [7]:

$$u_g = \overline{u} + u_r, \tag{11}$$

where the correction velocity u_r is calculated based on a bubble radius according to

$$u_r = \begin{cases} -4474 r_b^{1.357} g, \quad \text{if} \quad 0 < r_b \leq 7\times10^{-4}\text{m} \\ -0.23g, \quad \text{if} \quad 7\times10^{-4} < r_b \leq 5.1\times10^{-3}\text{m} \\ -4.202 r_b^{0.547} g \text{ if } r_b > 5.1\times10^{-3}\text{m}. \end{cases} \tag{12}$$

The inclusion of the diffusion term in (10) is considered optional.

Additionally, Lopes et al. [16] argue that to properly account for the break-up of bubbles at the free surface, α_g should be set to zero when α_{air} exceeds a certain threshold value, referred to as the BBA. The suggested value to use is 0.1.

The exact physical meaning of α_g and its relation to α_l are somewhat elusive. In [16], the authors discuss the possibility of using the entrainment model without backward coupling to the VoF solver. In this case, the situation is clear: α_g shows the modelled distribution of the volume fraction of entrained air, which cannot be captured by the VoF. However, when the coupling is two-way (particulars presented below), the idea is that the entrained air should be captured in the α_l field, and α_g is essentially reduced to a buffer-field used to propagate the effect of S_g onto α_l.

4.3. Coupling to the VoF solver

Here, we are interested in applying the model in a two-way coupling regime, meaning that the model's predictions should be propagated into the distribution of α_l. The premise is that the VoF simulation by itself does not resolve any entrainment, and therefore all of it is accounted for by a subgrid model based on the α_g equation (10). The overall idea is that α_l should be reduced in regions where α_g is large, and in a manner that does not disrupt mass conservation.

Here this is done through a modification of the artificial compression term introduced into the α_l-equation (3):

$$\nabla \cdot (u^c(1-\alpha_l)\alpha_l)\,. \tag{13}$$

The term $(1-\alpha_l)\alpha_l = \alpha_{air}\alpha_l$ is originally meant to serve as an indicator for cells constituting the interface, in which the compression is to be applied. The key observation is that multiplying u_j^r by some negative number instead would lead to interface expansion and thus a region occupied by a mixture. The goal is then to correlate α_g with the change in sign in the term in front of u_j^r. The most obvious way to do that is exchange $\alpha_{air}\alpha_l$ for $(\alpha_{air}-\alpha_g)\alpha_l$. Note that since (13) is a transport term, mass conservation is guaranteed. The modified α_l-equation then reads

$$\frac{\partial \alpha_l}{\partial t} + \nabla \cdot (\overline{u}\alpha_l) + \nabla \cdot (u^c(\alpha_{air}-\alpha_g)\alpha_l) = 0. \tag{14}$$

Under the definition above, the model is active only when $\alpha_g > \alpha_{air}$, which is reasonable. It is also worth mentioning that otherwise (13) recovers its original compressive function. This occurs even in the regions occupied by a mixture, which can be called into question. As part of the work on improving the model, some experiments have been conducted in which positive values of $\alpha_{air} - \alpha_g$ where cut to 0, however the exhibited results were inaccurate, and introducing such a discontinuity is probably best avoided.

4.4. Inception point estimation

As discussed in the introduction, surface aeration initiates when the turbulence perturbations exceed the stabilizing forces of surface tension and buoyancy at the free surface. In the model of Lopes et al. [16] no attempt is made to explicitly compute the force balance. Instead, two model parameters, k_c and u_c are introduced, where the subscript c stands for critical. The inception is considered to occur when

$$k > k_c \text{ and } u \cdot n > u_c \text{ and } u \cdot g > u_c. \tag{15}$$

Appropriate values for k_c and u_c are extremely difficult to predict a priori, since the selection clearly depends not only on the flow conditions (see Section 5.1), but also on the turbulence model and its prediction of k. Careful calibration with respect to the selected model is therefore necessary. In [16], the authors nevertheless suggest $u_c = 0.8$ m/s and $k_c = 0.2$ m^2/s^2, referring to previous experimental results. Unfortunately, how these values relate to the characteristic length and velocity scales of the flow is not discussed.

5. Stepped spillway simulations with the original model

This section demonstrates results from simulations performed using the model of Lopes et al. [16] described in the previous section. In the original source the model was reported to reproduce experimental data on a stepped spillway with $\mathsf{F_s}$=2.7. However, the simulations were performed on relatively coarse grids, with the grid sensitivity study performed using only the baseline VoF solver. Furthermore, initial testing within this work indicated that its effect was reduced upon grid refinement, which motivates the analyses herein.

The implementation of the corresponding solver, called `airInterFoam` was kindly provided by P. Lopes via personal communication. Below, we abbreviate `airInterFoam` to AIF. In the following sections, the solver is evaluated in terms of sensitivity to flow conditions (Section 5.1), grid resolution (Section 5.2), and several parameters of the entrainment model (Section 5.3).

5.1. Sensitivity to $\mathsf{F_s}$

Here, results from four AIF simulations varying in the prescribed Froude number of the spillway flow are presented. To highlight the effect of the entrainment model, data obtained with the baseline VoF solver `interFoam` (abbreviated IF henceforth) are also provided. The employed numerical parameters are based on [16], where good results for the $\mathsf{F_s}$=2.7 case (simulated in 3D) are presented. In particular, the G1 grid is employed, k-ω SST is used for turbulence modelling, the diffusion term is omitted in the α_g equation, and $k_c = 0.2\ \mathrm{m}^2/\mathrm{s}^2$, $u_c = 0$, $u_g = u_l$, BBA $= 0.1$, and $\phi_{ent} = 0.05h_c$.

Figure 2 shows the obtained values of α_{air} in the uniform flow region. Good accuracy is achieved for $\mathsf{F_s}$=2.7 and 4.6, but for the two higher $\mathsf{F_s}$ the model fails to predict the reduced penetration of air into the corners of the steps. As a result, in terms of magnitude, the errors in the IF and AIF simulations are similar, although in the case of IF the diffusion of the interface is a purely numerical effect. It is also interesting to note that for $\mathsf{F_s}$=2.7 the accuracy is on par with the 3D simulations using similar model settings conducted in [16].

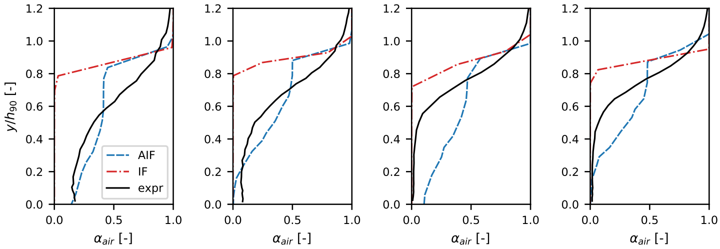

(a) $\mathsf{F_s}$=2.7 (b) $\mathsf{F_s}$=4.6 (c) $\mathsf{F_s}$=8.28 (d) $\mathsf{F_s}$=13

Figure 2: Vertical void fraction profiles for uniform flow conditions. Spillway flows with different Froude numbers at the coarsest grid G1. AIF simualtions compared to IF simulations and experimental results by Bung [4].

The evolution of the surface elevation, measured as h_{90}, is shown in Figure 3. The elevation's value in uniform conditions is well-predicted for all Froude numbers. However, the location of the inception points are not captured as consistently. The difference in the obtained values with respect to the experimental data of Bung is provided in each plot of the figure: Δn_i stands for the difference in terms the step number, and ΔL_i in terms of x. It should be noted that when comparing across different F_s, using ΔL_i is more appropriate, since for the two higher Froude numbers, the length of the step is halved relatively to the lower Froude number cases. The obtained incetion point locations for $\mathsf{F_s}$=2.7 and $\mathsf{F_s}$=4.6 are reasonably accurate, but, unfortunately, at higher $\mathsf{F_s}$ the disagreement with the experiment becomes larger. Furthermore, the predicted inception point for $\mathsf{F_s}$=8.3 is further downstream as compared to that for $\mathsf{F_s}$=13, whereas the experimental data exhibits the opposite trend.

Figure 3 additionally shows the experimental values of h_w, which is the equivalent clear water depth, i.e. the surface elevation that should be predicted by IF. In the obtained results, IF somewhat over-predicts h_w, the reason being the coarseness of the grid.

The predicted profiles of the streamwise velocity are shown in Figure 4. Remarkably, no effect of air entrainment modelling is visible, and accurate profiles can be predicted with IF. This result was reproduced in all the simulations in this paper, and, for that reason, velocity profiles are not further presented or discussed.

The principle conclusion from the obtained results is that the settings used in [16] for the $\mathsf{F_s}$=2.7 case fail to provide consistently accurate results as the Froude number becomes larger. This indicates that some parameter values of the model, for example k_c, should be made a function of $\mathsf{F_s}$.

5.2. Grid sensitivity

To explore the grid sensitivity of AIF, the $\mathsf{F_s}$=2.7-case was run on all four grids G1-G4. The resulting α_{air} and h_{90} profiles are shown in Figure 5. Clearly, the behaviour obtained on the coarse grid G1 is substantially changed as the grid gets denser. With increasing resolution, less air is distributed towards the

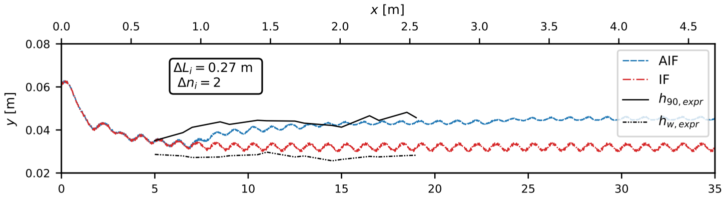

(a) $\mathsf{F_s}$=2.7

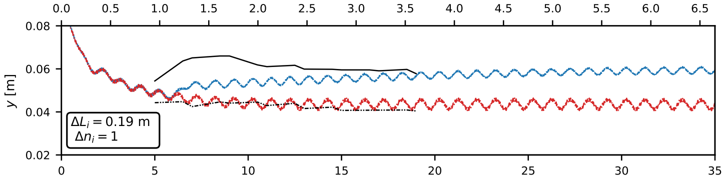

(b) $\mathsf{F_s}$=4.6

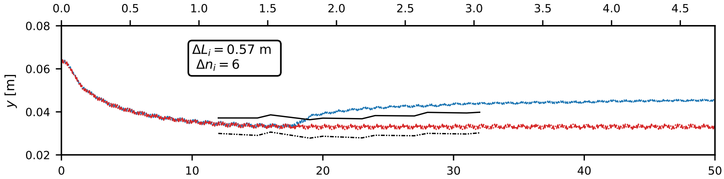

(c) $\mathsf{F_s}$=8.28

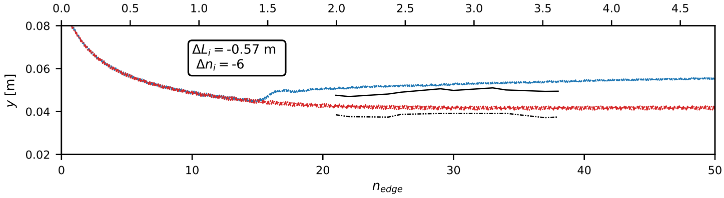

(d) $\mathsf{F_s}$=13

Figure 3: Surface elevation plots, h_{90}. Spillway flows with different Froude numbers simulated by AIF on the coarsest grid G1, compared to IF simulations and physical model results by Bung [4]. The difference from the experimentally measured inception point is annotated in meters (ΔL_i) and in steps (Δn_i).

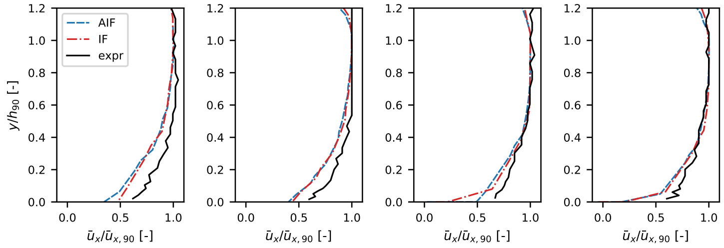

(a) $\mathsf{F_s}$=2.7 (b) $\mathsf{F_s}$=4.6 (c) $\mathsf{F_s}$=8.28 (d) $\mathsf{F_s}$=13

Figure 4: Vertical profiles for the streamwise velocity for uniform flow conditions. AIF and IF simulation results compared to experimental results by Bung [4].

pseudo-bottom, and for the densest grid only a tiny air layer is found close to the surface. The profiles, both h_{90} and α_{air}, approach the corresponding solutions obtained with IF. Obviously, this is caused by the fact that less numerical diffusion contribute to the transport of α_g as the grid is refined, but inspection shows that this is also caused by the shrinkage of the area in which the source term S_g is non-zero. This, in turn, is controlled by δ_{fs}, which makes the definition of this function a contributor to the grid sensitivity. A more elaborate discussion follows in Section 6. On the other hand, with respect to h_w, the IF solution consistently improves with grid refinement. On the G4 grid the interface is perfectly sharp and the h_w profile is very well-matched.

5.3. Sensitivity to u_r, bubble breakup criterion, and α_g-diffusion

Here we explore the effects of the entrainment model parameters that could arguably be considered non-essential or optional. First, the impact of the air bubble drift velocity model, as given in eq. (12), is investigated. This is followed by an analysis of the bubble breakup criteria, BBA. Finally, the model is tested in terms of activation of the diffusion term in the α_g-equation (10). The rest of the numerical setup is similar to that used in the Froude number sensitivity study, see Section 5.1.

Here we restrict the analysis to α_{air} profiles in the uniform flow region. For the u_r model, three values of the bubble radius r_b are considered, along with setting u_r to 0. The result is shown in Figure 6a. Clearly, including u_r leads to reduced air entrainment, and this effect becomes larger when the input bubble radius is increased. This is expected, since u_r is, by definition, directed upwards. Since the intensity of air entrainment is already heavily dependent on the formulation of δ_{fs}, having an additional controller in terms of u_r introduces unnecessary complication. At least in the case of spillway flow, setting $u_r = 0$ can therefore be recommended.

Three values of the BBA are considered. The first is 0.1, which is recommended by Lopes et al. [16], and the other two are 0.05 and 0. Recall that the chosen value refers to the minimal volume fraction of water for which α_g is allowed to be non-zero. The results from the three simulations are shown in Figure 6b. As expected, slightly more air is entrained close to the h_{90} when the bba value is reduced. Note that compared to the experimental data, the air fractions predicted by AIF close to the interface (from $y/h_{90} \approx 0.8$) are too low. Thus, deactivating the BBA-criterion produces a small improvement in the accuracy meaning that this parameter can be safely removed from the formulation of the model.

Finally, the effect of the diffusion term in (10) is investigated. Two simulations, with and without the diffusion term included, have been conducted, see Figure 6c. The effect of the diffusion appears to be completely negligible. Consequently, it is possible to remove it from the model.

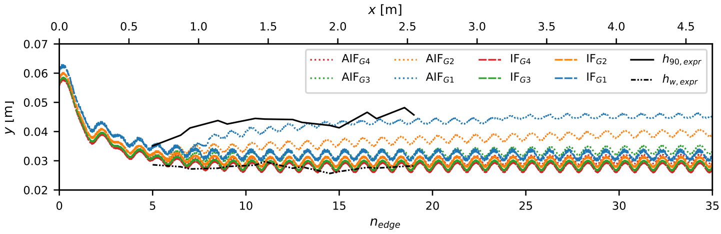

(a) Surface elevation plot, h_{90}-surface.

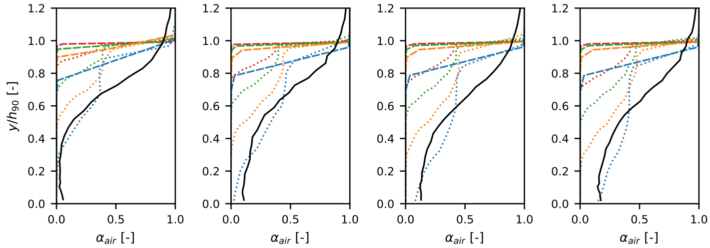

(b) Step 7 (c) Step 11 (d) Step 15 (e) Step 19

Figure 5: AIF simulations for F_s=2.7 at different grids (G1-G4) compared to physical model results by Bung [4]. Figure 5a shows the surface elevation, Figures 5b-5e void fraction profiles for different steps.

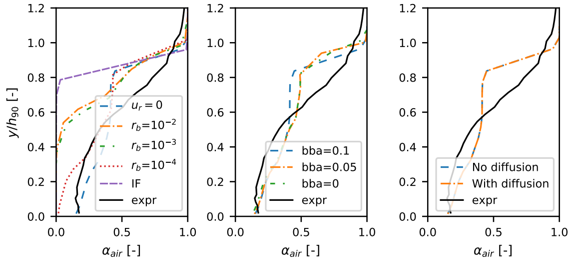

(a) (b) (c)

Figure 6: Sensitivity of α_{air} profiles to the slip velocity model, bubble breakup criterion, and α_g-diffusion.

In summary, u_r, BBA, and α_g-diffusion can be excluded from the model, significantly simplifying its formulation.

5.4. Sensitivity to β

As shown in Section 5.2, at high grid resolutions the effects of the model becomes negligible, or even deactivated. The most important controller of the breadth of the region (in terms of $\nabla\alpha_l$) where entrainment is introduced is the form of δ_{fs}, see Eq. (9). In particular, the parameter β determines the breadth of the tanh function, meaning that with smaller β the region of the model activation becomes larger. In principle, it may thus be possible to maintain an appropriate level of entrainment at high grid resolutions by adjusting β accordingly. However, for this to be possible in practice, the necessary change to β should be easy to predict a priori.

Multiple simulations across different Froude numbers and grid resolutions have been conducted in an attempt to determine whether clear guidelines for setting β could be established. Unfortunately, these efforts were fruitless, and the results of using a given β value change significantly depending on the flow and parameters of the simulation.

As an illustrative example, Figure 7 shows the α_{air} profiles produced using $\beta = 10$ and 25 in simulations at different Froude numbers on the G2 grid, and compares it to the corresponding profile produced by AIF, where a β-value of 100 is used as default. For $\mathsf{F_s}$=2.7 the sensitivity to β is rather small, but for $\mathsf{F_s}$=4.6 a significant increase in aeration occurs. For larger Froude numbers a lower β mainly leads to more air being present in the corner of the steps. While the change in the α_{air} profiles appears to be rather small, uniform flow conditions are not reached, and its effect continues to grow further downstream. Similar sporadic behaviour was observed with respect to other simulation parameters. For example, contrary to what is observed when using the G2 grid, using G3 instead leads to the $\mathsf{F_s}$=2.7 case becoming very sensitive β.

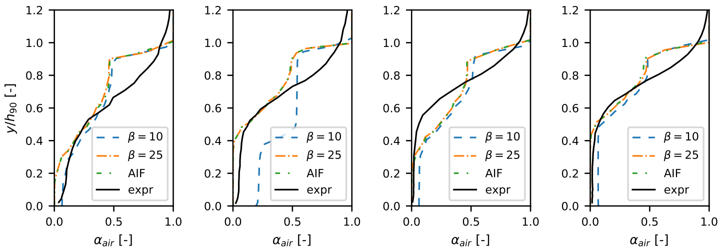

(a) $\mathsf{F_s}$=2.7 (b) $\mathsf{F_s}$=4.6 (c) $\mathsf{F_s}$=8.28 (d) $\mathsf{F_s}$=13

Figure 7: Sensitivity on β for AIF evaluated on grid G2 for different step Froude numbers. Vertical α_{air} profiles are shown. The data is extracted from what should be the start of the uniform flow region according to the experimental data [4].

6. Proposed model developments

In the previous sections, two issues with the entrainment model proposed by Lopes et al. [16] have been identified. Perhaps the most critical one is the successive deactivation of the model upon grid refinement. The other one is the difficulty in prescribing the k_c value in order to get a good prediction of the inception point. In this section, improvements to the model are proposed aiming at alleviating these problems. First, an alternative formulation for the δ_{fs} function is introduced in Section 6.1. Afterwards, amplification of the diffusion term in the α_g is argued for in Section 6.2. Finally, a different way of predicting the inception point is discussed in Section 6.3.

6.1. *Free surface detection*

Before discussing the formulation of δ_{fs}, it is necessary to consider what kind of restriction of S_g in space is needed in the case of spillway flow. A typical distribution of an unrestricted S_g is shown in the left plot of Figure 8. The first thick yellow line is located right below the interface and represents the region where the entrainment can be expected to take place. However, a discontinuous strip of non-zero values is also observed close to the psuedobottom along with more or less randomly distributed points of activation in the corners of the steps. Physically, no entrainment can occur in these regions, and the δ_{fs} function should filter them out. Note that the spatial separation between the correct and non-physical regions of source term activation is not large, which explains why defining δ_{fs} in a universal way that fits all flow conditions and numerical settings is not trivial.

To arrive to a better formulation for δ_{fs}, it is important to clearly understand the deficiencies of the original definition, see Eq. (9). With $\nabla\alpha_{l,cr}$ set to $1/(4\Delta x)$, the distribution of δ_{fs} over $\nabla\alpha_l$ depends on two quantities: β and Δx. It is instructive to see how δ_{fs} changes shape when the values of these parameters are changed. In the left plot of Figure 9, $\delta_{fs}(\nabla\alpha_l)$ is shown for Δx values corresponding to grids G1-G3, and the two values of β considered in the sensitivity study in Section 5.4. The tanh function defining the transition region of δ_{fs} from 0 to 1 is centred at $\nabla\alpha_{l,cr}$, shown in the figure with black vertical lines. As the grid is refined, this location is shifted to the right, and for larger values of β, the tanh only spans a limited range of high $\nabla\alpha_l$ values. On the other hand, for smaller β, the tanh becomes so wide that δ_{fs} remains non-zero everywhere.

This behaviour of δ_{fs} should be related to how $\nabla\alpha_l$ is typically distributed across y, see the right plot in Figure 8. Note that the high values of $\nabla\alpha_l$ are always restricted to to a relatively thin region close to the interface. Consequently, for a large β, for example $\beta = 100$ as proposed in [16], δ_{fs} will be restricted to an increasingly smaller region in space when the grid gets refined. This explains why the diminishing effect of the entrainment with grid refinement observed in Section 5.2.

As mentioned above, it is easy to make the δ_{fs} function less restrictive by lowering β. However, the issue here is that the β and the effective cut-off value in terms of $\nabla\alpha_l$ are not intuitively related. This is problematic given that the margin of error is quite small, as discussed above in relation to the typical distribution of S_g.

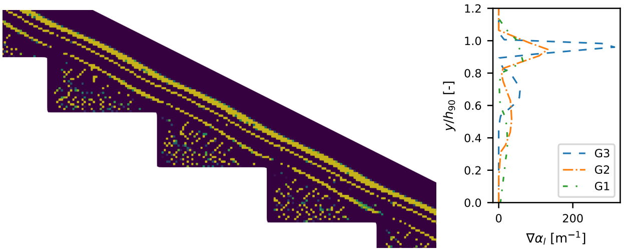

Figure 8: Left: Typical distribution pattern of an unrestricted S_g. Right: Typical profiles of the gradient of α_l.

Alternative options for the expression of δ_{fs} were explored, including a parabola based function, and a step-shaped function defined purely based on the distance from a defined interface. For both alternatives, the idea was to set the value of the critical gradient of α_l relatively tight, to capture the upper peak in the gradient plot in Figure 8, and then expand its prevalence away from the these locations according to an appropriate function or logic. In the distance based alternative, δ_{fs} was set to 0 or 1 for a particular cell, depending on its distance from the defined interface. If this distance was less then the interface thickness, ϕ_{ent}, δ_{fs} was set to 1, and otherwise its value was set to 0. However, this led to step-shaped profiles of α_l,

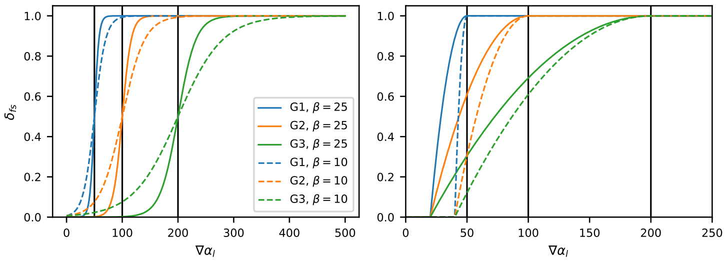

Figure 9: Surface indicator functions δ_{fs}.

where too much air was entrained below the interface, and indicated a need to apply some functionality to reduce the effects of the source term as the gradient of α_l is reduced below its critical value.

Acknowledging the above, a parabola based function was considered. The possibility to define $\nabla\alpha_{cr}$ as a top point of the function, and to define a cut-off value for the gradient as an intersection point, was viewed as beneficial features of this function in the current setting. The latter leading to the possibility of avoiding the long tail in the tanh-function, with the corresponding uncontrollable potential for generation of none-zero values of S_g within the steps. The parabola-based δ_{fs} formulation is proposed as

$$\delta_{fs}(\nabla\alpha_l) = \begin{cases} \mathrm{Pos}\left(-\frac{1}{4d}\left(|\nabla\alpha_l| - |\nabla\alpha_{l,cr}|\right)^2 + 1\right) & \text{if } \nabla\alpha_l < |\nabla\alpha_{l,cr}| \\ 1 & \text{otherwise.} \end{cases} \tag{16}$$

Here, d refers to the distance from the vertex of the parabola to its focus, which can be computed as

$$d = 0.25\left(|\nabla\alpha_{l,cr}| - |\nabla\alpha_{l,cut}|\right)^2,$$

where $\nabla\alpha_{l,cut}$ is an input parameter explicitly defining the lowest $\nabla\alpha_l$ for which the source term may assume non-zero values. The proposed δ_{fs}, computed for grids G1-G3 and two different values of $\nabla\alpha_{l,cut}$, is shown in the right plot of Figure 9. The non-zero values of the function are always fixed to the interval $[\nabla\alpha_{l,cut}, \nabla\alpha_{l,cr}]$, which expands upon grid refinement. Unfortunately, due to this expansion, even with this new δ_{fs}, the region of non-zero S_g values shrinks as the grid is refined. However, the process is slowed, since δ_{fs} is left to be non-zero at lower $\nabla\alpha_l$.

During initial testing, it was observed that the parabola-based δ_{fs} was very effective at filtering out the sporadic source term activation in the corner of the steps, while preserving the region where entrainment is expected. However, the secondary strip of non-zero S_g values close to the psuedobottom (see left plot in Figure 8) would sometimes still be left unfiltered. This is likely related to the secondary peak in $\nabla\alpha_l$. To rectify this, the parabolic surface indicator function in Eq. (16) is combined with a distance based approach like the one outlined above.

In details, the values of δ_{fs} computed according to Eq. 16 are additionally manipulated as follows. First, the cells in which $\delta_{fs} \geq 0.9$ are selected. These should lie near the interface and are therefore likely to belong to the region where S_g should be activated. For the remaining cells, the distance to the nearest cells with $\delta_{fs} \geq 0.9$ is computed. If this distance exceeds the interface thickness, ϕ_{ent}, the value of δ_{fs} in the cell is set to 0. Overall, this combined formulation gave improvements compared to the original formulation based on tanh. It is noted that even without the distance cut-off modification, improved results with the parabolic δ_{fs} could be achieved, and the $\delta_{fs} \geq 0.9$ criterion can give false positives.

Finally, making both $\nabla\alpha_{l,cr}$ and $\nabla\alpha_{l,cut}$ grid independent parameters has briefly been tested, but abandoned due to the sensitivity of the results to the chosen values. In general, our extensive efforts and experimenting with δ_{fs} formulations and other simulation settings showed that constructing a robust and accurate δ_{fs} is very challenging. The sensitivity of the results to any changes in the simulation parameters or flow conditions tends to be very strong. Nevertheless, as shown in the Section 7, the proposed δ_{fs} does represent an improvement with respect to prior art.

6.2. Modelling air propagation into the corners of the steps

By definition, the employed entrainment model is meant to account for aeration occurring close to the free surface, within some layer of thickness ϕ_{ent}. However, experimental results clearly show that in the case of the stepped spillway, air penetrates all the way down to the surface of the steps, see e.g. the experimental profiles in Figure 2. The physical mechanism through which this occurs is described by Pfister and Hager [22]. Inspection of video recordings from their experiments reveals the occasional generation of air troughs that extend from the surface into the bulk flow. These troughs penetrate deep enough to hit the step edges, and when they do, the air is distributed into the steps.

Capturing this intrinsically transient process in a steady state model is not straightforward. Here, we consider using a somewhat ad-hoc approach, taking advantage of the diffusion term in the α_g equation (10), $\nabla \cdot (\nu_t \nabla \alpha_g)$. Recall that in Section 5.3 it was shown that the effect of this term on the solution is essentially negligible. However, the effect can be easily amplified by pre-multiplying it with some constant C_t. The increased diffusion of α_g will then lead to air being redistributed more evenly across y, and consequently result in stronger aeration closer to the pseudobottom.

The difficulty lies in the choice of the value of C_t since there is no clear physical analogy between the modelled phenomenon and diffusion. In light of this, it was attempted to search for a suitable value through experimentation, to see whether one leading to improved results across all the considered Froude numbers could be found. As a result, $C_t = 150$ was selected.

6.3. Inception point prediction

Even if AIF predicts the aeration onset correctly when appropriate values for k_c and u_c are supplied, the inception point estimation using this method completely depends on user input. As shown in Section 5.1, the appropriate critical value k_c depends on the flow conditions. An alternative approach, found in the work of Hirt [13], is to directly consider the balance between the energy of turbulent motion and that of gravity and surface tension. Defining

$$P_t = \rho k, \tag{17}$$

$$P_d = \rho |g| a + \frac{\sigma}{a}, \tag{18}$$

the source term S_g is activated only in cells where $P_t > P_d$. This way the inception point prediction requires no user input. However, it completely relies on the correct prediction of k and a by the turbulence model.

7. Simulations with the improved model

This section is dedicated to evaluating the effects of the model improvements proposed above. To that end, a new solver incorporating these changes has been implemented. Reflecting the focus on stepped spillway simulations, the solver is called `spillwayFlow` [2], which is abbreviated to SPF below. The robustness of the model with respect to grid resolution is evaluated in Section 7.1. Results from application of the model to spillway flow at all four considered Froude numbers are presented Section 7.2. The proposed criterion for inception point location is tested separately, in Section 7.3.

---

[2] https://github.com/siljekre/spillwayFlow

7.1. Grid sensitivity

Here the new model is put to the same grid sensitivity analysis as presented in Section 5.2 for AIF. To simplify the analysis, the new inception point prediction approach is not employed, and the original criterion based on k_c is used instead. Simulation results for the $\mathsf{F_s}$=2.7 case obtained on grids G1-G4 are shown in Figure 10. Here, $C_t = 0$ and the diffusion term in the α_g equation is thus inactive. As anticipated, the results still depend on the grid, and the general trend is convergence towards the IF solution. Note that in the α_{air} profiles, the reduction of aeration manifests itself predominately at $y/h_{90} \lessapprox 0.6$. Closer to h_{90} results remain acceptable even on the G4 grid. Related to the absence of air in the lower parts, the predictions of h_{90} itself are more sensitive, and unfortunately on the finer grids the accuracy is poor. Nevertheless, compared to the original AIF results (see Figure 5) the robustness of the model is improved.

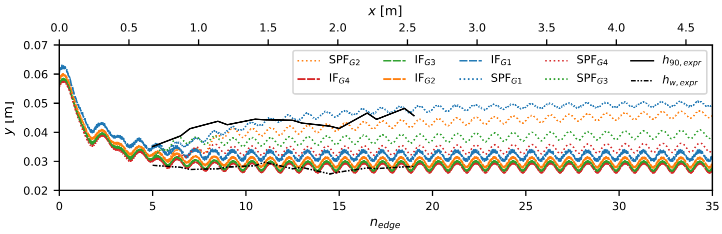

(a) Surface elevation plot, h_{90}-surface.

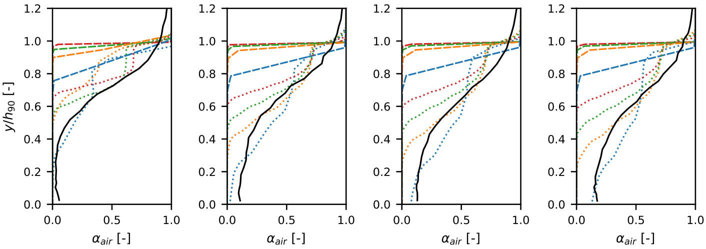

(b) Step 7 (c) Step 11 (d) Step 15 (e) Step 19

Figure 10: SPF simulated with no α_g-diffusion ($C_t = 0$) and $\mathsf{F_s}$=2.7 at different grids (G1-G4) compared to physical model results by Bung [4]. Figure 10a shows the surface elevation, Figures 10b-10e, the void fraction profiles at different steps.

Figure 11 shows the results obtained with $C_t = 150$. As expected, a comparatively more even distribution of α_{air} across y is achieved, in particular for the simulations on denser grids. Furthermore, a very clear improvement in the robustness of the model is evident, with much more similar results obtained on all four grids.

7.2. Results for different Froude numbers

Now, the results obtained with the new model are presented for all four considered values of the Froude number. The simulations were run on the densest mesh, G4. As in the section above, the new criterion for locating the inception point is not used here, and instead k_c is adjusted for each case in order to match the

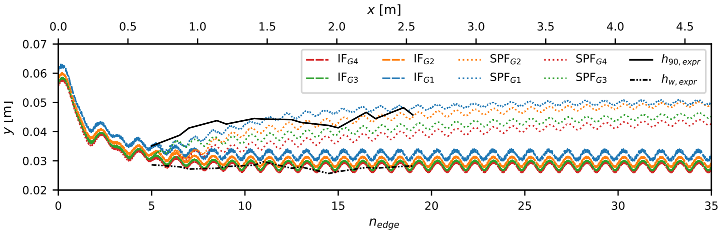

(a) Surface elevation plot, h_{90}-surface.

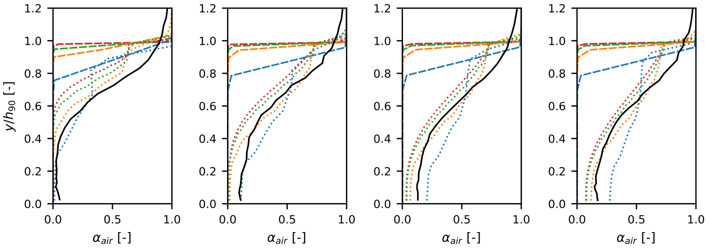

(b) Step 7 (c) Step 11 (d) Step 15 (e) Step 19

Figure 11: SPF simulated with α_g-diffusion ($C_t = 150$) and $\mathsf{F_s}$=2.7 at different grids (G1-G4) compared to physical model results by Bung [4]. Figure 11a shows the surface elevation, Figures 11b-11e, the void fraction profiles at different steps in the developing region.

location in the experimental data. For completeness, profiles corresponding to both $C_t = 0$ and $C_t = 150$ are shown in all the figures. For comparison, they also include results from AIF simulations on the G1 grid, and also from IF simulations on the G4 grid.

The α_{air} profiles are discussed first, see Figure 12. Qualitatively, the same behaviour with respect to C_t is observed for all $\mathsf{F_s}$. With $C_t = 0$ the distribution of α_{air} across y is close to step-wise, with decent agreement with experimental data for $y/h_{90} \gtrapprox 0.7$. When $C_t = 150$, the profiles are smoothed out, which generally increases the accuracy. The exception is the $\mathsf{F_s}$=8.28 case, for which the air volume fraction at low y/h_{90} becomes excessive. Yet even for this case the agreement is better than what could be achieved with AIF.

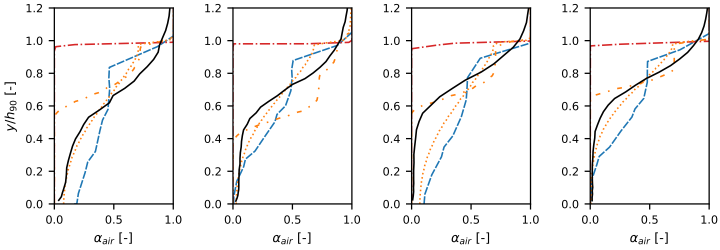

(a) $\mathsf{F_s}$=2.7 (b) $\mathsf{F_s}$=4.6 (c) $\mathsf{F_s}$=8.28 (d) $\mathsf{F_s}$=13

Figure 12: Vertical void fraction profiles for uniform flow conditions. Spillway flows at different Froude numbers. SPF simualtions (G4) compared to IF (G4), AIF (G1) and experimental results by Bung [4]. All plots are showing profiles at step edges.

The surface elevation plots are shown in Figure 13. Overall, $C_t = 150$ leads to better results, which agree well with the experimental data in the uniform flow region. An interesting exception is the $\mathsf{F_s}$=4.6, for which C_t barely has influence on h_{90} in the uniform flow region, whereas in the developing region $C_t = 0$ leads to very good agreement with the experiment. However, it is unlikely that this is explained by any fundamental property of the flow or the model. Compared to AIF, the accuracy of the new model is generally on par. AIF curves are marginally closer to experimental data for the two lower $\mathsf{F_s}$, and the other way around for the two higher $\mathsf{F_s}$.

7.3. Inception point analysis

In this section, the source term activation criterion presented in Section 6.3 is tested. Recall that the inception point location is determined from the flow, and depends heavily on the employed turbulence model. Here we show results from simulations using four models: the k-ω SST and realisable k-ϵ from the standard OpenFOAM library, and their respective counterparts in the library by Fan and Anglart [11], in which the density gradient is properly accounted for in the transport equations. The latter are referred to by adding `varRho` to the name of the model. Simulations using standard turbulence modelling and the k_c-criteria purposed by Lopes et al. [16] are added as reference. The simulations are performed on the G3 grid.

The results are summarized in Table 3, and the corresponding distributions of α_{air} are shown in Figure 14. For the two models from the standard library, the inception of entrainment is triggered immediately (downstream the crest) for all the considered Froude numbers. When the `varRho` variants are employed instead, the inception point shifts downstream. This reflects the fact that these model predict significantly lower values of k. For k-ω SST the agreement with experimental data is nevertheless poor, but for the realisable k-ϵ model the results are more promising.

In the results produced using standard turbulence and $k_c = 0.2$ m^2/s^2, the inception point is predicted in relatively good agreement with the experimental results for all cases but the $\mathsf{F_s}$=13 case, where the

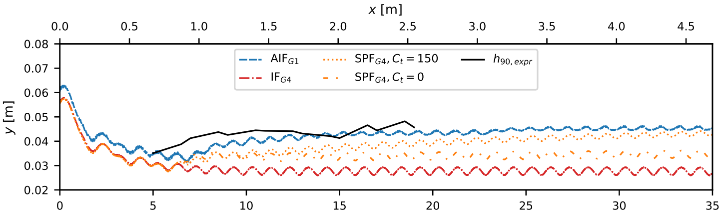

(a) F_s=2.7

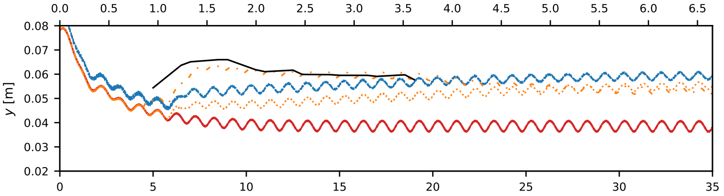

(b) F_s=4.6

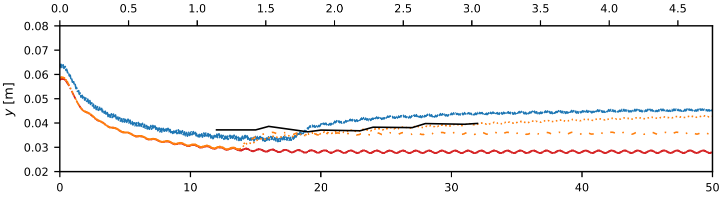

(c) F_s=8.28

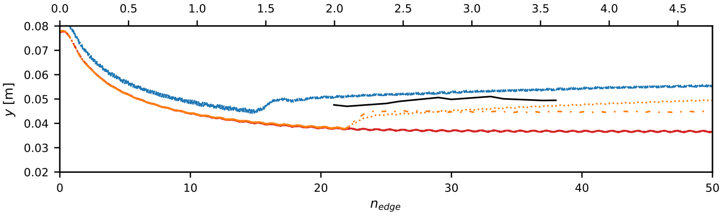

(d) F_s=13

Figure 13: Surface elevation plots, h_{90}. Spillway flows at different Froude numbers. SPF simualtions (G4) compared to IF (G4), AIF (G1) and experimental results by Bung [4].

correspondence is rather bad. This differs from the results attained for AIF at the G1 grid (see Section 5.1), where the inception points were poorly predicted for both $\mathsf{F_s}$=8.3 and $\mathsf{F_s}$=13. Compared to the k_c = 0.2 $\mathrm{m}^2/\mathrm{s}^2$ criterion, the automatic activation criterion performs on par using the realisable k-ϵ turbulence model and the variable density turbulence framework.

Overall, none of the tested models perform well enough to use the proposed source term activation criterion. The improved performance of the `varRho` models shows the importance of properly accounting for the density gradient in the transport equations for the modelled flow quantities. Improving turbulence modelling accuracy near interfaces is an active area of research. The results presented here warrant a deeper investigation of what models are appropriate for the stepped-spillway flow.

Table 3: Inception points found using the source term activation criteria given in Eq. (17)-(18) for SPF simulations on grid G3 using different models for turbulence modelling, compared to physical model results by Bung [4].

$\mathsf{F_s}$	Grid	Turbulence	$L_{i,sim}$	$L_{i,expr}$	ΔL_i	Δn_i
2.7	G3	k-ω SST, $k_c = 0.2$	0.60	0.67	-0.07	-0.5
2.7	G3	realisable k-ϵ, $k_c = 0.2$	0.60	0.67	-0.07	-0.5
2.7	G3	k-ω SST	0.00	0.67	-0.67	-5.0
2.7	G3	realisable k-ϵ	0.00	0.67	-0.67	-5.0
2.7	G3	`varRho`/k-ω SST	1.34	0.67	0.67	5.0
2.7	G3	`varRho`/realisable k-ϵ	1.10	0.67	0.43	3.5
4.6	G3	k-ω SST, $k_c = 0.2$	0.57	0.95	-0.38	-2.0
4.6	G3	realisable k-ϵ, $k_c = 0.2$	0.67	0.95	-0.28	-1.5
4.6	G3	k-ω SST	0.00	0.95	-0.95	-5.0
4.6	G3	realisable k-ϵ	0.00	0.95	-0.95	-5.0
4.6	G3	`varRho`/k-ω SST	2.00	0.95	1.05	5.5
4.6	G3	`varRho`/realisable k-ϵ	1.70	0.95	0.75	4.0
8.3	G3	k-ω SST, $k_c = 0.2$	1.05	1.14	-0.09	-0.9
8.3	G3	realisable k-ϵ, $k_c = 0.2$	0.86	1.14	-0.28	-2.9
8.3	G3	k-ω SST	0.00	1.14	-1.14	-12.0
8.3	G3	realisable k-ϵ	0.00	1.14	-1.14	-12.0
8.3	G3	`varRho`/k-ω SST	1.70	1.14	0.56	-5.9
8.3	G3	`varRho`/realisable k-ϵ	1.43	1.14	0.29	3.1
13	G3	k-ω SST, $k_c = 0.2$	0.76	2.00	-1.24	-13.0
13	G3	realisable k-ϵ, $k_c = 0.2$	0.86	2.00	-1.14	-12.0
13	G3	k-ω SST	0.00	2.00	-2.00	-21.0
13	G3	realisable k-ϵ	0.00	2.00	-2.00	-21.0
13	G3	`varRho`/k-ω SST	2.28	2.00	0.28	2.9
13	G3	`varRho`/realisable k-ϵ	1.90	2.00	-0.10	-1.1

8. Conclusions

This study presents developments in numerical modelling of self-aeration in stepped spillways. The model of Lopes et al. [16] is taken as baseline, and a large simulation campaign is conducted in order to explore its properties: robustness with respect to flow conditions, grid resolution, as well as sensitivity to the model parameters. The simulations were performed for spillway geometries and inflow discharge values used in the experiments of Bung [4], and cover four step Froude numbers in the range from 2.7 to 13. The corresponding experimental data was used as reference.

The results showed that for the case of spillway flows, three of the model parameters could be removed without loss of generality, making simulation setup easier. The main weakness of the model is shown to be its significant sensitivity to the density of the grid. In particular, with increased resolution, the effect of

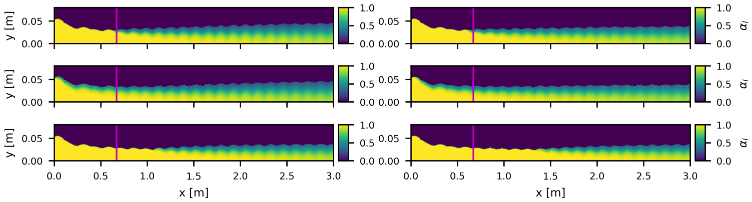

(a) $\mathsf{F_s}$=2.7 – realisable k-ϵ

(b) $\mathsf{F_s}$=2.7 – k-ω SST

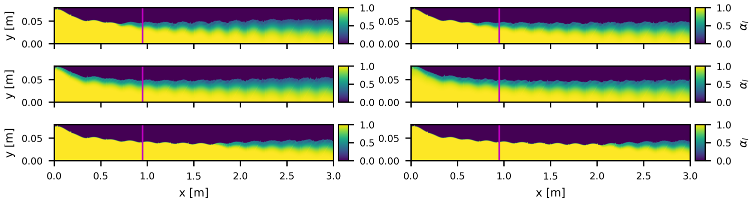

(c) $\mathsf{F_s}$=4.6 – realisable k-ϵ

(d) $\mathsf{F_s}$=4.6 – k-ω SST

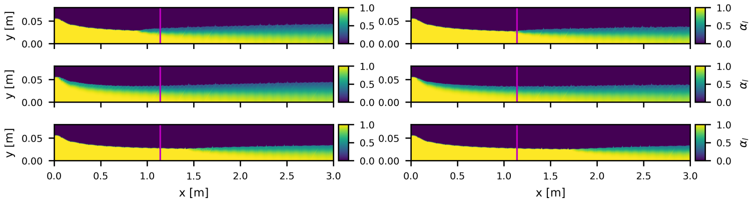

(e) $\mathsf{F_s}$=8.3 – realisable k-ϵ

(f) $\mathsf{F_s}$=8.3 – k-ω SST

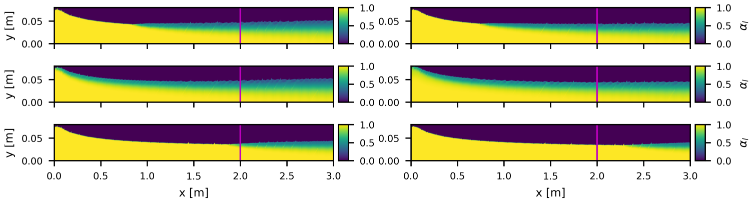

(g) $\mathsf{F_s}$=13 – realisable k-ϵ

(h) $\mathsf{F_s}$=13 – k-ω SST

Figure 14: α_l-fields (starting at the psuedo-bottom) illustrating the inception point locations predicted using Eq. (17)-(18) for the different $\mathsf{F_s}$ cases on grid G3. The middle sub-figures show simulations using standard turbulence modelling, whilst in the lower sub-figures the variable density formulation is used. The top sub-figures refers to results using standard turbulence modelling and $k_c = 0.2$ m^2/s^2, as suggested in [16]. The vertical lines indicate the experimental inception points.

the model diminishes until it is, essentially, no longer active. Nevertheless, at selected grid resolutions, the demonstrated accuracy of the model was acceptable for all considered step Froude numbers. Interestingly, the prediction of the mean velocity profiles was shown to not be affected by air entrainement modelling, and good results could be achieved using only the underlying VoF solver.

The main reason behind the model's deactivation on dense grids has been identified to be the form of δ_{fs}, which is the function used for limiting the activation region of the volumetric air entrainment source term, see Eq. (9).The region of non-zero values of δ_{fs} shrinks as the grid gets refined, and, in the limit, the source term is set to zero in the whole domain, regardless of flow conditions. To address this issue, a new formulation for δ_{fs} is proposed, combining a parabolic profile with distance-based cut-off. Simulations reveal that while fundamentally the results still depend on the grid resolution in the same manner, under the new definition of δ_{fs} the robustness of the model is improved.

As an additional modification, amplifying the diffusion term in the α_g-equation (10) is proposed in order to account for the propagation of entrained air into corners of the steps. Results reveal that this leads to a significant improvement in predictive accuracy, the new model performing better than the original [16] across the whole considered range of $\mathsf{F_s}$ numbers. Furthermore, the robustness of the model with respect to grid resolution improves significantly as well. It should be acknowledged that the selection of the value of the diffusion coefficient, $C_t = 150$, is currently not physically motivated and can, therefore, be called into question. Nevertheless, we believe that the possibility to use the same value across different flow conditions and the clearly demonstrated advantages in terms of the performance of the model are sufficiently strong arguments in favour of adopting the proposed modification. Finding a more rigorous connection between C_t and the characteristic scales of the flow remains as a line of future work.

Finally, an algorithm for automatic estimation of the inception point is tested. The criterion for the inception point is based on energy balance, as proposed by [13]. The performance of the algorithm are heavily dependant on the underlying turbulence model. Unfortunately, for the four considered models the predictions were not reliable, highlighting the need for a more careful investigation of what turbulence modelling is appropriate for self-aerating multiphase flows.

Acknowledgments

This work was supported by grant number P38284-2 from the Swedish Energy Agency. The simulations were performed on resources provided by Chalmers Centre for Computational Science and Engineering (C3SE), the NTNU IDUN/EPIC computing cluster, and UNINETT Sigma2 – the National Infrastructure for High Performance Computing and Data Storage in Norway. The authors are thankful to Daniel Bung for sharing the data files from his physical experiments and to Pedro Lopes for sharing the source code of the `airInterFoam` solver.

References

[1] Boes, R.M., Hager, W.H., 2003a. Hydraulic design of stepped spillways. Journal of Hydraulic Engineering 129, 671–679. URL: https://doi.org/10.1061/(asce)0733-9429(2003)129:9(671), doi:10.1061/(asce)0733-9429(2003)129:9(671).

[2] Boes, R.M., Hager, W.H., 2003b. Two-phase flow characteristics of stepped spillways. Journal of Hydraulic Engineering 129, 661–670. URL: https://doi.org/10.1061/(asce)0733-9429(2003)129:9(661), doi:10.1061/(asce)0733-9429(2003)129:9(661).

[3] Brackbill, J., Kothe, D., Zemach, C., 1992. A continuum method for modeling surface tension. Journal of Computational Physics 100, 335 – 354. URL: http://www.sciencedirect.com/science/article/pii/002199919290240Y, doi:http://dx.doi.org/10.1016/0021-9991(92)90240-Y.

[4] Bung, D.B., 2011. Developing flow in skimming flow regime on embankment stepped spillways. Journal of Hydraulic Research 49, 639–648. URL: https://doi.org/10.1080/00221686.2011.584372, doi:10.1080/00221686.2011.584372.

[5] Chanson, H., 1993. Stepped spillway flows and air entrainment. Canadian journal of civil engineering 20, 422–435. URL: https://doi.org/10.1139/l93-057, doi:10.1139/l93-057.

[6] Cheng, X., Gulliver, J., Zhu, D., 2014. Application of displacement height and surface roughness length to determination boundary layer development length over stepped spillway. Water 6, 3888–3912. URL: https://doi.org/10.3390/w6123888, doi:10.3390/w6123888.

[7] Clift, R., Grace, J., Weber, M., Weber, M., 1978. Bubbles, Drops, and Particles. Academic Press.

[8] Damián, S.M., 2013. An extended mixture model for the simultaneous treatment of short and long scale interfaces. Ph.D. thesis. National University of the Littoral.

[9] Dong, Wang, Vetsch, Boes, Tan, 2019. Numerical simulation of air–water two-phase flow on stepped spillways behind X-shaped flaring gate piers under very high unit discharge. Water 11, 1956. URL: https://doi.org/10.3390/w11101956, doi:10.3390/w11101956.

[10] Ervine, D., Falvey, H., 1987. Behaviour of turbulent water jets in the atmosphere and in plunge pools. Proceedings of the Institution of Civil Engineers 83, 295–314. URL: https://doi.org/10.1680/iicep.1987.353, doi:10.1680/iicep.1987.353.

[11] Fan, W., Anglart, H., 2020. varRhoTurbVOF: A new set of volume of fluid solvers for turbulent isothermal multiphase flows in OpenFOAM. Computer Physics Communications 247, 106876. URL: https://doi.org/10.1016/j.cpc.2019.106876, doi:10.1016/j.cpc.2019.106876.

[12] Hänsch, S., Lucas, D., Krepper, E., Höhne, T., 2012. A multi-field two-fluid concept for transitions between different scales of interfacial structures. International Journal of Multiphase Flow 47, 171–182. URL: https://doi.org/10.1016/j.ijmultiphaseflow.2012.07.007, doi:10.1016/j.ijmultiphaseflow.2012.07.007.

[13] Hirt, C., 2003. Modeling turbulent entrainment of air at a free surface. Flow Science, Inc .

[14] Hirt, C., Nichols, B., 1981. Volume of fluid (VOF) method for the dynamics of free boundaries. Journal of Computational Physics 39, 201 – 225. URL: http://doi.org/10.1016/0021-9991(81)90145-5, doi:10.1016/0021-9991(81)90145-5.

[15] Issa, R.I., 1986. Solution of the implicitly discretised fluid flow equations by operator-splitting. Journal of Computational Physics 62, 40–65. URL: https://doi.org/10.1016/0021-9991(86)90099-9.

[16] Lopes, P., Leandro, J., Carvalho, R.F., 2017. Self-aeration modelling using a sub-grid volume-of-fluid model. International Journal of Nonlinear Sciences and Numerical Simulation 18. URL: https://doi.org/10.1515/ijnsns-2017-0015, doi:10.1515/ijnsns-2017-0015.

[17] Ma, J., Oberai, A.A., Drew, D.A., Lahey, R.T., Hyman, M.C., 2011. A comprehensive sub-grid air entrainment model for RaNS modeling of free-surface bubbly flows. The Journal of Computational Multiphase Flows 3, 41–56. URL: https://doi.org/10.1260/1757-482x.3.1.41, doi:10.1260/1757-482x.3.1.41.

[18] Matos, J., Pinheiro, A.N., Quintela, A.C., Frizell, K.H., 2001. On the role of stepped overlays to increase spillway capacity of embankment dams, in: Proceedings ICOLD European SymposiumDams in a European Context.

[19] Menter, F., 1993. Zonal two equation k-ω turbulence models for aerodynamic flows, in: 23rd Fluid Dynamics, Plasmadynamics, and Lasers Conference, American Institute of Aeronautics and Astronautics. URL: https://doi.org/10.2514/6.1993-2906, doi:10.2514/6.1993-2906.

[20] Moraga, F., Carrica, P., Drew, D., Lahey, R., 2008. A sub-grid air entrainment model for breaking bow waves and naval surface ships. Computers & Fluids 37, 281–298. URL: https://doi.org/10.1016/j.compfluid.2007.06.003, doi:10.1016/j.compfluid.2007.06.003.

[21] Mortazavi, M., Chenadec, V.L., Moin, P., Mani, A., 2016. Direct numerical simulation of a turbulent hydraulic jump: turbulence statistics and air entrainment. Journal of Fluid Mechanics 797, 60–94. URL: https://doi.org/10.1017/jfm.2016.230, doi:10.1017/jfm.2016.230.

[22] Pfister, M., Hager, W.H., 2011. Self-entrainment of air on stepped spillways. International Journal of Multiphase Flow 37, 99–107. URL: https://doi.org/10.1016/j.ijmultiphaseflow.2010.10.007, doi:10.1016/j.ijmultiphaseflow.2010.10.007.

[23] Qian, Z., Hu, X., Huai, W., Amador, A., 2009. Numerical simulation and analysis of water flow over stepped spillways. Science in China Series E: Technological Sciences 52, 1958–1965. URL: https://doi.org/10.1007/s11431-009-0127-z, doi:10.1007/s11431-009-0127-z.

[24] Rusche, H., 2002. Computational fluid dynamics of dispersed two-phase flows at high phase fractions. Ph.D. thesis. Imperial College of Science, Technology and Medicine. URL: http://hdl.handle.net/10044/1/8110.

[25] Shih, T.H., Liou, W.W., Shabbir, A., Yang, Z., Zhu, J., 1995. A new k-ϵ eddy viscosity model for high reynolds number turbulent flows. Computers & Fluids 24, 227–238. URL: https://doi.org/10.1016/0045-7930(94)00032-t, doi:10.1016/0045-7930(94)00032-t.

[26] Straub, L.G., Anderson, A.G., 1958. Experiments on self-aerated flow in open channels. J.Hydraul.Div. 84, 1–35.

[27] Valero, D., Bung, D., 2015. Hybrid investigation of air transport processes in moderately sloped stepped spillway flows, in: E-proceedings of the 36th IAHR World Congress 28 June - 3 July, 2015, The Hague, the Netherlands, pp. 1 – 10.

[28] Valero, D., Bung, D.B., 2016. Development of the interfacial air layer in the non-aerated region of high-velocity spillway flows. Instabilities growth, entrapped air and influence on the self-aeration onset. International Journal of Multiphase Flow 84, 66–74. URL: `https://doi.org/10.1016/j.ijmultiphaseflow.2016.04.012`, doi:`10.1016/j.ijmultiphaseflow.2016.04.012`.

[29] Viti, N., Valero, D., Gualtieri, C., 2018. Numerical simulation of hydraulic jumps. Part 2: Recent results and future outlook. Water 11, 1–18. URL: `https://doi.org/10.3390/w11010028`, doi:`10.3390/w11010028`.

[30] Wardle, K.E., Weller, H.G., 2013. Hybrid multiphase CFD solver for coupled dispersed/segregated flows in liquid-liquid extraction. International Journal of Chemical Engineering 2013. URL: `https://doi.org/10.1155/2013/128936`, doi:`10.1155/2013/128936`.

[31] Yan, K., Che, D., 2010. A coupled model for simulation of the gas–liquid two-phase flow with complex flow patterns. International Journal of Multiphase Flow 36, 333 – 348. URL: `https://doi.org/10.1016/j.ijmultiphaseflow.2009.11.007`, doi:`http://dx.doi.org/10.1016/j.ijmultiphaseflow.2009.11.007`.

[32] Zalesak, S.T., 1979. Fully multidimensional flux-corrected transport algorithms for fluids. Journal of Computational Physics 31, 335–362. URL: `https://doi.org/10.1016/0021-9991(79)90051-2`, doi:`10.1016/0021-9991(79)90051-2`.

[33] Zhang, G., Chanson, H., 2016. Hydraulics of the developing flow region of stepped spillways. I: Physical modeling and boundary layer development. Journal of Hydraulic Engineering 142, 04016015. URL: `https://doi.org/10.1061/(asce)hy.1943-7900.0001138`, doi:`10.1061/(asce)hy.1943-7900.0001138`.

A.3 Paper III: LES of a classical hydraulic jump: Influence of modelling parameters on the predictive accuracy

LES of a classical hydraulic jump: Influence of modelling parameters on the predictive accuracy

Timofey Mukha[a], Silje Kreken Almeland[b,*] and Rickard E. Bensow[a]

[a]Chalmers University of Technology, Department of Mechanics and Maritime Sciences, Hörsalsvbägen 7A, SE-412 96 Gothenburg, Sweden
[b]Norwegian University of Science and Technology, Department of Civil and Environmental Engineering, NO-7491 Trondheim, Norway

ARTICLE INFO

Keywords:
Hydraulic jump
Large-eddy simulation
CFD
OpenFOAM

ABSTRACT

Results from large-eddy simulations of a classical hydraulic jump at inlet Froude number 2 are reported. The computations are performed using the general-purpose finite-volume based code OpenFOAM®, and the primary goal is to evaluate the influence of modelling parameters on the predictive accuracy, as well as establish associated best-practice guidelines. A benchmark simulation on a dense computational mesh is conducted, and good agreement with existing reference data is found. The remaining simulations cover different selections of modelling parameters: geometric vs algebraic interface capturing, three mesh resolution levels, four choices of the convective flux interpolation scheme. Geometric interface capturing leads to better accuracy but deteriorated numerical stability and increased simulation times. Interestingly, numerical dissipation is shown to systematically improve the results, both in terms of accuracy and stability. The densest of the three grids, which is twice as coarse as the grid used in the benchmark simulation, was found to be sufficient for faithfully reproducing all the considered quantities of interest. The recommendation is therefore to use this grid, geometric interface capturing, and a second-order upwind scheme for the convective fluxes.

1. Introduction

A hydraulic jump is an abrupt change in the water depth accompanying the transition of the flow in a shallow canal from super- to subcritical. This transition causes energy dissipation, which defines the application of hydraulic jumps in engineering. In fact, according to [2], hydraulic jumps are the most commonly used energy dissipator in hydraulic structures. This motivates the significant attention this class of flows received from the scientific community. Hydraulic jumps have been the subject of a multitude of studies, both experimental and numerical, a recent review of which can be found in [21, 23]. Most works focus on the so-called ‘classical’ hydraulic jump (CHJ), which occurs in a smooth horizontal rectangular channel.

An illustration of the air-water interface in a CHJ is shown in Figure 1. The topology of the interface is complex and rapidly evolving, which can be fully appreciated by looking at the animations found in the supplementary material to this article. The interface dynamics are driven by a recirculating motion—the so called roller— which leads to overturning waves occurring across the jump. Consequently, a significant amount of air is entrained. A detailed discussion of the entrainment mechanism can be found in [15]. The flow in the jump is also highly turbulent, with a turbulent shear layer forming below the roller and interacting with it.

The main physical parameter of the CHJ is the inlet Froude number, Fr_1, computed based on the water inlet velocity, U_1, and its depth, d_1. Several classifications of the jump's behaviour based on Fr_1 can be found in the literature, see [21] and the references therein. The most stable CHJs occur when $\mathrm{Fr}_1 \in [4, 9]$. The rate of air entrainment also depends on the Froude number, and at higher Fr_1 the level of aeration is increased. In spite of the flow's complexity, given the parameters of the inflow, some of its properties can be easily derived analytically based on control volume analysis, see e.g. [12, p. 250]. This includes the water depth after the jump, $d_2 = 0.5 d_1 \left((1 + 8\mathrm{Fr}_1^2)^{0.5} - 1 \right)$.

From a numerical perspective, the CHJ represents an extremely challenging test of predictive capabilities for multiphase modelling approaches. A suitable model should be able to capture fast and complex topology changes taking place across a wide range of spatial scales. Accurate turbulence modelling is also necessary and, in particular, the

---

*Corresponding author

timofey@chalmers.se (T. Mukha); silje.k.almeland@ntnu.no (S.K. Almeland); rickard.bensow@chalmers.se (R.E. Bensow)

ORCID(s): 0000-0002-2195-8408 (T. Mukha); 0000-0003-3106-0623 (S.K. Almeland); 0000-0002-8208-0619 (R.E. Bensow)

Figure 1: Classical hydraulic jump at $Fr_1 = 2$, a snapshot of the air-water interface.

possibility to properly account for its interaction with the multiphase structures. On the other hand, the geometric simplicity of the case makes mesh generation easy, and the abundance of published experimental data makes validation easier. Furthermore, data from direct numerical simulation (DNS) [15] is also available.

A compilation of previous numerical studies of the CHJ, classified by turbulence modelling approach, and also Fr_1, can be found in [23]. The majority of works are based on two-equation Reynolds-averaged Navier-Stokes (RANS) turbulence models and the Volume of Fluid (VoF) method for capturing the interface. Note that in RANS it is assumed that there is a clear scale separation between the modelled turbulent motion and other types of unsteadiness. In the case of a CHJ, this is unlikely to take place due to the direct interaction between turbulence and multiphase structures, e.g. entrained bubbles. Generally, it is unclear whether the topological changes in the flow occur significantly slower than the integral time scales of turbulence. A possibility for resolving this inconsistency is keeping the resolution coarse enough for the interface to remain steady, and introduce an explicit model for air entrainment, as done in [14]. However, these theoretical difficulties do not imply that RANS cannot be used to obtain useful results. On the contrary, as summarized in [23], RANS is capable of predicting d_2, the mean location of the interface, and the length of the roller with $< 5\%$ relative error.

In order to get new physical insights, and get an accurate picture of the turbulent motion inside the jump, scale-resolving turbulence modelling approaches can be used. Only a few studies report results from such simulations. The DNS by Mortazavi et al. [15] has already been mentioned above, and represents an important milestone. In [10], Detached-Eddy Simulation (DES) was used. A detailed analysis of the flow is given, in particular, a quadrant decomposition of the turbulent shear stress is considered, as well as high-order statistical moments of the velocity field. A Large-Eddy Simulation (LES) of a CHJ was conducted as part of the study by Gonzalez and Bombardelli, which also includes RANS simulations [7]. Unfortunately, due to the reference being a short conference abstract, results are only discussed superficially. In [13] the authors report on an unsuccessful attempt to conduct a LES: the location of the jump could not be stabilized. Finally, in [14], which was already mentioned in the context of RANS, results from DES modelling are also discussed. However, the simulation in question is not a DES in the classical sense, i.e. not a fully resolved LES outside the RANS region. Instead, a rather coarse mesh is used and an air entrainment model is employed. Nevertheless, this DES yielded more accurate results than the corresponding RANS.

In summary, only two articles [15, 10] contain detailed reports on scale-resolving simulations of the CHJ to date. Nevertheless, with the increase of available computing power, it can be expected that LES and its hybrids will find wider adoption in hydraulic engineering in the near future. This transition is already well underway in, for example, the automotive and aerospace industries. From a practical perspective, an important step is to establish guidelines for the selection of the most important LES modelling parameters. Of immediate interest is to form them for the particular case of solvers based on finite-volume discretisation, since these are currently the workhorse of industrial computational fluid dynamics. In this numerical framework, the two arguably most important LES input parameters are the density of the grid and the numerical scheme used for interpolating convective fluxes. Both control the capability of the LES to resolve turbulent structures, and also the stability of the simulation. In the case of multiphase flow, the choice of the interface capturing scheme is also important. The goal of this paper is to quantify the effects of these three parameters on the various quantities of interest. To that end, results from an LES campaign, consisting of 25 simulations of a CHJ at $\mathrm{Fr}_1 = 2$, are presented. The campaign covers four different mesh resolution levels, and two VoF approaches: algebraic and geometric. The diffusivity of the convective flux interpolation scheme is also controlled, and four diffusivity levels are considered. All the simulation results, including ready-to-run simulation cases, are made available as a supplementary dataset.[1]

The remainder of the article is structured as follows. Section 2 presents the computational fluid dynamics methods used in the paper. The setup of the CHJ simulations is presented in Section 3. The results of the simulation campaign are shown and analysed in Section 4. Finally, conluding remarks are given in Section 5.

2. Computational fluid dynamics methods

2.1. Governing equations

The Volume of Fluid (VoF) method [8] is used to simulate the flow. Accordingly, a single set of conservation equations is solved for both fluids, and the phase is distinguished based on the values of the volume fraction of the liquid, α. The momentum and continuity equations read as follows,

$$\frac{\partial \rho u_i}{\partial t} + \frac{\partial}{\partial x_j}\left(\rho u_i u_j\right) = -\frac{\partial p_{\rho g h}}{\partial x_i} - g_i x_i \frac{\partial \rho}{\partial x_i} + \frac{\partial}{\partial x_j}\left(\mu\left(\frac{\partial u_i}{\partial x_j} + \frac{\partial u_j}{\partial x_i}\right)\right) + f_s, \quad (i = 1, 2, 3) \tag{1}$$

$$\frac{\partial u_j}{\partial x_j} = 0. \tag{2}$$

Here, summation is implied for repeated indices, u_i is the velocity, ρ is the density, μ is the dynamic viscosity, g_i is the standard acceleration due to gravity, $p_{\rho g h} = p - \rho g_i x_i$ is the dynamic pressure, and f_s is the surface tension force. The latter is accounted for using the Continuous Force Model [3]:

$$f_i^s = \sigma \kappa \frac{\partial \alpha}{\partial x_i}. \tag{3}$$

Here, σ is the surface tension coefficient and $\kappa = \partial n_i^f / \partial x_i$ is the curvature of the interface between the two phases, where n_i^f is the interface unit-normal, which is computed as follows,

$$n_i^f = \frac{\partial \alpha}{\partial x_i} \Bigg/ \left(\left|\frac{\partial \alpha}{\partial x_i}\right| + \delta_N\right). \tag{4}$$

Here, δ_N is a small number added for the sake of numerical stability.

Equations (1)-(2) must be complemented with an interface capturing approach in order to compute the distribution of α. Methodologies for this are discussed in the next subsection. Given the values of α, the local material properties of the fluid are computed as

$$\rho = \alpha \rho_1 + (1 - \alpha)\rho_2, \qquad \mu = \alpha \mu_1 + (1 - \alpha)\mu_2, \tag{5}$$

where the indices 1 and 2 are used to refer to the liquid and gas properties, respectively.

2.2. Interface capturing methods

As discussed above, it is necessary to introduce a method for computing the evolution of α, i.e. capture the location of the interface between the two fluids. Here, two different approaches to this are considered. The first is algebraic, meaning that a transport equation for α is solved:

$$\frac{\partial \alpha}{\partial t} + \frac{\partial u_j \alpha}{\partial x_j} + \frac{\partial}{\partial x_j}\left(u_j^r (1 - \alpha)\alpha\right) = 0. \tag{6}$$

The last term in the equation is artificial and its purpose is to introduce additional compression of the interface. To that end, the direction of u_i^r is aligned with the interface normal, n_i^f. The magnitude of u_i^r is defined as $C_\alpha |u_i|$, where $C_\alpha = 1$ is an adjustable constant.

Special treatment of the convective term in (6) is necessary in order to ensure that α is bound to values between 0 and 1. Typically, a total-variation diminishing (TVD) scheme is chosen to compute the convective flux, but this can be

---

[1] DOI: `10.6084/m9.figshare.12593480`

insufficient because the TVD property of such schemes is, in fact, only strictly valid for one-dimensional problems. An additional flux limiting technique, referred to as MULES, is used to rectify this. While we omit discussing MULES in detail and instead refer the reader to [5], we note that it is based on the idea of Flux Corrected Transport and the work of Zalesak [27]. It should also be mentioned that two variations of MULES are available in OpenFOAM®, explicit and semi-implicit. Using the latter sometimes allows to keep the simulation stable for CFL numbers larger than one.

The second approach belongs to the class of geometric VoF methods, and is referred to as isoAdvector. The details on isoAdvector can be found in [18], here we provide a brief summary of the key steps of the algorithm. In contrast to algebraic VoF, here the surface of the interface is explicitly reconstructed at each time-step. Within each cell, it is represented by a plane, and the reconstruction algorithm ensures that it divides the cell volume consistently with the local value of α. To predict the location of the interface at the next time-step, it is advected along the direction of the interface normal. For each cell, the advection velocity is obtained using linear interpolation from the vertices of the cell onto the centroid of the interface-plane. Then, based on the predicted new location of the interface, the change in α is computed.

Comparing the two approaches, one can generally say that geometric VoF can be expected to be more accurate, yet more computationally demanding. Quantifying these differences for the case of the hydraulic jump is one of the goals of the present paper. A significant drawback of the algebraic VoF is the necessity to choose the convection scheme for α, which can have a large influence on the results. Selecting the values of model constants, such as C_α, also represents a difficulty.

2.3. Numerical methods

The computations are performed using the open-source CFD software OpenFOAM® version 1806. This code is based on cell-centred finite-volume discretization, which can currently be considered standard for industrial CFD. Two solvers distributed with OpenFOAM® were employed, corresponding to the two VoF methodologies discussed above. For algebraic VoF, the solver `interFoam` was used, whereas the isoAdvector is implemented in the `interIsoFoam` solver. Here we omit the particulars regarding the solver algorithms, but note that they are based on the PISO [9] pressure-velocity coupling procedure. For a detailed discussion we refer the reader to the following thesis works [19, 5].

A key component of the finite-volume method are the spatial interpolation and time integration schemes. For spatial interpolation, the goal is to obtain the values of the unknowns at the cell face centroids based on the values at the centroids of the cells. The most trivial choice is using linear interpolation, which is second-order accurate. This scheme can be applied to interpolation of diffusive fluxes without negative side-effects. Unfortunately, when applied to convective fluxes, linear interpolation leads to a dispersive error. In spite of this, in single-phase LES and DNS it is common practice to use this scheme anyway because the high density of the mesh, in combination with a small time-step, allows to avoid any significant contamination of the solution. On the other hand, in industrial flow simulations it is quite common to use a second-order upwind scheme. Although also unbounded, the error introduced by this scheme is dominated by a dissipative term, which facilitates the stability of the simulation but negatively affects the capability to resolve small-scale turbulent motions. In this work, a linear blending of these two interpolation schemes will be considered. The following weights for the linear upwind scheme will be tested: 10%, 25%, 50%, and 100%. For simplicity, this weight will be referred to as 'the amount of upwinding' in the remainder of the paper.

For time integration, both solvers have the option of using a first-order implicit Euler scheme. In `interFoam`, the Crank-Nicholson scheme can also be used, as well as a linear blending of Crank-Nicholson and Euler. In `interIsoFoam`, one can instead use a second-order accurate backward-differencing scheme. Unfortunately, it was only possible to keep the simulations stable using the Euler scheme. However, since the employed time-step sizes are kept low, it is anticipated that the numerical errors are dominated by the spatial interpolation errors, whereas the time-integration error plays a smaller role.

Finally, in the case of MULES, a scheme has to be chosen for the convection of α. Here a TVD scheme using the van Leer limiter is selected to that end, see [22, p. 170] for the definition. The selected limiter results in a more diffusive scheme than some alternatives, but here the artificial compression term in (6) remedies that.

2.4. Turbulence modelling

In order to obtain the governing equations for LES based on the employed two-phase flow model, spatial filtering should be formally applied to equations (1)-(2), as well as (6) in the case of algebraic VoF. Following standard practice, we use implicitly-filtered LES, letting the finite volume grid act as the spatial filter. The associated filter size is equal to the cubic root of the local computational cell volume.

Filtering leads to the appearance of the subgrid stress (SGS) term in the momentum equation (1). For several reasons, here we choose to ignore this term instead of modelling it. One reason is the relatively dissipative numerical schemes employed in the solution procedure. When a high amount of upwinding is present, it can be expected that the numerical dissipation is comparable in magnitude to that produced by a Boussinesq-type SGS model. This stacking of artificial and modelled dissipation leads to deterioration of accuracy. Another reason is the overall negative experience of the authors with the SGS models implemented in OpenFOAM®. Some results for turbulent channel flow and several available models can be found in [16]. In that study, only the dynamic k-equation model [11] does not lead to worsened results compared to not using a model at all. Also, one of the goals of this paper is to see what accuracy can be achieved on coarse grids, which are technically not suitable for LES but may nevertheless appear in an industrial setting due to limitations in computing resources. Using an SGS model that is designed to model a specific part of turbulent spectrum is unlikely to be fruitful in this context. Finally, it should be noted that the existing closures where designed for single-phase flows, and do not account for the interaction effects between multiphase and turbulent structures. Detailed investigations of the impact of this on the predictive accuracy have not yet been reported in the literature. Consequently, using such SGS models in hydraulic jump simulations can be called into question.

2.5. Instability sources in VoF simulations

Compared to single-phase LES, numerical stability in LES-VoF simulations can be significantly harder to achieve. As discussed in Section 4, for certain combinations of the grid resolution, VoF methodology, and amount of upwinding, the CHJ simulations diverged. It is therefore appropriate to briefly review the main additional sources of numerical instability intrinsic to the considered multiphase modelling approach.

The Continuous Force Model, see (3)-(4), used for the surface tension force computation can lead to parasitic currents across the interface between the phases. An illustration of such currents produced in an `interFoam` simulation of a single rising bubble can be found in [4]. The source of the currents is the numerical imbalance between the pressure gradient across the interface and the surface tension. When the velocity of the parasitic current becomes large, the simulation may crash. A multitude of improvements to the Continuous Force Model have been proposed, ranging from more accurate curvature estimation algorithms to more robust discrete handling of the balance between pressure and surface tension forces, see, for example, [17]. Unfortunately, none of these have been implemented and publicly released in OpenFOAM®, although there are ongoing efforts [20]. Interestingly, in [20] the author mentions that the sharper interface obtained using `isoAdvector` actually increases the magnitude of the parasitic currents.

The second source of instabilities is the treatment of the gravity term in the momentum equation (1). When a segregated pressure-velocity coupling algorithm, such as PISO, is used, a numerical imbalance between the dynamic pressure gradient and the density gradient terms can occur, which will be compensated by an acceleration of the fluid [24]. This can lead to a strong increase of velocity magnitude in the gas above the interface, due to its low density. For this reason, it is not uncommon to artificially increase the density of the gas to facilitate stability.

The crucial practical consequence of the above is that one does not necessarily get a more stable simulation by refining the grid and using a more accurate interface capturing approach. This is very different from single-phase incompressible LES, in which dampening numerical instabilities by using a denser grid or a smaller time-step is a common strategy. It should also be mentioned that it is not possible to predict when the discussed instabilities will take place. Some of the CHJ simulations conducted as part of this study were well under way when the destabilizing velocity overshoots occurred, leading to loss of tens of thousands of core-hours worth of computing time. An even more unfortunate scenario is when a very strong spurious current takes place, but no crash occurs. The simulation finishes, but the results are unpublishable because the computed statistical moments of velocity are contaminated. In our simulations, the solver would sometimes exhibit surprising resilience and survive currents that are 3 orders of magnitude stronger than the characteristic velocity scale of the flow. It is therefore recommended to closely monitor the maximum velocity values in the course of the simulation.

3. Simulation setup

The setup of the simulation is similar to that used in the DNS by Mortazavi et al. [15], which is later used as reference. An overview of the computational domain, as well as boundary conditions, can be found in Figure 2, and Table 1 contains a full list of the setup parameters. The main difficulty in setting up a hydraulic jump simulation is obtaining a stable jump positioned sufficiently far away from the inlet and outlet boundaries of the domain. A common approach to facilitating the formation of the jump is by introducing a vertical barrier—a weir—some distance upstream of the outlet, see e.g. [25, 10, 26]. In other works [15, 1, 2], including the reference DNS, the jump is controlled by the boundary condition at the outlet of the domain. The particular condition enforced varies among the studies.

Here, the weir approach is employed due to its simplicity. This choice also facilitates reproducibility by making the simulation setup easier to reproduce in any CFD code, without the need to program a new boundary condition. Test simulations were necessary to find a configuration of the domain length L_x, weir height H_w, and the streamwise position of the weir, L_w, in order to get a stable jump positioned roughly in the middle of the domain. The streamwise dimension of the weir is always set to equal the size of a computational cell, which is defined below. A simple pressure outlet is used on the downstream boundary.

At the inlet, the depth of the water, d_1 and the inlet velocity U_1, are set to enforce $\mathrm{Fr}_1 = U_1/\sqrt{gd_1} = 2$. In the air phase, a Blasius boundary layer profile subtracted from U_1 is enforced. The thickness of the boundary layer is $\delta = 1.3d_1$. This matches the condition in the reference DNS.

The condition at the bottom surface is also matched and is set to a slip wall. This allows to not spend computational resources on the boundary layer, which would have been formed if a no-slip condition were to be imposed. In the DNS, a slip condition is also used for the top boundary. However, we find this choice difficult to justify and instead impose a pressure outlet, mimicking the atmosphere. Accordingly, the height of the domain is made significantly larger than in the DNS as well. Some test simulations with a slip applied to the top boundary were nevertheless conducted, and the changes in the obtained solution were not significant.

The spanwise extent of the domain, L_z, was set to match the DNS, $L_z = 4.2d_1$. However, analysis of two-point autocorrelations of the velocity field at selected locations (presented below) revealed that a larger L_z should preferably be used. Due to limitations in computational resources, it was not possible to extend L_z in all the conducted simulations. However, in the simulations on coarser meshes (defined below), $L_z = 8.4d_1$ was used. One the one hand, this can be seen as an impediment to consistent evaluation of the predictive accuracy across several mesh densities. On the other hand, simulations on coarse meshes are more prone to deteriorating in accuracy due to an insufficiently wide domain, because a coarse mesh tends to introduce spurious spatial correlations. The latter consideration was judged to outweigh the former.

It remains to define the material properties of the fluids: their densities, kinematic viscosities, and also the surface tension coefficient. These are adjusted to exactly match the dimensionless parameters of the DNS, which includes the Weber number, $\mathrm{We} = \rho_1 U_1^2 d_1/\sigma = 1820$, the Reynolds number, $\mathrm{Re} = U_1 d_1/\nu_1 = 11000$, density ratio, $\rho_1/\rho_2 = 831$, and dynamic viscosity ratio, $\mu_1/\mu_2 = 50.5$. The corresponding dimensional values can be found in Table 1.

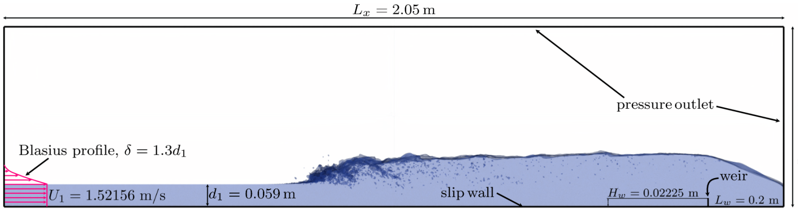

Figure 2: Simulation setup.

Several computational meshes, varying in their density, are employed in the study. All the meshes are fully defined in the next section, and here the general topology, which all the meshes share, is presented. The region occupied by the jump is meshed using cubic cells. This can be considered optimal in terms of the performance of the employed numerical algorithms. A rapid coarsening towards the top boundary is introduced slightly above the half-height of the domain. Similarly, the mesh is coarsened towards the outlet past the location of the weir. Coarsening towards the inlet is also present, starting about half-way from the position of the jump to the inlet.

Table 1
Simulation parameters.

Property	**Value**
Water inlet height, d_1	0.0059 m
Domain length, L_x	2.05 m, $\approx 34.75d_1$
Domain height, L_y	0.47355 m, $\approx 8d_1$
Domain width, L_z	0.2478 m / 0.4956 m, $4.2d_1$ / $8.4d_1$
Weir height, H_w	0.02225 m
Distance from the weir to the outlet, L_w	0.2 m
Liquid density, ρ_1	1.20012 kg/m^3
Gas density, ρ_2	997.3 kg/m^3
Density ratio, ρ_1/ρ_2	831
Liquid kinematic viscosity, ν_1	$8.1611213 \cdot 10^{-6}$ m^2/s
Gas kinematic viscosity, ν_2	$1.34295 \cdot 10^{-4}$ m^2/s
Kinematic viscosity ratio, ν_1/ν_2	0.06077
Dynamic viscosity ratio, μ_1/μ_2	50.5
Surface tension coefficient, σ	0.07484925
Water inlet velocity, U_1	1.52156 m/s
Inlet Froude number, Fr_1	2
Weber number, We	1820
Reynolds number, Re	11 000

4. Numerical experiments

In this section, the results of the simulations are presented and discussed. First, an overview of the simulation campaign is given in Section 4.1. This is followed by a presentation of results from the simulation on the densest mesh and their comparison with reference DNS data in Section 4.2. Finally, in Section 4.3, the effects of various modelling parameters are quantified.

4.1. Simulation campaign overview

The simulation campaign consists of 25 cases, which differ in the amount of upwinding introduced by the convective flux interpolation scheme, the density of the grid, and the VoF methodology employed.

A single simulation, referred to as the benchmark, has been run on a grid with the edge of the cubic cells Δx set to 1 mm, which is approximately equal to the resolution used in the DNS. With this grid, the theoretical height of the jump, $d_2 - d_1$, is discretized by 81 cells. The size of the grid is $\approx$ 83 million cells. The algebraic VoF was used, and only 2% upwinding was employed. We note that the initial plan was to use the geometric VoF for the benchmark simulation due to its superior accuracy. However, stabilizing the simulation proved difficult. Several costly attempts were made, with the amount of upwinding gradually increased, but even with 20% upwinding instabilities occurred.

The rest of the simulations cover the following choices for the grid resolution, $\Delta x \in [2, 3, 4]$ mm, and amount of upwinding, $[10\%, 25\%, 50\%, 100\%]$. We will from here on refer to the four grids used in the study as [$\Delta x1$, $\Delta x2$, $\Delta x3$, $\Delta x4$], and denote the amount of upwinding as [$u10\%$, $u25\%$, $u50\%$, $u100\%$]. For each configuration, algebraic and geometric VoF are considered, which will be referred to by the name of the key underlying algorithm, MULES and isoAdvector, respectively. As mentioned in Section 3, for simulations on grids $\Delta x3$ and $\Delta x4$ the value of L_z was doubled.

All simulations were first run for 1 s of simulation time, after which time-averaging was commenced and continued for 11 s. This corresponds to $\approx 283d_1/U_1$ time-units. By comparison, the reference DNS was averaged across 120 time-units. To obtain the final statistical results spatial averaging along the spanwise direction was performed. The time- and spanwise-averaged quantities will be denoted with angular brackets below, $\langle \cdot \rangle$. Adaptive time-stepping based on the maximum value of the CFL number currently registered in the domain was used. For simulations using MULES, the maximum CFL allowed was 0.75, whereas 0.5 was used with isoAdvector.

Further notation used in the remainder of the paper is now introduced. The mean location of the interface is denoted as $\langle \alpha_{0.5} \rangle$, corresponding to the 0.5 isoline in the mean volume fraction field. The triple u, v, w is used to denote the three Cartesian components of velocity. The location of the toe of the jump, x_{toe}, is defined as the streawise location at which the vertical position of $\langle \alpha_{0.5} \rangle$ is $1.1d_1$. The same definition is used in the reference DNS data [15]. The following rescaling of the coordinate system will be used: $x' = (x - x_{toe})/d_1$, $y' = y/d_1$.

4.2. Benchmark simulation

Here the results of the benchmark simulation are compared to the DNS of Mortazavi et al. [15]. The grid resolution in the two simulations is similar, but the setup doesn't match exactly, as pointed out in Section 3. There are also certain differences in the definitions of the considered quantities of interest, as discussed below. Additionally, for certain quantities the DNS is clearly poorly converged. Nevertheless, a qualitative and, in most cases, quantitative comparison of the results is possible, with the DNS generally considered as reference, since it was performed using more accurate numerics. The primary goal here is not to obtain perfect agreement, but rather to answer the principle question of whether the employed physical and numerical modelling frameworks are capable of capturing the properties of such a complicated flow.

An overview of the distribution of the main flow quantities is given first, see Figure 3. The top-left plot shows the distribution of $\langle \alpha \rangle$, with the magenta line showing $\langle \alpha_{0.5} \rangle$. Close to the toe of the jump, and some distance downstream, the values of $\langle \alpha \rangle$ are significantly lower than 1, indicating air entrainment. The mean streamwise and vertical velocities are shown in the top-right and bottom-left plots, respectively. As expected, the streamwise velocity is significantly lower downstream of the jump. It is also visible how the boundary layer in the gas follows the interface, leading to an increase in the vertical velocity in a region above the toe of the jump. Finally, the mean turbulent kinetic energy per unit mass, $\langle k \rangle$, is shown in the bottom-right plot. High values are observed in the region close to the toe, with the peak directly downstream of it. This reflects the coupling between turbulence and the air entrainment.

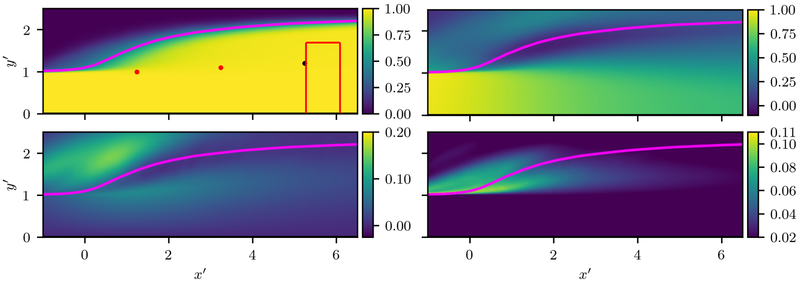

Figure 3: Distribution of $\langle \alpha \rangle$ (top-left), $\langle u \rangle/U_1$ (top-right), $\langle v \rangle/U_1$ (bottom left), $\langle k \rangle/U_1^2$ (bottom-right) in the benchmark simulation. The magenta line shows $\langle \alpha_{0.5} \rangle$.

As discussed in the introduction, the depth of the water after the jump, d_2, can be computed a priori. It is therefore possible to compute how the location of the interface approaches d_2 with increasing x. The corresponding graph is shown in Figure 4 along with the reference DNS data. We note that the value at $x' = 0$ is fixed through the definition for x_{toe}, which explains why the agreement with the DNS is perfect. The rate of growth of the water depth continues to be similar in both the LES and DNS up to $x' \approx 1$. Further downstream the DNS values converge towards d_2 at a faster pace, and for the LES, full convergence is in fact not achieved in the limits of the computational domain. The observed discrepancy is likely explained by the difference in the treatment of the outflow boundary.

Figure 5 shows the obtained profiles of $\langle \alpha \rangle$. Agreement with the DNS is extremely good, with observable discrepancies only at $x' = 0$ and $x' = 1$. As discussed above, the most intense air entrainment occurs right downstream of the toe, so it is unsurprising that capturing the correct $\langle \alpha \rangle$ profile in this region is the most difficult.

The mean streamwise and vertical velocity profiles are shown in Figure 6. The horizontal magenta lines show the positions of $\langle \alpha_{0.5} \rangle$. Excellent agreement with the reference is obtained at all 6 streamwise positions. Noticeable deviation is only observed in the values of vertical velocity of the air, which are not of particular interest and can be significantly affected by the boundary condition at the top of the domain.

The profiles of the root-mean-square values of the three velocity components are shown in Figure 7. We note that inspection of the DNS data clearly shows that these second-order statistical moments are not completely converged,

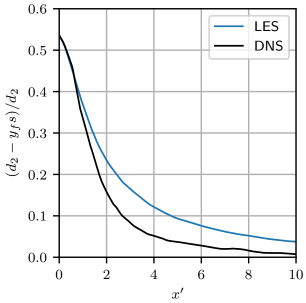

Figure 4: Convergence of the interface height towards d_2 in the benchmark simulation.

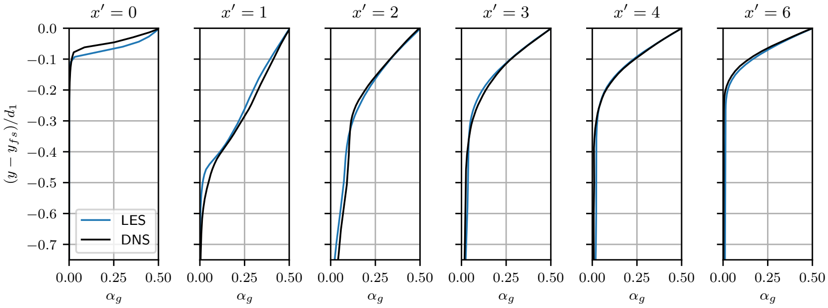

Figure 5: The profiles of $\langle \alpha \rangle$ in the benchmark simulation.

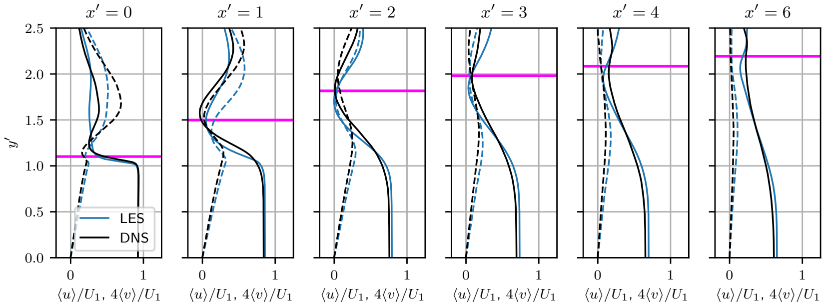

Figure 6: The profiles of $\langle u \rangle$ and $4\langle v \rangle$ obtained in the benchmark simulation. The magenta line shows the location of the interface.

see Figure 8 in [15]. In light of this, and the differences in the simulation setup, the obtained agreement is generally very good. All three components are predicted with similar accuracy. It is noteworthy that the disagreement with DNS is chiefly observed in the air and a short distance below the interface, whereas closer to the bottom the match is close to perfect. In other words, the accuracy becomes worse in the presence of rapid interface topology changes. This clearly demonstrates the importance of the interaction between the multiphase and turbulent structures.

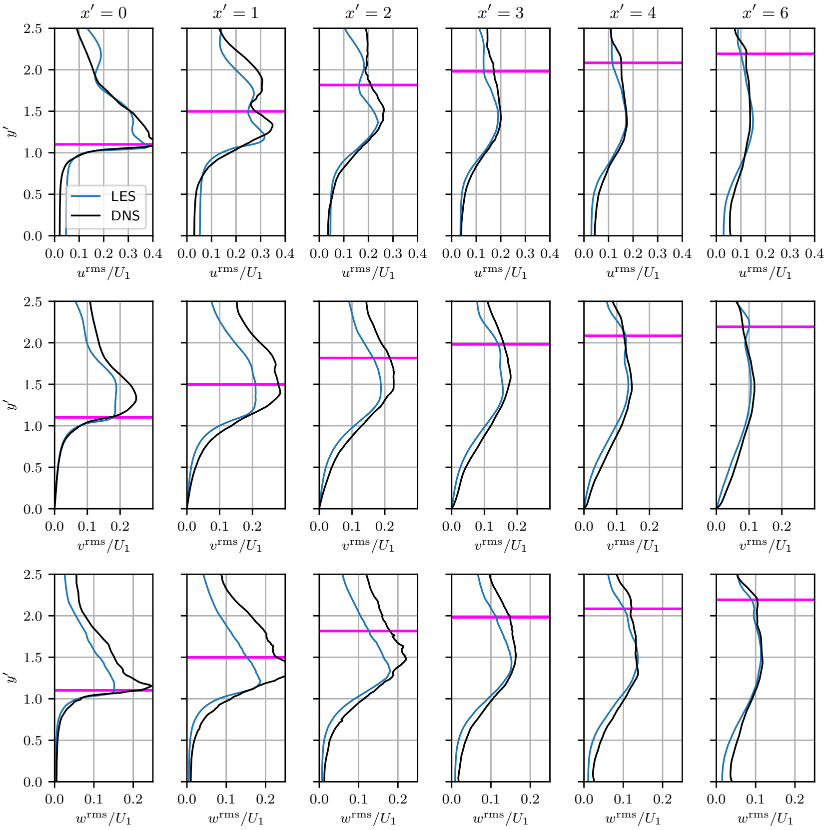

Figure 7: The profiles of u^{rms}/U_1, v^{rms}/U_1, and w^{rms}/U_1 obtained in the benchmark simulation. The magenta line shows the location of the interface.

The analysis continues with the consideration of the temporal energy spectra of the velocity fluctuations. These were computed at two $[x', y']$ positions: [1.24, 1], [3.24, 1.1]. These are shown with red dots in top-left plot in Figure 3. Note that the x' values were essentially an outcome of the simulation, since it was not possible to know the value of x_{toe} a priori. Furthermore, the intention is to use the same x and y values in the whole simulation campaign, and the location of x_{toe} varies slightly from simulation to simulation. The values were therefore chosen in a conservative way to ensure that both locations are to the right of the toe. The DNS data also provides temporal velocity spectra, including the following $[x', y']$ positions: $[0, 1]$, $[2, 1.1]$. Both the DNS and LES data are shown in Figure 8. The LES recovers the correct slope in the inertial range, which is in most cases close to the canonical $-5/3$-power spectrum. Less energy is contained in the fluctuations in the case of the LES, but a this is likely to be a consequence of the signals being sampled from locations further from the toe. Spectra for all three velocity components are predicted with comparable precision.

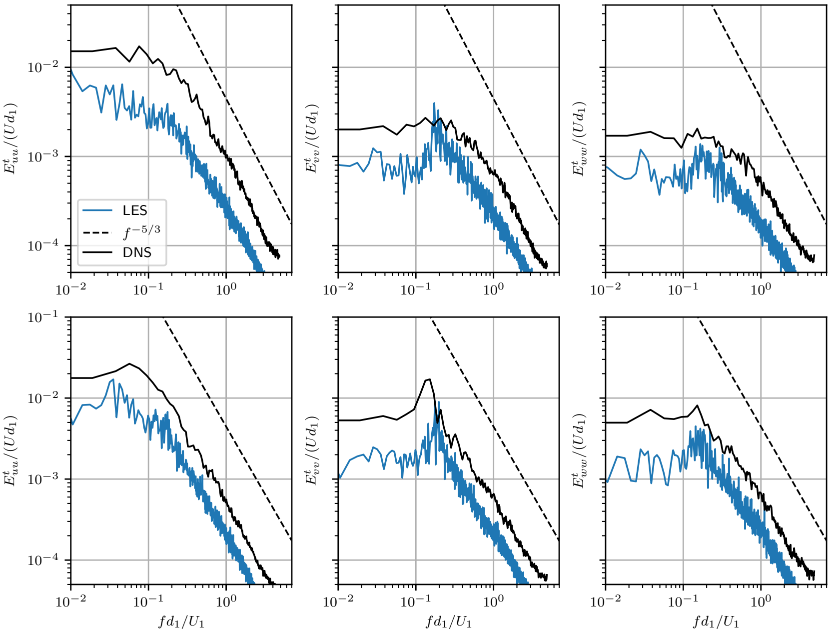

Figure 8: Temporal energy spectra of the three components of velocity at two selected $[x', y']$ positions: $[1.24, 1]$ (top), $[3.24, 1.1]$ (bottom).

Next, the spanwise autocorrelation functions of the three velocity components, $R_{u_i u_i}$, are considered. These are computed at the same two $[x', y']$ locations as the temporal spectra, plus an additional location further downstream: $[5.24, 1]$, see the black dot in Figure 3. The result is shown in Figure 9. Evidently, R_{uu}, does not decline to zero for two of the three considered locations. This indicates that the spanwise dimension of the computational domain is somewhat insufficient, and prompted the use of a larger domain for the simulations on the $\Delta x3$ and $\Delta x4$ meshes. The figure also presents the ratio of the integral length scales $L_{u_i u_i}$ and the cell size in the spanwise direction Δz. The smallest scale to be discretized is L_{ww}, and at $[1.24, 1]$ it is only covered by ≈ 6.6 cells. By comparison, in [6], 8 cells is recommended for a *coarse* LES. This indicates that even with the $\Delta x1$ mesh some turbulent scales are resolved poorly. Alternatively, the integral length scale may be a poor metric to relate grid resolution to for this particular flow. In any case, further downstream $L_{u_i u_i}$ grow, meaning that the resolution with respect to them improves.

Lastly, we analyse the air entrainment by considering the temporal variation of the volume of air passing through

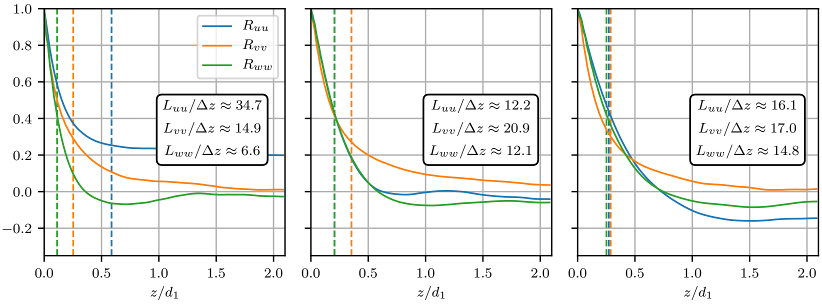

Figure 9: Spanwise two-point auto-correlations of velocity components computed at 3 selected $[x', y']$ locations: $[1.24, 1]$ (left), $[3.24, 1.1]$ (middle), $[5.24, 1]$ (right). Vertical dashed lines show the integral length scale.

the box $x' \in [5.27, 6.09]$, $y' \in [0, 1.70]$. The box is shown with red lines in the top-left plot in Figure 3. Similar to the analysis made for the DNS [15], we consider the autocorrelation function of the recorded signal. The result is shown in Figure 10. As expected, strong periodicity is revealed. The DNS data appears somewhat unconverged, but the location of the first peak is relatively close to the LES. The integral time-scales corresponding to the two curves are clearly different, but that is explained by the fact that the width of the box used for sampling the signal is larger in the LES.

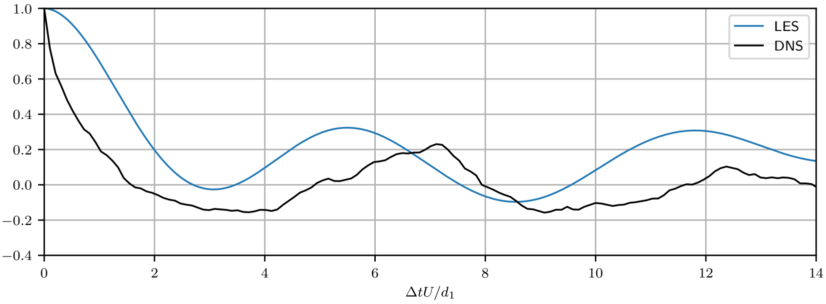

Figure 10: Autocorrelation function of the time-signal of the air volume passing through the box $x' \in [5.27, 6.09]$, $y' \in [0, 1.70]$.

The primary conclusion of this section is that OpenFOAM® can be successfully used for scale-resolving simulations of the CHJ. This can probably be extended to include other codes based on the same discretization and multiphase modelling frameworks. In spite of the slight differences in the simulation setup, the observed overall agreement with the DNS data is good not only for first- and second-order statistical moments of the considered flow variables, but also for temporal turbulent spectra and air entrainment properties. The largest deviations with DNS were observed directly downstream of the toe of the jump, which is physically the most complicated region to simulate.

Table 2
The simulation cost metric, N_h. For each Δx and $u\%$ combination, two values are given, corresponding to MULES and isoAdvector, respectively.

	$u10\%$	$u25\%$	$u50\%$	$u100\%$
$\Delta x2$	595/825	553/855	554/778	591/801
$\Delta x3$	284/-	197/257	199/264	198/250
$\Delta x4$	75/-	53/62	52/66	50/64

4.3. Influence of modelling parameters

In this section, the effects of the grid resolution, amount of upwinding, and interface capturing method on the cost and accuracy of the results are considered. The cost of the simulations is analysed first, and the associated metric, N_h is defined as follows. First, the simulation logs are used to compute the number of physical hours necessary to advance each simulation by 1 s. Since the simulations on different grids were parallelised using different amounts of computational cores, the obtained timings are then multiplied by the corresponding amount of cores used. This assumes linear scaling of computational effort with parallelisation, which is not exact, but provides a very good approximation in the range of core numbers used in the study. Recall also that in the simulations using isoAdvector the time-step was adjusted to ensure the maximum Courant number is < 0.5, whereas 0.75 was used in the MULES simulations. To be able to account for the cost difference associated with the VoF algorithm as such, the cost metric for the MULES simulations was premultiplied by $0.75/0.5$. Note that since a typical desktop computer has around 10 computational cores, and the full simulation needs to be run for about 10 s, N_h also gives a rough estimate of how many hours it would take to perform a given simulation on a desktop machine.

The obtained values of N_h are shown in Table 2. Each entry contains two numbers, corresponding to MULES and isoAdvector. It is evident that the isoAdvector simulations are more expensive. Depending on the other simulation parameters the ratio of N_h varies within $\approx [1.17, 1.55]$. As a general trend, the isoAdvector becomes relatively more expensive with increased mesh resolution. Numerical dissipation sometimes favourably affects the amount of iterations necessary to solve the pressure equation. Here this effect is observed when the transition from 10% to 25% upwinding occurs, with the former always leading to a more expensive simulation. However, for higher $u\%$, the effect of dissipaion on N_h is neither particularly strong nor regular. Considering the cost as a function of Δx, it is crucial to recall that the $\Delta x2$ simulations are performed on a thinner domain. Since the computational effort does not scale linearly with the number of cells, this could not be directly accounted for in the metric. Based on the data, on a desktop machine, it is possible to perform the $\Delta x4$ simulations in about 3 days, and the $\Delta x3$ in about 10. For $\Delta x2$, the corresponding number is from 25 to 35 days depending on the simulation settings. Taking into account the increased access of both academia and industry to HPC hardware, it can be said that the simulations on all three grids are relatively cheap, at least by LES standards.

Next, the computed profiles of $\langle \alpha \rangle$ are investigated, see Figure 11. The benchmark simulation revealed that the region of the flow that is most difficult to predict is directly downstream of the toe. Therefore, here we focus on the following streamwise positions: $x' = 0.5, 1.0, 2.0$. The clear trend overarching all x' and Δx is that a higher amount of upwinding leads to better results. For the majority of Δx and streamwise positions, using isoAdvector and $u100\%$ leads to the best predictive accuracy. The fact that using more dissipative schemes improves results is somewhat unexpected, because typically the recommendation for scale-resolving simulations is to keep dissipativity to a minimum. However, it should be appreciated that in VoF any parasitic currents arising due to numerical errors of dispersive type propagate into errors in the advection of the interface. It appears that avoiding these errors is more important than resolving steep velocity gradients. As expected, the quality of the results degrades with the coarsening of the mesh. The most precise result on $\Delta x2$ is quite close to the benchmark. On the coarser grids, the accuracy is acceptable considering how cheap the corresponding simulations are.

The predictions of the mean velocity are analysed next, see Figure 12. We focus on the streamwise component $\langle u \rangle$ only, since the level of accuracy of $\langle v \rangle$ is similar. It is clear that compared to $\langle \alpha \rangle$, the results are more robust with respect to the amount of upwinding. This is rather peculiar: The choice of interpolation scheme for u has little effect on $\langle u \rangle$, but a stronger effect on a different quantity, $\langle \alpha \rangle$. Nevertheless, the profiles obtained with higher $u\%$ are generally slightly more accurate, at least in the water phase. Using isoAdvector leads to superior accuracy in the gas phase, whereas in the water phase no significant advantage over MULES is achieved. The combination of $\Delta x2$, $u100\%$ and isoAdvector gives the best results, which are close to the benchmark. At coarser resolutions accuracy deteriorates

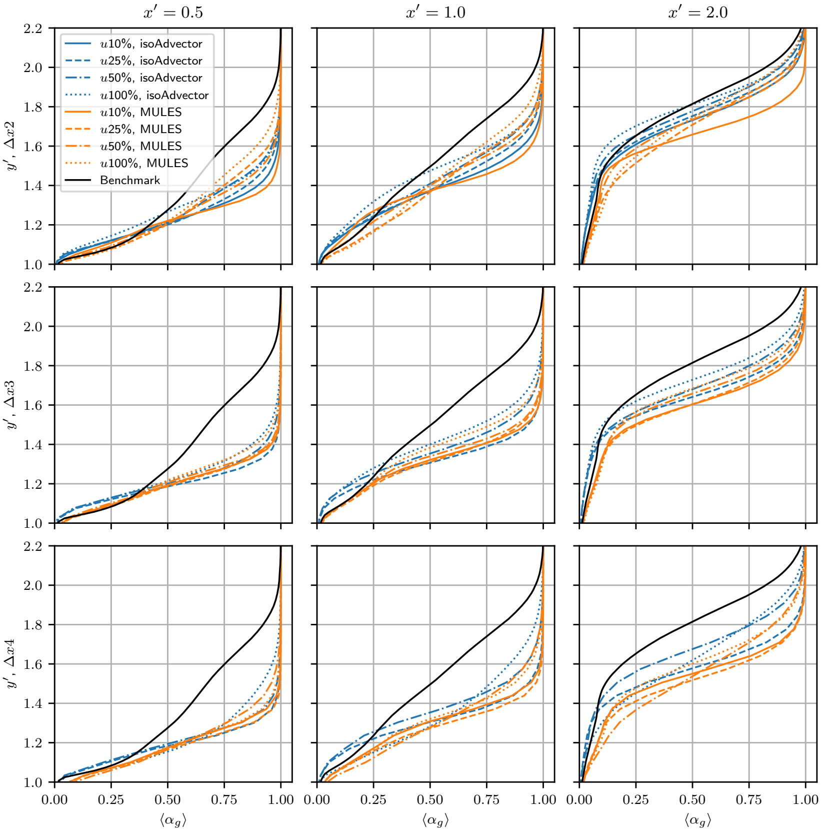

Figure 11: The profiles of $\langle\alpha\rangle$ obtained in the simulation campaign.

but not as strongly as for $\langle\alpha\rangle$.

Figure 13 shows the obtained profiles of $\langle k\rangle$. The observed error patterns are significantly less regular than in $\langle u\rangle$ and $\langle\alpha\rangle$. Two factors contribute to this. One is that $\langle k\rangle$ lumps together the errors in the variances of the three velocity components. The other is that parasitic oscillations have a direct amplifying effect on $\langle k\rangle$. Both of the above can lead to either error cancellation or amplification. On the $\Delta x2$ grid, the best results are achieved with isoAdvector and 25/50% upwinding. In case of u100%, the main peak in the detached shear layer is somewhat under-predicted, but the discrepancy is not very significant. An interesting observation is that at lower grid resolutions, a secondary peak in $\langle k\rangle$ is developed for $x' = 1.0$ and 2.0 right underneath the interface. This unphysical peak is more pronounced when isoAdvector is used, and can even be observed on the $\Delta x2$ grid when this interface capturing technique is used. It is

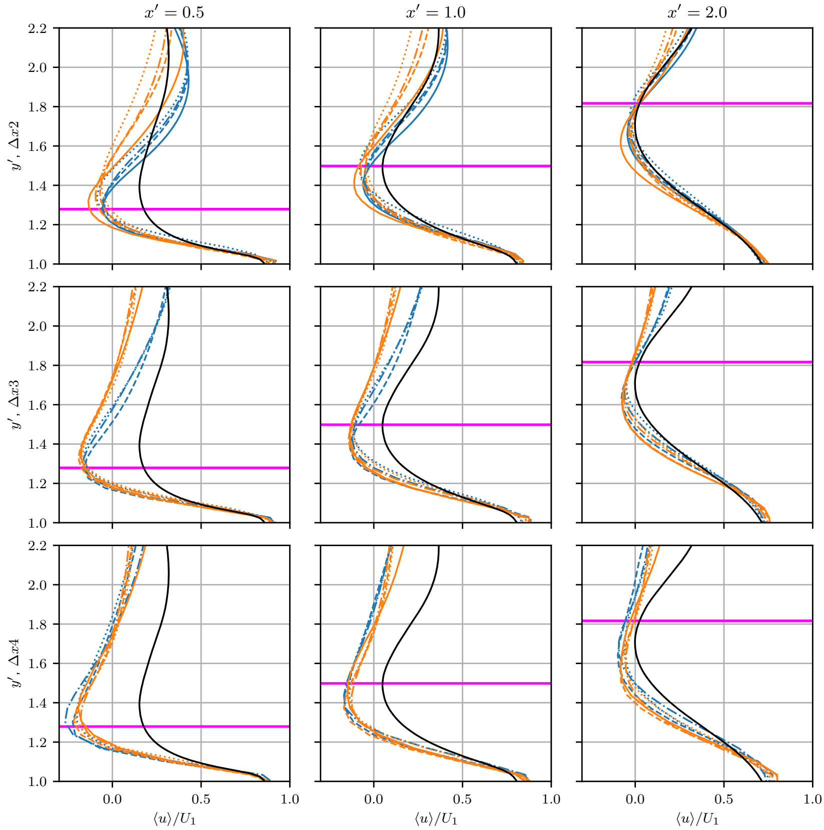

Figure 12: The profiles of $\langle u \rangle / U_1$ obtained in the simulation campaign. Line styles and colours as in Figure 11.

present in all three components of the velocity variance, although for the streamwise component it is less pronounced. The size of the peak grows with decreasing amount of upwinding, which confirms its numerical origin. Even apart from this additional peak, the results for $\langle k \rangle$ on $\Delta x3$ and $\Delta x4$ are quite inaccurate, although the combination $\Delta x4$, $u50\%$, MULES does reproduce the main features of the benchmark profiles fairly faithfully.

The analysis of velocity predictions is now concluded with considering the spanwise energy spectra of the streamwise velocity, see Figure 14. The spectra are computed at the same three $[x, y]$ locations as the spanwise autocorrelation functions for the benchmark simulations. This entails that the respective x' values are slightly different from simulation to simulation. The reason for considering spanwise spectra instead of temporal is that, due to a larger amount of samples to average across, the spanwise spectra are much smoother, making it easier to distinguish the profiles

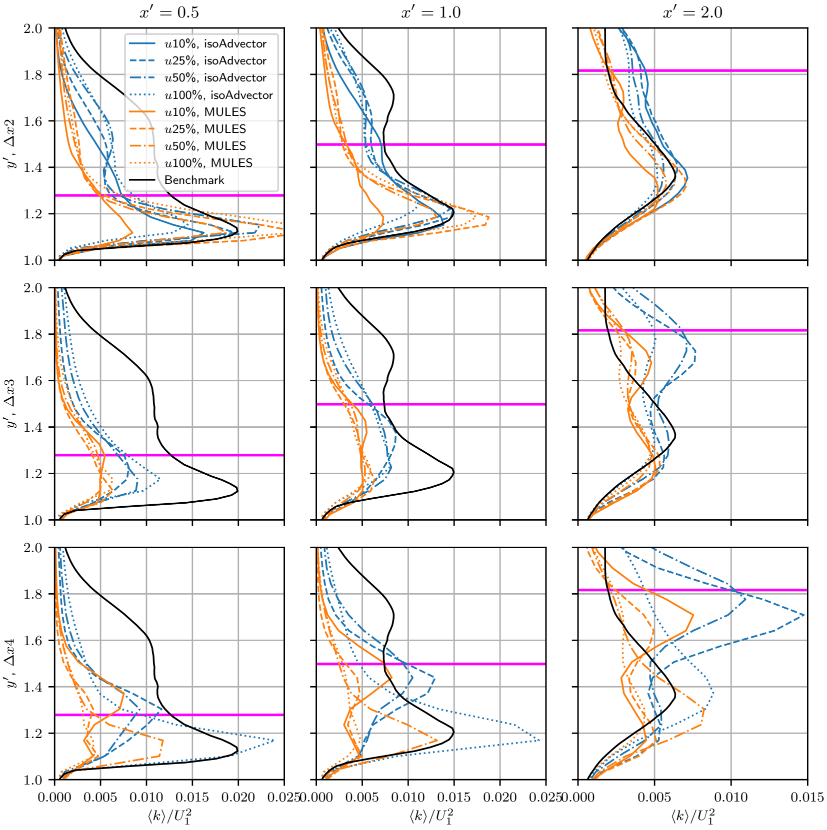

Figure 13: The profiles of $\langle k \rangle / U_1^2$ obtained in the simulation campaign.

from different simulations in the plots. Unsurprisingly, increased upwinding leads to heavier dampening of the high-frequency fluctuations. Due to the log-log scale being used, it is actually difficult to distinguish any effects of the VoF algorithm or Δx, besides for the fact that the frequency band of the spectrum is larger for denser meshes. One could say that for small amounts of $u\%$ the spectrum is relatively well-predicted even at $\Delta x4$. Therefore, one should exercise caution when making judgements regarding mesh resolution based on spectrum predictions.

Finally, the periodicity of air entrainment is analysed. As for the benchmark simulation, the autocorrelation functions of the volume of air passing through a box located some distance downstream of the toe (see top-left plot in Figure 3) were computed. The results are shown in Figure 15. For $\Delta x2$ and $\Delta x3$, the location of the first peak is quite well predicted by all the simulations, whereas for $\Delta x4$ the accuracy deteriorates, in particular for some of the simula-

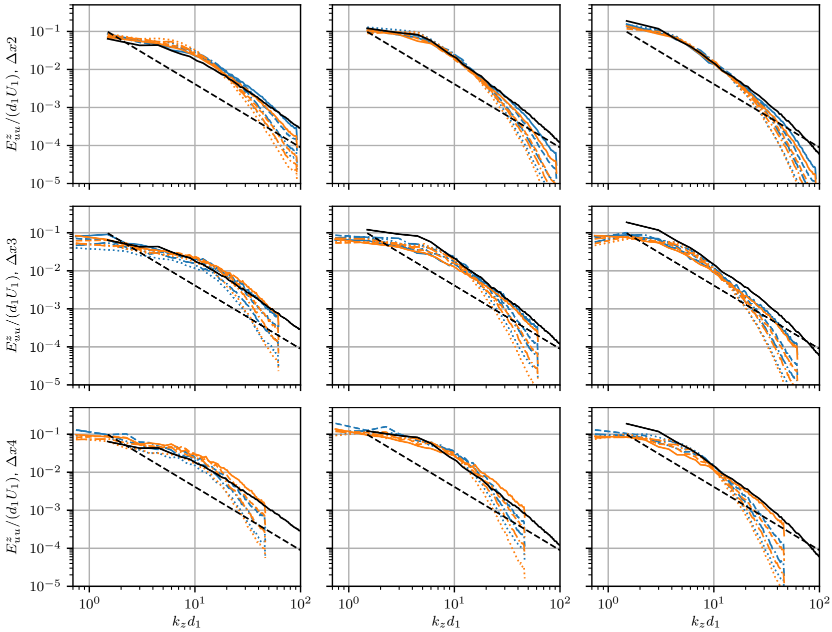

Figure 14: The spanwise velocity spectra obtained in the simulations at three selected locations: $[1.24, 1]$ (left), $[3.24, 1.1]$ (middle), $[5.24, 1.4]$ (right). Line styles and colours as in Figures 11 and 13.

tions using MULES. Animations of the $\alpha = 0.5$ isosurface reveal that isoAdvector does a much better job at preserving the sharpness of the interface as the entrained bubbles travel downstream. Therefore, if tracking the fate of the bubbles is important, using this VoF approach is recommended. It should also be noted that while all the simulation predict similar entrainment frequencies, other statistical air entrainment properties do not agree equally well. For example, the mean amount of air within the monitored box is highly affected by the choice of the VoF method, with MULES giving systematically higher values.

5. Conclusions

This article presents results from an extensive simulation campaign studying the effects of different modelling parameters on the accuracy of LES of CHJ flow at $\mathrm{Fr}_1 = 2$. The simulations were performed with a general-purpose finite-volume based CFD code, making the obtained results relevant for industry professionals and researches alike.

A benchmark simulation on a dense grid was conducted to test whether commonly employed VoF-based multiphase modelling methodologies are sufficiently accurate to capture the complicated physics of the flow. Comparison with DNS data [15] has shown that the answer is positive, and good agreement with the reference has been found for the considered quantities of interest. However, it was also revealed that numerical instabilities, discussed in Section 2.5, constitute a significant problem. It is virtually impossible to know a priori whether the chosen numerical setup would lead to a stable simulation, and a crash may occur sporadically after a significant part of the simulation time has already past. Addressing the primary sources of instability (surface tension, density gradient term in (1)) should therefore be

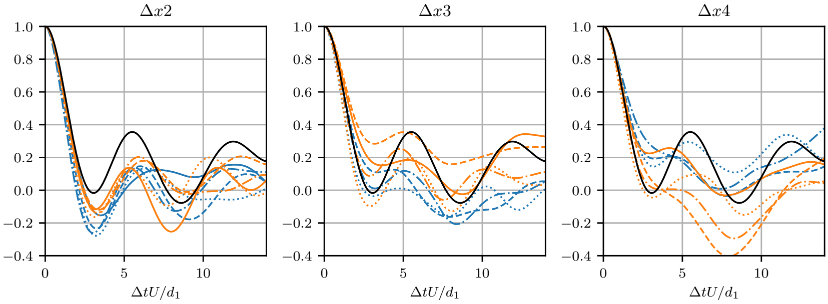

Figure 15: The obtained autocorrelation functions of the volume of leaked air. Line styles and colours as in Figures 11 and 13.

a high priority for the development of VoF solvers in OpenFOAM® and other codes based on similar algorithms.

The rest of the simulation campaign focused on the effects of grid resolution, amount of upwinding, and VoF methodology. One of the most interesting results is that the most dissipative scheme, $u100\%$, led to the best results for nearly all the considered quantities of interest. Fortunately, dissipation also favours stability, which means that having both an accurate and stable numerical setup is possible.

Using the geometric VoF methodology, isoAdvector, was shown to lead to improved accuracy of the results and preservation of the interface sharpness. This characteristic is particularly important if one of the simulation goals is tracking the fate of entrained bubbles. However, the chance of instability is also increased by isoAdvector, and for some combinations of modelling parameters the simulations could not be run. Unfortunately, this included the benchmark simulation. The computational costs of isoAdvector simulations are also significantly larger than their MULES counterparts, see Table 2. For equivalent simulation settings, the maximum cost ratio was 1.5, however due to MULES being more stable it is possible to select a larger time step, which makes the difference even larger.

The combination of parameters that resulted in good predictions for all the quantities of interest is the $\Delta x2$ grid, the isoAdvector and the $u100\%$ scheme. This combination of parameters is therefore recommended when compromising accuracy in favour of computational efficiency is not an option. Using MULES instead is an alternative when guaranteed numerical stability and improved efficiency can motivate a modest reduction in the accuracy of the profiles and worsened resolution of individual bubbles. The $\Delta x3$ grid could be used to reduce costs significantly and still maintain a level of predictive accuracy that can be suitable for industrial simulations. Using the $\Delta x4$ can only be recommended when the CHJ is a part of a larger flow configuration and is not of particular interest as such.

6. Acknowledgements

This work was supported by grant number P38284-2 from the Swedish Energy Agency. The simulations were performed on resources provided by Chalmers Centre for Computational Science and Engineering (C3SE) and UNINETT Sigma2—the National Infrastructure for High Performance Computing and Data Storage in Norway. The authors are thankful to Milad Mortazavi for sharing the data files from the DNS simulation [15].

References

[1] A. Bayon, D. Valero, R. García-Bartual, F. J. Vallés-Morán, and P. A. López-Jiménez. Performance assessment of OpenFOAM and FLOW-3D in the numerical modeling of a low Reynolds number hydraulic jump. *Environmental Modelling and Software*, 80:322–335, 2016.

[2] A. Bayon-Barrachina and P. A. Lopez-Jimenez. Numerical analysis of hydraulic jumps using OpenFOAM. *Journal of Hydroinformatics*, 17(4):662–678, 2015.

[3] J. U. Brackbill, D. B. Kothe, and C. Zemach. A continuum method for modeling surface tension. *Journal of Computational Physics*, 100(2):335–354, 1992.

[4] J. C. Cano-Lozano, R. Bolaños-Jiménez, C. Gutiérrez-Montes, and C. Martínez-Bazán. The use of Volume of Fluid technique to analyze multiphase flows: Specific case of bubble rising in still liquids. *Applied Mathematical Modelling*, 39(12):3290–3305, 2015.

[5] S. M. Damián. *An extended mixture model for the simultaneous treatment of short and long scale interfaces*. PhD thesis, National University of the Littoral, 2013.

[6] L. Davidson. Large Eddy Simulations: How to evaluate resolution. *International Journal of Heat and Fluid Flow*, 30(5):1016–1025, 2009.

[7] A. Gonzalez and F. Bombardelli. Two-phase-flow theoretical and numerical models for hydraulic jumps, including air entrainment. In *Proceedings of the Korea Water Resources Association Conference*, Seoul, Korea, 2005.

[8] C. W. Hirt and B. D. Nichols. Volume of Fluid (VOF) method for the dynamics of free boudnaries. *Journal of Computational Physics*, 39:201–225, 1981.

[9] R. I. Issa. Solution of the implicitly discretised fluid flow equations by operator-splitting. *Journal of Computational Physics*, 62(1):40–65, 1986.

[10] V. Jesudhas, R. Balachandar, V. Roussinova, and R. Barron. Turbulence characteristics of classical hydraulic jump using DES. *Journal of Hydraulic Engineering*, 144(6):04018022, 2018.

[11] W.-W. Kim and S. Menon. A new dynamic one-equation subgrid-scale model for large eddy simulations. In *33rd Aerospace Sciences Meeting and Exhibit*, page 356, 1995.

[12] P. K. Kundu and I. M. Cohen. *Fluid Mechanics*. Academic Press, 4th edition, 2008.

[13] Pi. Lubin, S. Glockner, and H. Chanson. Numerical simulation of air entrainment and turbulence in a hydraulic jump. In *Colloque SHF : Modeles Physiques Hydrauliques*, pages 109–114, Lyon and Grenoble, 2009.

[14] J. Ma, A. A. Oberai, R.T. Lahey, and D. A. Drew. Modeling air entrainment and transport in a hydraulic jump using two-fluid RANS and DES turbulence models. *Heat and Mass Transfer*, 47(8):911–919, 2011.

[15] M. Mortazavi, V. Le Chenadec, P. Moin, and A. Mani. Direct numerical simulation of a turbulent hydraulic jump: Turbulence statistics and air entrainment. *Journal of Fluid Mechanics*, 797:60–94, 2016.

[16] T. Mukha. *Inflow generation for scale-resolving simulations of turbulent boundary layers*. Licentiate thesis, Uppsala University, 2016.

[17] S. Popinet. An accurate adaptive solver for surface-tension-driven interfacial flows. *Journal of Computational Physics*, 228(16):5838–5866, 2009.

[18] J. Roenby, H. Bredmose, and H. Jasak. A computational method for sharp interface advection. *Royal Society Open Science*, 3(11), 2016.

[19] H. Rusche. *Computational fluid dynamics of dispersed two-phase flows at high phase fractions*. PhD thesis, Imperial College of Science, Technology and Medicine, 2002.

[20] H. Scheufler. Implementation of new surface tension models for the Volume of Fluid Method. In *7th ESI OpenFOAM Conference*, Berlin, Germany, 2019.

[21] D. Valero, N. Viti, and C. Gualtieri. Numerical simulation of hydraulic jumps. Part 1: Experimental data for modelling performance assessment. *Water*, 11(1):1–16, 2018.

[22] H. K. Versteeg and W. Malalasekera. *An introduction to computational fluid dynamics: The finite volume method*. Pearson Education Limited, 2nd edition, 2007.

[23] N. Viti, D. Valero, and C. Gualtieri. Numerical simulation of hydraulic jumps. Part 2: Recent results and future outlook. *Water*, 11(1):1–18, 2018.

[24] V. Vukčević, H. Jasak, and I. Gatin. Implementation of the Ghost Fluid Method for free surface flows in polyhedral Finite Volume framework. *Computers and Fluids*, 153:1–19, 2017.

[25] A. Witt, J. Gulliver, and L. Shen. Simulating air entrainment and vortex dynamics in a hydraulic jump. *International Journal of Multiphase Flow*, 72:165–180, 2015.

[26] A. Witt, J. S. Gulliver, and L. Shen. Numerical investigation of vorticity and bubble clustering in an air entraining hydraulic jump. *Computers and Fluids*, 172:162–180, 2018.

[27] S. T. Zalesak. Fully multidimensional flux-corrected transport algorithms for fluids. *Journal of Computational Physics*, 31(3):335–362, 1979.

CRediT authorship contribution statement

Timofey Mukha: Conceptualization of this study, Methodology, Investigation, Visualization, Data curation, Writing - Original draft preparation. **Silje Kreken Almeland:** Conceptualization of this study, Methodology, Investigation, Resources, Writing - review & editing. **Rickard E. Bensow:** Conceptualization of this study, Funding acquisition, Project administration, Resources, Supervision, Writing - review & editing.

Appendix B

Statements from co-authors

Encl. to application for assessment of PhD thesis

Faculty of Engineering

NTNU

STATEMENT FROM CO-AUTHOR

(cf. section 10.1 in the PhD regulations)

Silje Kreken Almeland applies to have the following thesis assessed:

Numerical modelling of air entrainment in hydraulic engineering

*) The statement is to describe the work process and the sharing of work and approve that the article may be used in the thesis.

*)

Statement from co-author on article: "Multiple solutions of the Navier-Stokes equations computing water flow in sand traps"

I was the supervisor of both Mr. Aryal and Ms. Almeland during their work on this project. Two numerical models were used: SSIIM and OpenFOAM. I made the SSIIM model. Mr. Aryal set up and ran the SSIIM model for the Kimti sand trap, and discussed the results in relation to measurements from a laboratory model in Nepal. Mrs. Bråtveit was in charge of the field measurements from the Tonstad sand trap. Ms. Almeland did all the work with OpenFOAM: Setting up the model for the Tonstad sand trap, making the results, parameter tests and the graphics. Ms. Almeland also made recomputations using the SSIIM model and graphics from the results. The text of the article was mainly written by Ms. Almeland.

Trondheim 5 oct. 2020 Nils Reidar Olsen

Place, date Signature co-author

Encl. to application for assessment of PhD thesis

Faculty of Engineering

NTNU

STATEMENT FROM CO-AUTHOR

(cf. section 10.1 in the PhD regulations)

Silje Kreken Almeland applies to have the following thesis assessed:

Numerical modelling of air entrainment in hydraulic engineering

*) The statement is to describe the work process and the sharing of work and approve that the article may be used in the thesis.

*)
Statement from co-author on article: "Multiple solutions of the Navier-Stokes equations computing water flow in sand traps"

Nesflaten 8/10-20
Place, date

Kari Bråveit
Signature co-author

Encl. to application for assessment of PhD thesis

Faculty of Engineering

NTNU

STATEMENT FROM CO-AUTHOR

(cf. section 10.1 in the PhD regulations)

Silje Kreken Almeland applies to have the following thesis assessed:

Numerical modelling of air entrainment in hydraulic engineering

*) The statement is to describe the work process and the sharing of work and approve that the article may be used in the thesis.

*)
Statement from co-author on article: **"Multiple solutions of the Navier-Stokes equations computing water flow in sand traps"**

I hereby declare that I am aware of the fact that the work in the article of which I am a co-author will form a part of the PhD thesis by the candidate.

Kathmandu, 12 Oct, 2020
Place, date

Signature co-author

Encl. to application for
assessment of PhD thesis

Faculty of Engineering

NTNU

STATEMENT FROM CO-AUTHOR

(cf. section 10.1 in the PhD regulations)

Silje Kreken Almeland applies to have the following thesis assessed:

Numerical modelling of air entrainment in hydraulic engineering

*) The statement is to describe the work process and the sharing of work and approve that the article may be used in the thesis.

*)

Statement from co-author on article: “An improved air entrainment model for stepped spillways”

Here, the vast majority of the work has been performed by Silje K. Almeland. This included theoretical work on developing the entrainment model, implementing it in C++, conducting and post-processing simulations, and producing the first full draft of the manuscript. My main role as a co-author involved discussing the ongoing results, brainstorming ideas regarding model development, and guiding the layout of the simulation campaign. I have also contributed significantly to finalizing the text of the manuscript and helped polish the C++ code.

Gothenburg 2020-09-30
Place, date

Timofey Mukha
Signature co-author

*)

Statement from co-author on article: “LES of a classical hydraulic jump: Influence of modelling parameters on the predictive accuracy”

Here, Silje K. Almeland performed the initial exploratory stage of hydraulic jump simulations, which was instrumental to determining the focus of the article. Based on evaluation of prior art, she set up the simulation case with a stable jump, which is known to be difficult to achieve. She then performed various types of simulations, exploring possibilities for turbulence modelling, air entrainment modelling, etc. Based on this study, angling the article towards LES was chosen. The LES simulations were performed by me, using the case files created by Silje K. Almeland. I’ve also produced the first manuscript draft and finalized it based on the comments from Silje K. Almeland and Rickard E. Bensow.

Gothenburg 2020-09-30
Place, date

Timofey Mukha
Signature co-author

Encl. to application for assessment of PhD thesis

Faculty of Engineering

NTNU

STATEMENT FROM CO-AUTHOR

(cf. section 10.1 in the PhD regulations)

Silje Kreken Almeland applies to have the following thesis assessed:

Numerical modelling of air entrainment in hydraulic engineering

*) The statement is to describe the work process and the sharing of work and approve that the article may be used in the thesis.

*)
Statement from co-author on article: "An improved air entrainment model for stepped spillways"

Silje K. Almeland did the major work in the study, including formulating the research problem, identify background research, develop and implement improved models, set-up and conduct simulations, analyse results and write the first draft of the paper. My contribution in this paper is limited to 1) guidance on which parts of the model to develop and on the layout on simulation plan to assess current model as well as the development, and 2) support in interpreting results from the simulations. I read the manuscript in a rather late state and gave feedback and some minor corrections.

Gothenburg 201002 ……………………………… Bensow

Place, date ……………………………… Signature co-author

*)
Statement from co-author on article: "LES of a classical hydraulic jump: Influence of modelling parameters on the predictive accuracy"

In order to get a better understanding of the details of air entrainment and what influence this mechanism, a more canonical case than the stepped spillway was discussed and the hydraulic jump was proposed. Silje K Almeland did the background research on the case, defined the case and set-up initial simulations. She further did simulations to explore the connection between this case and the air entrainment modelling for the spillway. My contributions was in guidance in the initial discussions, taking part in discussions of the results, and reviewing late drafts of the paper

Gothenburg 201002 ……………………………… Bensow

Place, date ……………………………… Signature co-author